Focused Rocket-Ejector RBCC Experiments

Final Report
for
NASA Contract Grant NAG8-1844

Robert J. Santoro and Sibtosh Pal

Propulsion Engineering Research Center
and
Department of Mechanical and Nuclear Engineering
The Pennsylvania State University
University Park, Pennsylvania

September, 2003

PENNSTATE

TABLE OF CONTENTS

ABSTRACT

This document reports the results of additional efforts for the Rocket Based Combined Cycle (RBCC) rocket-ejector mode research work carried out at the Penn State Propulsion Engineering Research Center in support of NASA's technology development efforts for enabling 3rd generation Reusable Launch Vehicles (RLV). The two tasks conducted under this program build on earlier NASA MSFC funded research program on rocket ejector investigations. The first task continued a systematic investigation of the improvements provided by a gaseous hydrogen (GH_2)/oxygen (GO_2) twin thruster RBCC rocket ejector system over a single rocket system. In a similar vein, the second task continued investigations into the performance of a hydrocarbon (liquid JP-7)/gaseous oxygen single thruster rocket-ejector system. To gain a systematic understanding of the rocket-ejector's internal fluid mechanic/combustion phenomena, experiments were conducted with both direct-connect and sea-level static diffusion and afterburning (DAB) configurations for a range of rocket operating conditions. For all experimental conditions, overall system performance was obtained through global measurements of wall static pressure profiles, heat flux profiles and engine thrust. For the GH_2/GO_2 propellant rocket ejector experiments, high frequency measurements of the pressure field within the system were also made to understand the unsteady behavior of the flowfield.

1. INTRODUCTION

Recent interest in low cost, reliable access to space has generated increased interest in advanced technology approaches to space transportation systems. A key to the success of such programs lies in the development of advanced propulsion systems capable of achieving the performance and operations goals required for the next generation of space vehicles. One extremely promising approach involves the combination of rocket and air-breathing engines into a rocket-based combined-cycle engine (RBCC). Although there are several design variations for the RBCC engine, the gamut of concepts includes four flight regimes, viz. rocket-ejector, ramjet, scramjet and all-rocket [1]. Of these four flight regimes, the rocket-ejector mode that encompasses a flight Mach number range from zero to two is the least well understood. Studies of RBCC engine concepts are not new and studies dating back thirty years are well documented in the literature. However, studies focused on the rocket-ejector mode of the RBCC cycle are lacking.

The present investigation builds on earlier research programs funded by NASA MSFC to examine critical rocket ejector performance issues. The final report for the initial program, "Experimental and Analytical Modeling of the Rocket Ejector Mode of a Combined Cycle Rocket-Based Engine" (Original NASA Contract Grant NAS8-40890) was submitted in June 2001 [2]. Additional work was documented as an addendum report titled, "Focused RBCC Experiments: Two-Rocket Configuration Experiments and Hydrocarbon/Oxygen Rocket Ejector Experiments" (Addendum Report for NASA Contract Grant NAG8-1844), and submitted in September, 2003 [3]. The objective of the original research program was to obtain new data using advanced optical diagnostics such as Raman spectroscopy and CFD techniques to investigate mixing in the rocket ejector mode. A new research facility for the study of the rocket ejector mode was designed and fabricated for this purpose. The tasks described in the addendum report investigated rocket ejector performance and operation for a single JP-7/gaseous oxygen (GO_2) thruster at 200 psia and for twin gaseous hydrogen (GH_2)/GO_2 thrusters also operating at 200 psia. The objectives of the present program are to further the understanding achieved in the earlier investigations through additional measurements. The present investigation utilizes the rocket-ejector infrastructure developed for the earlier programs to obtain additional experimental measurements for CFD code validation.

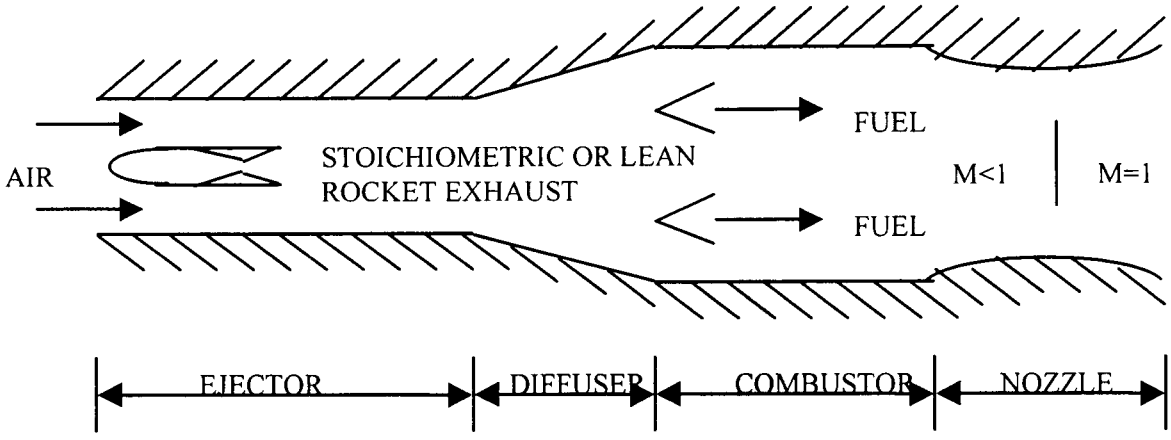

A) Tandem Rocket Ejector-Ramjet

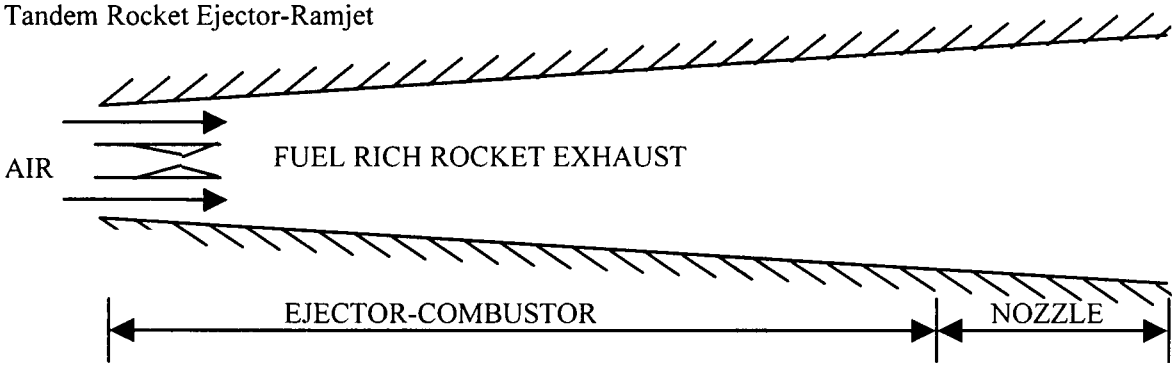

B) Integrated Ejector Combustor

Fig. 1.1. Basic Ejector cycles described by Billig [5].

The experimental configuration studied here (and in the original program) is based on the well-known 1968 experimental rocket-ejector study of Odegaard and Stroup [4]. Early on in the first program, it was recognized that advancements of both proprietary and classified natures have been made in the last thirty years, however, this particular geometry was chosen as the baseline configuration because it represents the most comprehensive set of data available in the open literature. The scope of the current study was not to simply duplicate the experiments of Odegaard and Stroup, but to build on this benchmark study by bringing to bear advances made in diagnostic techniques to quantitatively document the flow characteristics of the rocket-ejector mode of the RBCC engine.

From an RBCC engine design point-of-view, two basic ejector cycles are potentially attractive as noted by Billig [5] and schematized in Fig. 1.1. The first cycle concept includes a sequential inlet/rocket ejector/mixer/diffuser/combustor/nozzle assembly. This is also the cycle

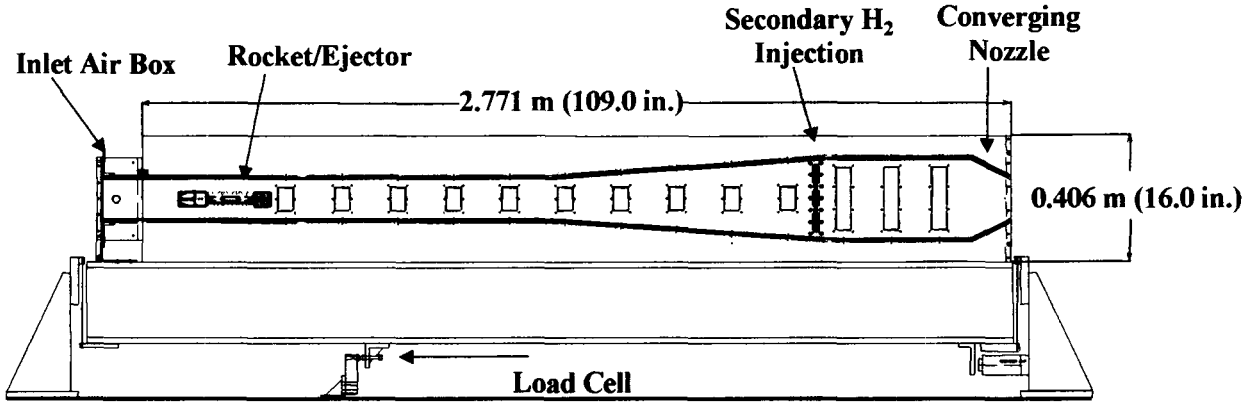

Fig. 1.2. Side view of direct-connect Diffusion and Afterburning (DAB) RBCC test rig developed in the original program. Flow is from left to right.

that was studied by Odegaard and Stroup. The second cycle concept features a single integrated duct with no physical nozzle that relies on thermal choke to simulate the key features of the first cycle. The experiments reported in the original study investigated both these cycle concepts, whereas the focus of the current study was to further investigate the first concept.

The original study [2] was conducted using a two-dimensional rocket-ejector setup that used a single two-dimensional gaseous hydrogen/gaseous oxygen (GH_2/GO_2) rocket as the ejector. A schematic and photograph of the setup are shown in Figs. 1.2 and 1.3, respectively. Experiments of this original study were conducted for the Diffusion and Afterburning (DAB) geometry for both direct-connect (DC) and sea-level static (SLS) configurations. The ejector rocket was operated at mixture ratios of eight and four and at chamber pressures of 500 and 200 psia. Experimental measurements included estimation of the overall system performance obtained through global measurements of wall static pressure profiles, heat flux profiles and engine thrust, and detailed mixing and combustion information obtained through Raman spectroscopy measurements of major species (gaseous oxygen, hydrogen, nitrogen and water vapor).

Based on the success of the earlier program [2], additional research was conducted using the established rocket-ejector facility. The objectives of the additional research (viz., Addendum report [3]), were to establish databases for a (a) single rocket ejector that uses JP-7/GO_2 propellants, and (b) twin-rocket ejector that uses GH_2/GO_2 propellants. Results obtained for the single JP-7/GO_2 rocket ejector configuration operating at 200 psia include rocket ejector duct static pressure profiles, and heat flux profiles, as well as overall engine thrust. For the second

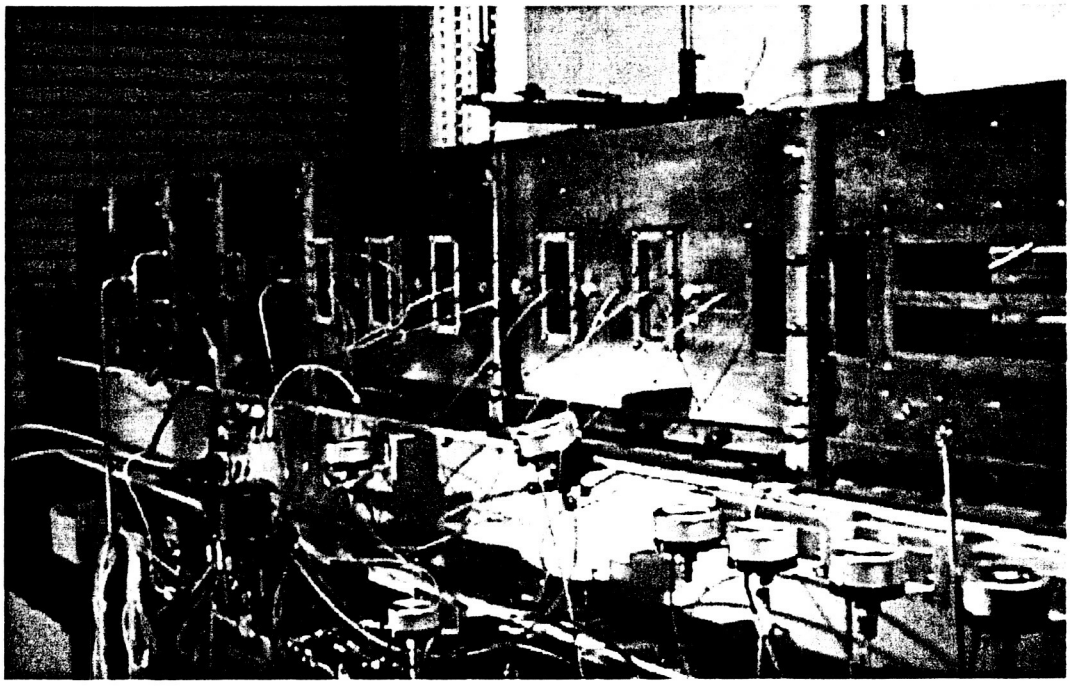

Fig. 1.3. Penn State RBCC rocket-ejector test article. Flow is from right to left.

task, two identical rockets were designed, each with one-half the frontal cross-sectional area of the existing single rocket unit. These rockets were designed for 200 psia operation. In addition to the global measurements of static pressure/heat flux profiles and engine thrust, measurements for the twin-rocket configuration also included detailed flowfield measurements of major species.

The current program furthers the understanding of rocket ejectors obtained under the earlier investigations [2, 3]. The initial objective of the current effort was to investigate (a) rocket ejector performance with a single JP-7/GO_2 rocket operating at 500 psia. However, during the course of the program, due to a need for more details for the GH_2/GO_2 twin-rocket ejector configuration, the program scope was redirected. The redirection was geared towards extending the twin-rocket database to include results for a different rocket placement (in the RBCC ejector configuration), further static pressure measurements in the near rocket exhaust region, and information on the unsteadiness in the flowfield.

In this report, the experimental facility and setups are first described in Chapter 2, followed by a description of diagnostic techniques in Chapter 3. Results for the single rocket JP-7/GO_2 and twin-rocket GH_2/GO_2 experiments are presented and discussed in Chapters 4 and 5, respectively.

2. EXPERIMENTAL FACILITY AND SETUP

The RBCC rocket-ejector combustion experiments for both single rocket (JP-7/GO_2) propellants and single/twin rocket (GH_2/GO_2) were carried out at Penn State's Cryogenic Combustion Laboratory (CCL). This laboratory was established in 1989 to be the flagship facility for Penn State's Propulsion Engineering Research Center (PERC). In this section, the capabilities of the CCL are discussed first. This is followed by a description of the setups used for the two sets of experiments.

2.1. Cryogenic Combustion Laboratory

The CCL is a unique university facility where researchers conduct work on representative rocket engine flowfields. The laboratory is designed based on a similar test cell at the NASA Glenn Research Center (formerly the NASA Lewis Research Center). The CCL, a remotely controlled laboratory, features a control room, diagnostic room and the test cell. The test cell, where the combustion experiment is housed, is isolated from the control and diagnostic rooms with reinforced concrete walls. For experimentation, the test cell's garage door is fully opened and the ventilation turned on to prevent the possible buildup of combustible materials. The diagnostic room located adjacent to the test cell is utilized for situating all the laser-based diagnostics. Optical ports between the diagnostics room and the test cell provide access into the test cell. The control room houses the computer control system that is used for timing the rocket firing. Video cameras with pan features enable remote visualizations of the test room. The operation of the entire system is designed with two levels of safety.

The propellant flowrate capabilities of the CCL are tabulated in Table 2.1. The CCL was initially operable for gaseous oxygen/hydrogen propellants. Liquid oxygen capability was

Table 2.1. Flowrate capabilities of the cryogenic combustion laboratory (CCL).

Propellant	Maximum Flowrate (lbm/s)
Gaseous Oxygen (GO_2)	1
Gaseous Hydrogen (GH_2)	0.25
Liquid Oxygen (LOX)	1
Liquid Hydrocarbon	0.5
Air	4 (can be upgraded to 16)

Table 2.2. Comparison of current rocket ejector and Odegaard and Stroup setups.

	Marquardt *(Areas Divided by 8)*	**Penn State**
Thruster Throat Area, A_t (sq in)	0.274	0.300
Mixer Section Area, A_{mix} (sq in)	14.1	15.0
A_{mix}/A_t --	51.5	50.0
Afterburner Area, $A_{A/B}$ (sq in)	31.75	30
$A_{A/B}/A_{mix}$ --	2.25	2.00
Duct Exit Area, A_{ex} (sq in)	14.4	15.0
Mixer/Combustor Length, L_{mix} (in)	36.0 *(Baseline)*	35.3
Duct Length (without inlet), L_{tot} (in)	107 *(Baseline)*	109

initiated within a year of the laboratory's operation. Liquid hydrocarbon capability was brought on-line three years later. Finally airflow capability was brought on-line in early 1997.

2.2. JP-7/GO_2 Single Rocket Ejector Setup

The JP-7/GO_2 experiments utilized the existing Penn State RBCC hardware and facility [2, 3, 6-9]. The RBCC test rig was designed based on the earlier design by Odegaard and Stroup [4]. The Odegaard and Stroup design was axisymmetric and employed an annular array of rocket/ejectors. The configuration used in the current set of experiments focuses on a 1/8 "sector" slice of the axisymmetric design, maintains the critical area ratios, and converts them into a 2-D geometry. The key geometric parameters defining the current two-dimensional rocket-ejector are compared to those of Odegaard and Stroup in Table 2.2.

Schematics for both direct-connect (DC) and sea level static (SLS) experiments are shown in Fig. 2.1 for the DAB configuration. These configurations differ only in the inlet section: For the DC experiments, air flow (secondary flow) was controlled by a venturi and delivered through a closed inlet box (Fig. 2.1(a)). On the other hand, the SLS configuration (Fig. 2.1(b)) had an open inlet that allowed ambient air to be entrained into the flow path, where flow rates of the entrained air depended on the pumping effect of the rocket-ejector. Details of the two rocket ejector inlets are shown in Fig. 2.2.

The rocket ejector flow path has four sections downstream of the rocket exit plane: a mixer, a diffuser, an afterburner, and a converging nozzle as labeled in Fig. 2.1(a). Throughout the flow path, the internal width was uniform (3 in.) to allow two-dimensional flow field analyses.

The DAB geometry was designed to achieve optimum performance when the rocket was operated at stoichiometric conditions. The hot products from the rocket (primary flow) and the air (secondary flow) mix in the 35 in. long constant area mixer section with internal height of 5 in. The mixed flow, then passes through the diffuser section that was 35 in. in length. The flow path height continuously expands from 5 in. to 10 in. at the end of the diffuser section. Secondary fuel (GH_2) is injected at this axial location from a vertical series of seven 0.1 in. diameter orifices (both sides). The ejected air and the afterburner fuel combust in the constant area afterburner which is 10 in. in height and 18 in. long. Finally, the flow accelerates in the

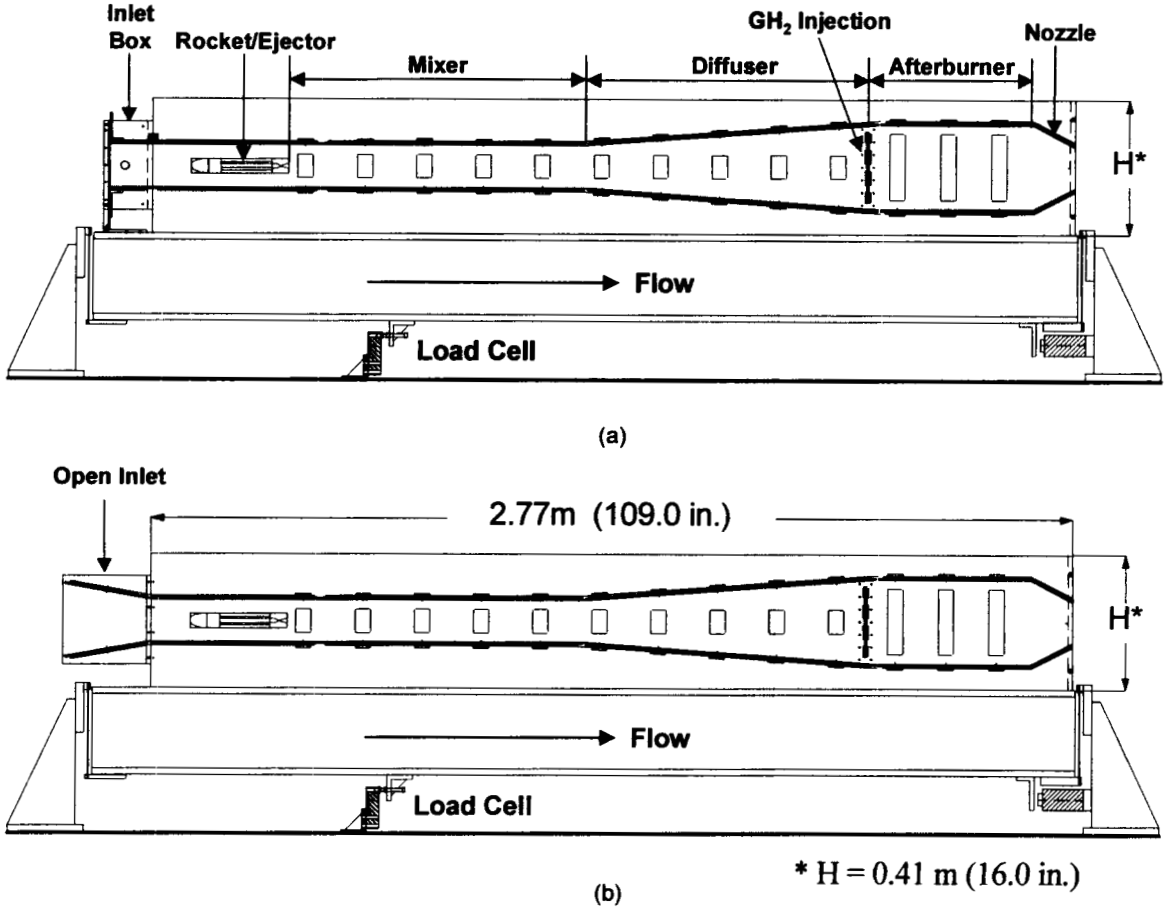

Fig. 2.1. RBCC test rig for the DAB geometry with modifications of the inlet section. (a) direct connect configuration (DC), (b) sea level static configuration (SLS).

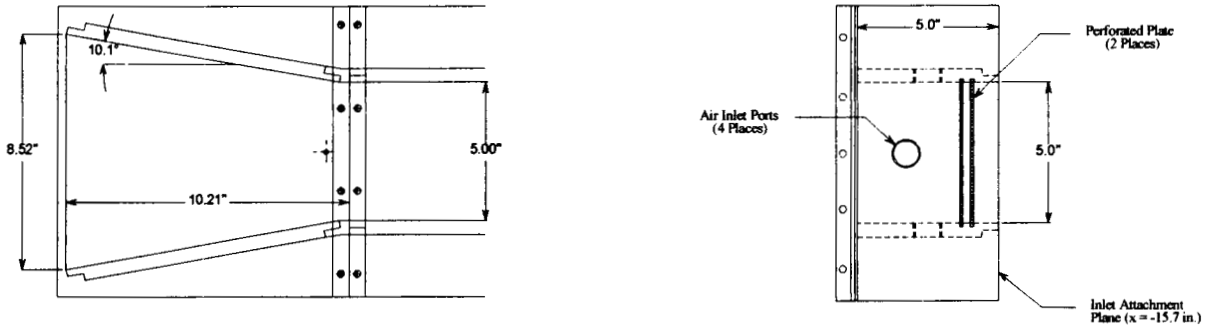

(a) **(b)**

Fig. 2.2. Rocket ejector inlet configurations. (a) Open inlet, and (b) direct connect.

converging nozzle which has a contraction ratio of two. Both the length and the exit height of the converging nozzle are 5 in. The rocket ejector rig is made from oxygen-free high-conductivity (OFHC) copper whereas the joints are supported using stainless steel bars.

The rocket ejector setup features measurement ports for static pressure and heat flux measurements. The entire test rig is mounted on a hanging I-beam to enable thrust measurements using a load cell. Details of all measurements are described in the next chapter.

For the single rocket experiments, the rocket was located along the centerline of the flow path at an axial location 4.4 in. downstream from the inlet of the straight section of the air duct. The rocket consisted of a nose cone, an injector, a combustion chamber, and a nozzle as shown in Fig. 2.3. All of the rocket components have rectangular cross sections with an internal width of 3 in., which is the same as the rocket ejector flow path width. Thus, the rocket provides a uniform flow field across the width of the rocket ejector flow path. The total length of the rocket

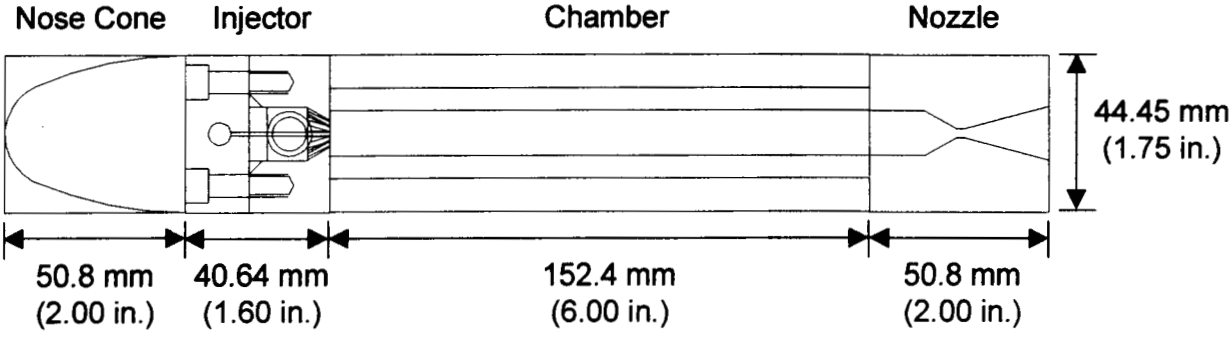

Fig. 2.3. Rocket assembly for JP-7/GO_2 rocket ejector experiments.

Table 2.3. Comparison of static pressures at the rocket exit plane for JP-7/GO_2 and GH_2/GO_2 propellants at stoichiometric mixture ratios.

Pc		JP-7/GO_2		GH_2/GO_2		Difference
MPa	(psia)	kPa	(psia)	kPa	(psia)	%
1.38	(200)	91.9	(13.3)	91.2	(13.2)	0.7
3.45	(500)	104.6	(15.2)	103.1	(15.0)	1.4

is 11.60 in., whereas the internal height of the combustion chamber is 0.5 in. The rocket sections are made from OFHC copper that are supported with bottom and top stainless steel plates.

Two rocket nozzles with expansion ratios of 3.3 and 6.0 are available for chamber pressures of 200 and 500 psia, respectively. The nozzle throat height is 0.10 in. The nozzle exit heights are 0.33 in. and 0.6 in. for the two nozzles, respectively. Although the nozzles were designed for GH_2/GO_2 propellants, the static pressure at the exit plane is comparable for JP-7/GO_2 and GH_2/GO_2 operations as summarized in Table 2.3.

An impinging injector as shown in Fig. 2.4 was used for the JP-7/GO_2 rocket-ejector experiments. The injector body and posts (inner tubes) are made of OFHC copper and stainless

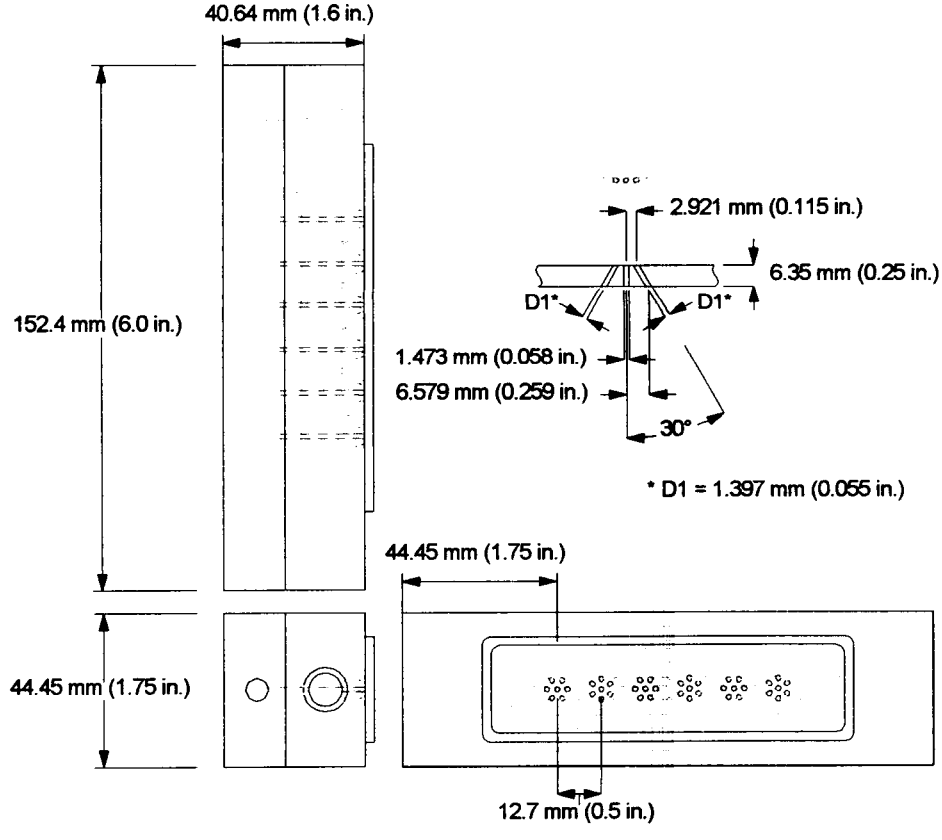

Fig 2.4. Detail of the JP-7/GO_2 injector design.

Table 2.4. Calculated injection velocities.

	JP-7	GO_2
The Number of Orifices per Element	1	6
Orifice Diameter, mm (inch)	1.48 (0.058)	1.40 (0.055)
Injection Velocity at Pc = 1.38 MPa (200psia) m/s (ft/s)	4.3 (14.2)	123.4 (404.7)
Injection Velocity at Pc = 3.45 MPa (500psia) m/s (ft/s)	10.7 (35.1)	121.9 (400.0)
Impinging Angle, degree	---	30

steel, respectively. The injector consists of six elements that are equally spaced at intervals of 0.5 in. Each element has one straight JP-7 orifice surrounded by six identical GO_2 orifices with an impingement angle of 30°. Calculated injection velocities for the injector are presented in Table 2.4. In the table, injection velocities for both 200 and 500 psia chamber pressure are shown. Note that a limited number of experiments for the 500 psia rocket chamber pressure were conducted under this program. Experiments conducted for 200 psia rocket operation have been reported in the addendum report [3].

2.3. JP-7/GO_2 Single Rocket Ejector Operating Conditions

The JP-7/GO_2 RBCC rocket ejector experimental series were to be investigated at six operating conditions (Cases $1-6$) with the Diffusion and Afterburning (DAB) geometry. The operating conditions were based on earlier single rocket experiments with GH_2/GO_2 [2, 6-8] and JP-7/GO_2 propellants [3, 9]. All the target cases were for a rocket chamber pressure of 500 psia. Table 2.5 characterizes the operating condition for each case qualitatively, whereas the detailed flow conditions are discussed later. In the table, the bypass ratio is defined as the ratio

Table 2.5. Overview of the JP-7/GO_2 experimental cases.

Mode	Direct Connect				Sea Level Static	
Case	**1**	**2**	**3**	**4**	**5**	**6**
Rocket Stoichiometry	Fuel-Rich	Fuel-Rich	Stoichiometric	Stoichiometric	Fuel-Rich	Stoichiometric
Bypass Ratio	2.1	2.7	2.1	2.7	Open Inlet	Open Inlet
Afterburner	Off	Off	On	On	Off	On
Overall Stoichiometry	Fuel-Rich	Stoichiometric	Stoichiometric	Stoichiometric	N/A*	N/A*

* Overall stoichiometry of a SLS case depends on the entrained air flow rate.

of the air mass flow rate to rocket propellant (JP-7 and GO_2) mass flow rate. Target cases for both direct connect (DC) and sea level static (SLS) configurations are listed in the table. However, experiments for only the SLS configuration (Cases 5 and 6) were completed before the scope of this research program was redirected.

Two methods of measuring the stoichiometry are introduced to characterize each case: the "rocket stoichiometry" represents the primary combustion (JP-7 and GO_2) in the rocket; the "overall stoichiometry" is determined for the combustion of the rocket exhaust, air, and GH_2 injected into the afterburner.

Although the DC Cases 1-4 were not attempted, the rationale for choosing these cases are described. Cases 1 and 2 differ only in the supplied air flow rate. The air flow rates were based on the flight conditions at Mach 1.0 and 1.9, respectively, at P_c = 500 psia operation as discussed later. For Case 1, the overall stoichiometry remained fuel rich while an overall stoichiometric mixture ratio was achieved for Case 2. Cases 3 and 4 are operated at the same bypass ratios as Cases 1 and 2, respectively, with the downstream GH_2 injection to combust all of the oxygen in the rocket-ejector duct.

Cases 5 and 6 are sea level static (SLS) cases where air is entrained through the open inlet by the pumping effect of the rocket ejector, rather than being supplied through the inlet box. The rocket is operated at a fuel rich mixture ratio in Case 5, and operated at the stoichiometric point in Case 6. For Case 6, the same mass flow rate of GH_2 as Case 3 is injected for the afterburner operation. The air flow rates for the SLS cases were calculated after the experiments using a static pressure measurements made in the inlet section.

As mentioned earlier, previous studies conducted at Penn State for GH_2/GO_2 RBCC rocket ejector conditions [2, 6-8] also investigated six cases based on the earlier experimental study of Odegaard and Stroup [4], in which the engine performance was tested at sea level static, and for flight conditions of Mach 1.0 at 9,400 ft and Mach 1.9 at 40,000 ft. For the GH_2/GO_2 RBCC direct connect cases, two air flow rates were selected by running the RAMSCRAM [10] computer program to simulate these flight conditions for a rocket operating at a chamber pressure of 500 psia.

The operating conditions for the JP-7/GO_2 experiments were determined to produce the same rocket and overall equivalence ratios as the GH_2/GO_2 experiments. Matching these conditions allows comparisons to be made between tests that use JP-7/GO_2 and GH_2/GO_2

propellants. The rocket equivalence ratio of unity was used for the GH_2/GO_2 experimental series for Cases 3, 4, and 6, whereas for Cases 1, 2, and 5, the rocket equivalence ratio was chosen to be two. Since one of the objectives of the JP-7/GO_2 experimental series was to reproduce these equivalence ratios, the stoichiometry of the primary propellants are reviewed in this section to document the rocket O/F selections for this set of experiments. The equivalent chemical composition of JP-7, $C_{10}H_{21}$, was employed for the analysis.

The stoichiometric combustion between JP-7 and oxygen is:

$$C_{10}H_{21} + 15.25\, O_2 \rightarrow 10\, CO_2 + 10.5\, H_2O \qquad [2.1]$$

Hence, the stoichiometric oxidizer to fuel ratio (O/F) becomes,

$$O/F = \frac{15.25\, MW_{O_2}}{MW_{JP-7}} \cong 3.45 \qquad [2.2]$$

where MW_{O2} is the molecular weight of oxygen, 32.00, and $MW_{JP\text{-}7}$ is the molecular weight of JP-7, 141.277. The rocket was operated at the stoichiometric O/F = 3.45 for Cases 3, 4, and 6, and O/F = 1.73 for Cases 1, 2, and 5. These O/F ratios correspond to equivalence ratios of one and two respectively, as discussed earlier.

The operating conditions for the JP-7/GO_2 experiments at rocket chamber pressures of (a) 200 psia and (b) 500 psia are shown in Table 2.6. Note that programmatically, only the 500 psia rocket experiments for the DC configuration were conducted during this investigation. Experiments with the rocket operating at 200 psia (Cases 1-6) were conducted and discussed in the addendum report [3]

For stoichiometric rocket operation (Cases 3, 4, and 6), the primary propellants are completely consumed, and the rocket exhaust mixes with the secondary air. The mixed gas is decelerated in the diverging (the diffuser) section prior to combustion with GH_2 in the afterburner. Therefore the secondary combustion for Cases 3, 4, and 6 occurs between oxygen in the air and GH_2 in the constant area afterburner section.

In contrast, the secondary combustion for Cases 1, 2, and 5 occurs far upstream of the afterburner section because a fuel rich rocket operation is not the design condition for the DAB geometry. These conditions were targeted to obtain additional measurements that will be valuable for modelers but do not represent optimum DAB operation. The reactants of the secondary combustion also differ from the stoichiometric rocket operation cases and are composed of the excess fuel from the rocket and the delivered (or entrained) air. Because of the

Table 2.6. Operating conditions: (a) P_c = 1.38 MPa (200 psia) (b) P_c = 3.45 MPa (500 psia).

Pc = 1.38 MPa (200 psia)	Direct Connect				Sea-Level Static	
	Case 1	Case 2	Case 3	Case 4	Case 5	Case 6
Rocket						
O/F	1.73	1.73	3.45	3.45	1.73	3.45
GO_2 Flow Rate kg/s	0.097	0.097	0.121	0.121	0.097	0.121
(lb/s)	(0.214)	(0.214)	(0.267)	(0.267)	(0.214)	(0.267)
JP-7 Flow Rate kg/s	0.056	0.056	0.035	0.035	0.056	0.035
(lb/s)	(0.124)	(0.124)	(0.077)	(0.077)	(0.124)	(0.077)
Equivalence Ratio	2	2	1	1	2	1
Duct						
Air Flow Rate kg/s	0.325	0.416	0.325	0.416	***0.47***	***0.48***
(lb/s)	(0.716)	(0.916)	(0.716)	(0.916)	***(1.03)***	***(1.06)***
GH_2 Flow Rate kg/s	0	0	0.010	0.012	0	0.010
in Afterburner (lb/s)	(0)	(0)	(0.021)	(0.027)	(0)	(0.021)
Overall Equivalence Ratio	1.28	1	1	1	***0.91***	***0.68***

(a)

Pc = 3.45 MPa (500 psia)	Direct Connect				Sea-Level Static	
	Case 1	Case 2	Case 3	Case 4	Case 5	Case 6
Rocket						
O/F	1.73	1.73	3.45	3.45	1.73	3.45
GO_2 Flow Rate kg/s	0.242	0.242	0.299	0.299	0.242	0.299
(lb/s)	(0.533)	(0.533)	(0.660)	(0.660)	(0.533)	(0.660)
JP-7 Flow Rate kg/s	0.140	0.140	0.087	0.087	0.140	0.087
(lb/s)	(0.309)	(0.309)	(0.191)	(0.191)	(0.309)	(0.191)
Equivalence Ratio	2	2	1	1	2	1
Duct						
Air Flow Rate kg/s	0.811	1.038	0.811	1.038	***0.59***	***0.58***
(lb/s)	(1.787)	(2.288)	(1.787)	(2.288)	***(1.30)***	***(1.28)***
GH_2 Flow Rate kg/s	0	0	0.024	0.030	0	0.024
in Afterburner (lb/s)	(0)	(0)	(0.053)	(0.067)	(0)	(0.053)
Overall Equivalence Ratio	1.28	1	1	1	***1.71***	***1.40***

Note: Bold italicized numbers were calculated after the experiments

(b)

reactant species variation in the secondary combustion, different stoichiometric O/F ratios were used to determine the overall stoichiometry for fuel-rich and stoichiometric rocket operations. Further flow rate and stoichiometry calculations are presented next.

To determine air flow rates, the composition of the rocket exhaust is required for the fuel-rich rocket operation cases (Cases 1, 2, and 5). Relevant mole fractions were obtained by

Table 2.7. Results of the CEA analyses for the fuel rich rocket cases at (a) $P_c = 1.38$ MPa (200 psia) and $P_c = 3.45$ MPa (500 psia).

Product	Molecular Weight	Mole Fraction	Mass Fraction	Mass Flow Rate	
				kg/s	(lb/s)
H	1.01	0.0001	0.0000	0.0000	(0.0000)
H_2	2.02	0.3278	0.0352	0.0054	(0.0119)
H_2O	18.02	0.1844	0.1768	0.0270	(0.0596)
CO	28.01	0.4161	0.6202	0.0948	(0.2091)
CO_2	44.01	0.0717	0.1679	0.0257	(0.0566)
Total	18.79	1.0000	1.0000	0.1529	(0.3371)

(a)

Product	Molecular Weight	Mole Fraction	Mass Fraction	Mass Flow Rate	
				kg/s	(lb/s)
H	1.01	0.0000	0.0000	0.0000	(0.0000)
H_2	2.02	0.3461	0.0371	0.0142	(0.0313)
H_2O	18.02	0.1661	0.1592	0.0608	(0.1340)
CO	28.01	0.3978	0.5929	0.2263	(0.4990)
CO_2	44.01	0.0900	0.2108	0.0805	(0.1774)
Total	18.79	1.0000	1.0000	0.3818	(0.8417)

(b)

running CEA [11] and are summarized in Table 2.7 along with further calculations. The CEA solutions indicate that there exist large percentages of H_2 and CO in the rocket exhaust. Atomic hydrogen also exists in the exhaust in a very small fraction. Thus, H_2 and CO are considered as constituting the excess fuel from the primary combustion in the rocket and, at the same time, the fuel for the secondary combustion with air in the duct. The stoichiometric secondary combustion is then represented by:

$$6.76\,H_2 + 8.25\,CO + 7.51\,(O_2 + 3.76\,N_2) \rightarrow 8.25\,CO_2 + 6.76\,H_2O + 28.23\,N_2 \qquad [2.3]$$

Air flow rates are selected so that overall equivalence ratios are 1.28 and 1 for Cases 1 and 2, respectively. The stoichiometric O/F ratio for the secondary combustion is:

$$Stoichiometric\ O/F = \frac{7.51\,MW_{O_2}}{6.76\,MW_{H_2} + 8.25\,MW_{CO}} \qquad [2.4]$$

where MW is the molecular weight of the individual species. The O/F ratios for Cases 1 and 2 were determined from:

$$O/F = \frac{Stoichiometric\ O/F}{Overall\ Equivalence\ Ratio} \quad [2.5]$$

Thus,

$$\dot{m}_{O_2} = (O/F)\cdot(\dot{m}_{H_2} + \dot{m}_{CO}) \quad [2.6]$$

The air flow rates were calculated from:

$$\dot{m}_{air} = \frac{\dot{m}_{O_2}}{Y_{O_2}} \quad [2.7]$$

where Y_{O2} is the mass fraction of oxygen in the air.

$$Y_{O_2} = \frac{MW_{O_2}}{MW_{O_2} + 3.76\,MW_{N_2}} \approx 0.77 \quad [2.8]$$

The air flow rates obtained from this analysis are summarized in Table 2.6.

For Cases 3, 4, and 6, the primary fuel is consumed completely because the rocket is operated at an equivalence ratio equal to unity. Again, overall equivalence ratios for the Cases 3 and 4 are required to match with the GH_2/GO_2 experimental series [2]. Since the reactants of the secondary combustion for these cases were gaseous hydrogen injected in the downstream afterburner and air, the overall equivalence ratios were determined based on H_2/O_2 stoichiometric O/F = 8.

2.4. GH_2/GO_2 Single and Twin Rocket Ejector Setups

The test setup used for the GH_2/GO_2 Twin rocket ejector was the same as that used for the JP-7/GO_2 experiments described earlier (Figs. 2.1 and 2.2). The setups differ in the rocket designs. For the GH_2/GO_2 Twin rocket ejector setup, an extensive set of experiments were conducted and reported in the addendum report [3], whereas GH_2/GO_2 Single rocket ejector experiments were reported to NASA in Refs. 2 and 3. Experiments reported in the addendum report [3] focused on 200 psia rocket operation. The goal of the current set of experiment is to extend the database obtained under the earlier study. Specifically, the current study emphasizes detailed static pressure measurements in the near rocket exhaust region, the unsteady nature of the flowfield and the effect of rocket spacing on performance.

For the Single rocket ejector experiments, the overall rocket assembly shown in Fig. 2.3 was used. However, the injector used for the rocket was not the one shown in Fig. 2.4 but the six-element shear coaxial design shown in Fig. 2.5. The rocket nozzle used was the 200 psia

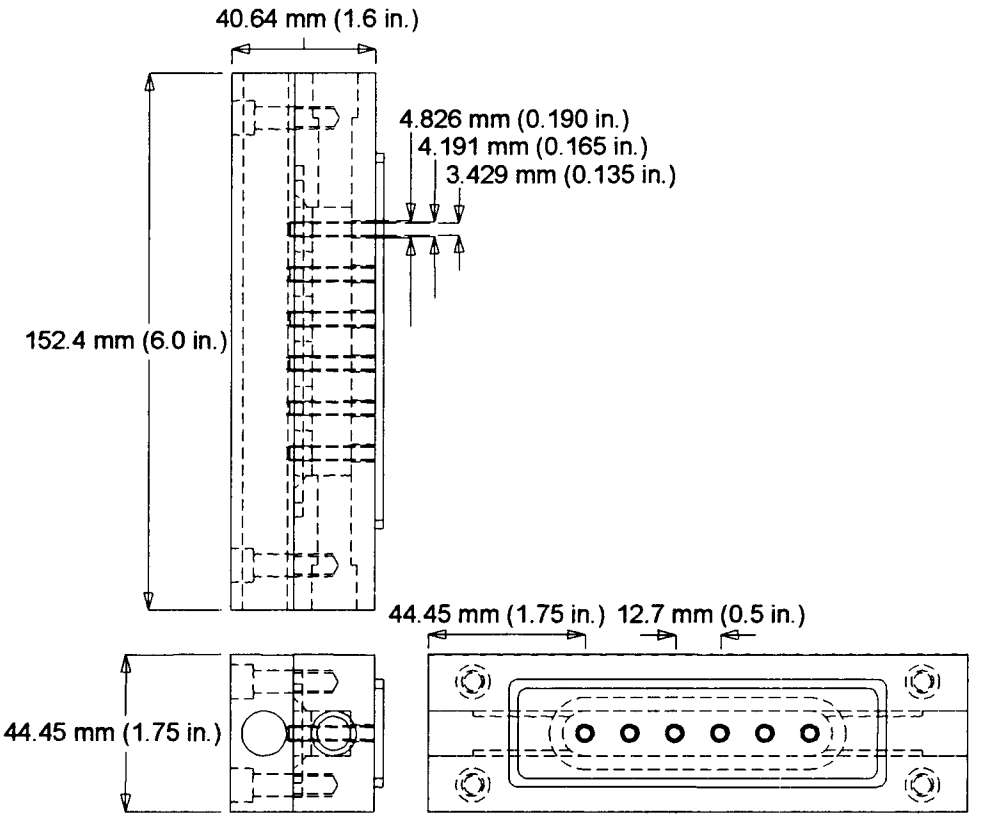

Fig. 2.5 Detail of injector body for Single rocket ejector experiments.

nozzle with a throat height of 0.1 and an exit height of 0.33 in. (area ratio of 3.3) which ideally expands the gas from the chamber pressure down to atmospheric pressure.

The Twin rocket ejector experiments used two smaller thrusters stacked in the RBCC setup as shown in Fig 2.6. Details of the Twin thruster design can be seen in Fig. 2.7.

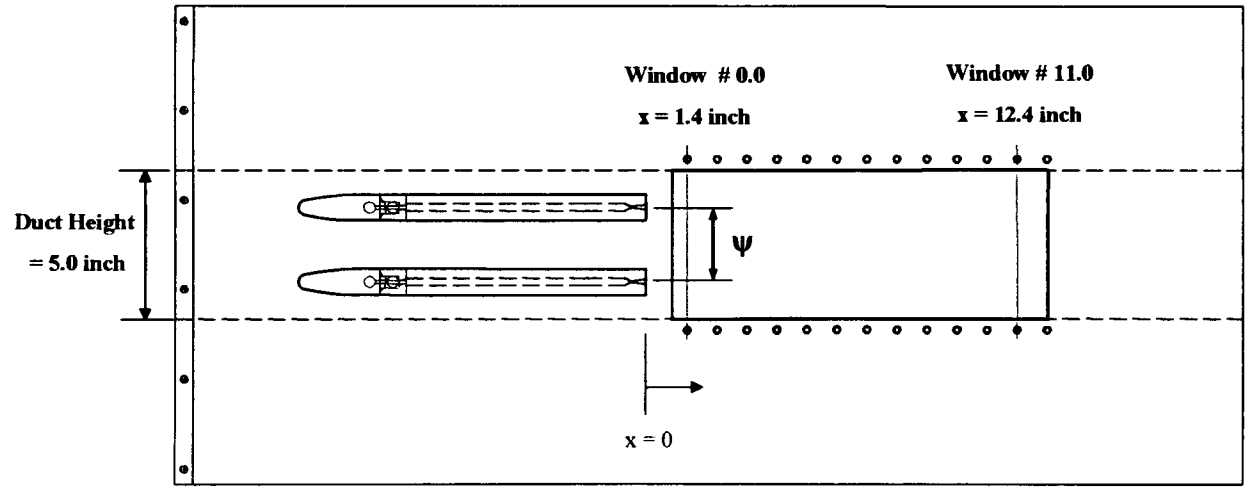

Fig. 2.6. Twin thruster spacing and optical access in the RBCC duct.

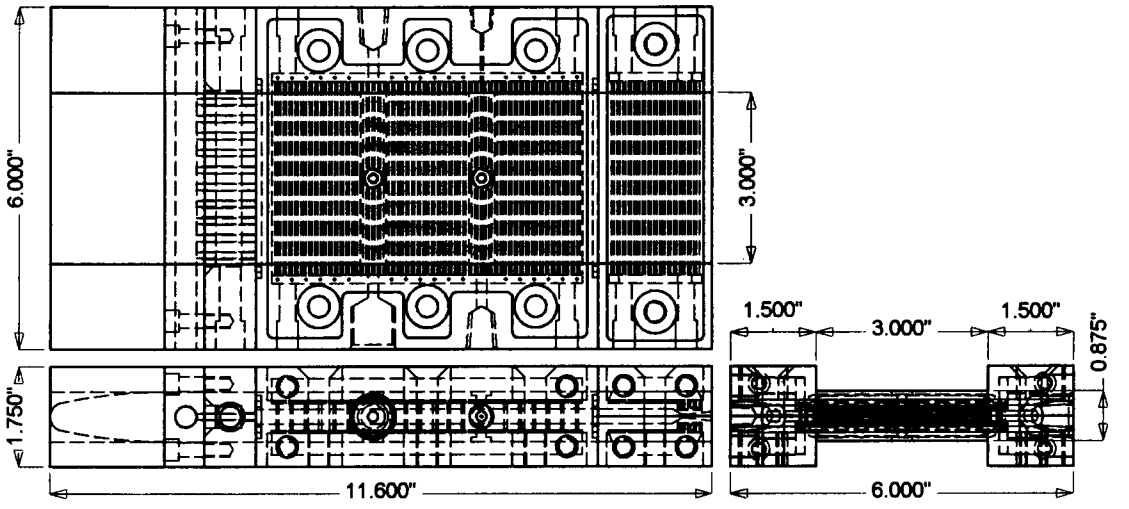

Fig. 2.7. Assembly drawing of single twin-rocket for GH_2/GO_2 propellants.

The incoming air flowed above and below the thrusters, as well as between them. Because of stress and cooling issues, these smaller thrusters were only operated up to a P_c of 200 psia. The blockage area, nozzle exit area, and rocket propellant flow rates of the twin thrusters combined equaled those of the single thruster ejector experiments [2, 3]. Thus a direct comparison of results can be made between the single and twin thruster configurations at a P_c of 200 psia.

Because the flow rate through each twin-thruster was half that of the single thruster, the size of the injector elements was reduced. The elements had the same basic shear coaxial design as the single thruster injector. The GO_2 post inner diameter (ID) was 0.106 in., the fuel annulus I.D. was 0.134 in., and its outer diameter was 0.156 in. In an effort to keep the thruster flow uniform across the duct, ten of these smaller elements were used per thruster. The drawing of the injector is shown in Fig. 2.8. The axial dimensions of the twin thrusters were identical to those of the single thruster. The height dimensions were exactly half those of the single rocket. A torch igniter was mounted to the side of each thruster combustion chamber.

The twin thrusters can be stacked in three different positions within the 5 in. high duct as shown in Fig. 2.9. The thruster centerline-to-centerline distance ("ψ" in Fig. 2.6) can be set at 1.75, 2.50 or 3.25 in. These spacings will be referred to as Twin A, B and C, respectively. Note that for this investigation, experiments were conducted for the Twin A (ψ = 1.75 in.) and Twin B (ψ = 2.50 in.) configurations. In all cases, the thrusters were equally spaced from the centerline of the duct, and their exit planes were at the same axial position (x = 0 in.). These

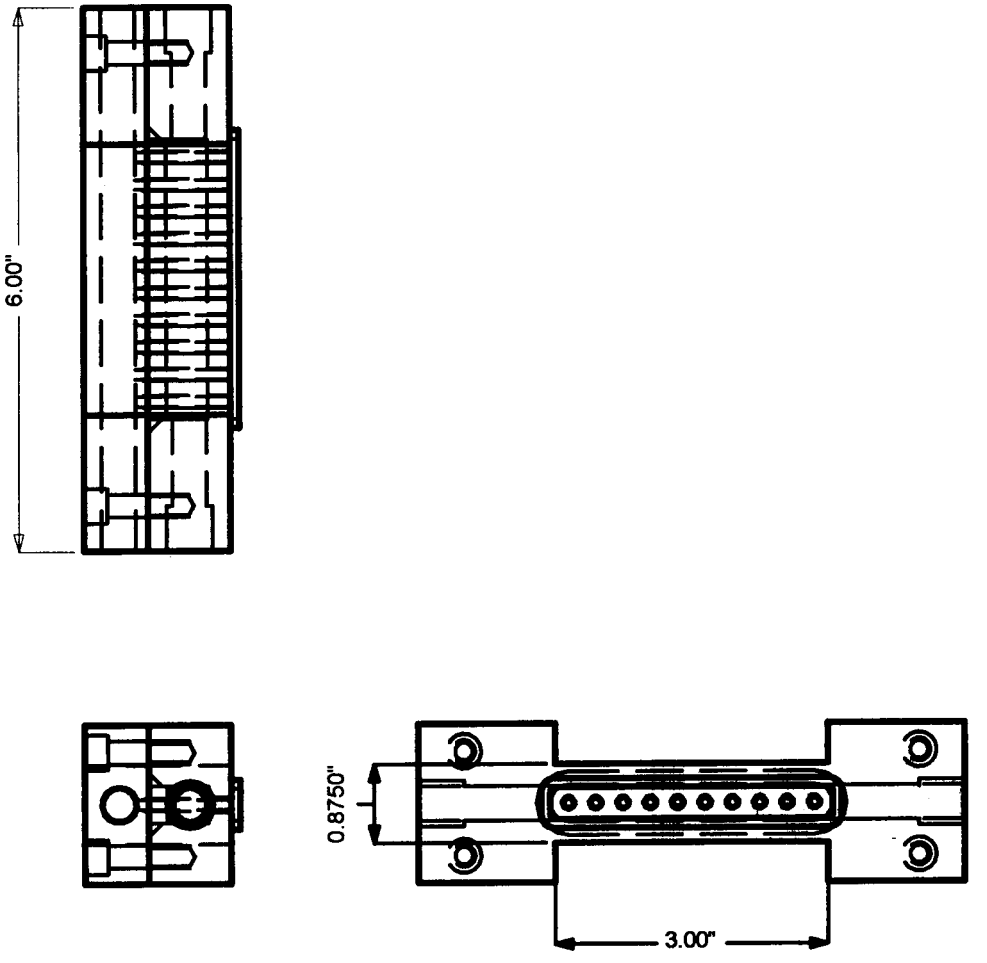

Fig. 2.8 Detail of injector body for Twin rocket ejector experiments.

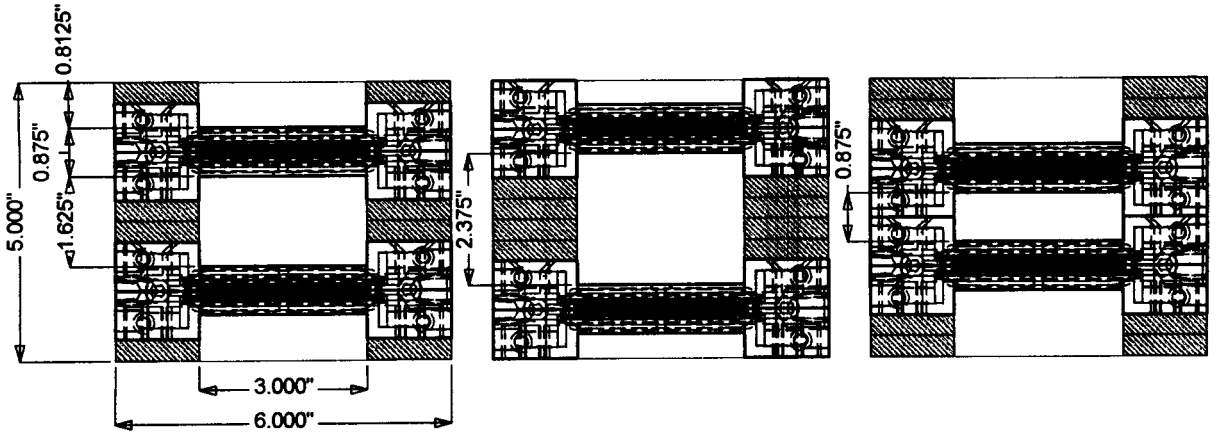

Fig. 2.9. Schematic showing possible twin rocket placements in RBCC duct.

Table 2.8. Summary of twin thruster spacing options.

		Far Spacing	Mid Spacing	Near Spacing
Thruster Centerline-to-Centerline Spacing, ψ	(in)	3.25	2.50	1.75
Nozzle Spacing Ratio, ψ/h	--	19.7	15.2	10.6
Thruster Centerline-to-Wall Spacing	(in)	0.875	1.250	1.625
Total Secondary Flow Area, A_2	(sq in)	9.75	9.75	9.75
Secondary Flow Area (Center), $A_{2,c}$	(sq in)	7.125	4.875	2.625
Secondary Flow Area (Near Walls), $A_{2,w}$	(sq in)	2.625	4.875	7.125
Ratio of Secondary Flow Areas, $A_{2,c}/A_{2,w}$	--	2.71	1.00	0.368

thruster spacing options provide a means for studying some of the geometric effects on the pumping and mixing processes. Table 2.8 summarizes the geometric variations that can be achieved at the different thruster spacings.

2.5. GH_2/GO_2 Single and Twin Rocket Ejector Operating Conditions

Twin thruster and a limited number of single thruster tests were conducted at the six operating points detailed in Table 2.9. The air box was installed at the front of the duct for Cases

Table 2.9. RBCC operating conditions for P_c = 200 psia.

	Direct Connect				Sea-Level Static	
	Case 1	Case 2	Case 3	Case 4	Case 5	Case 6
Simulated Flight Mach # ==>	**1.0**	**1.9**	**1.0**	**1.9**	**0.0**	**0.0**
Thruster O/F ==>	**4**	**4**	**8**	**8**	**4**	**8**
Thruster Flows						
Total GO_2 Flow Rate (lb_m/s)	0.188	0.188	0.243	0.243	0.188	0.243
Total GH_2 Flow Rate (lb_m/s)	0.0470	0.0470	0.0304	0.0304	0.0470	0.0304
Duct Flow						
Air Flow Rate (lb_m/s)	0.630	0.807	0.630	0.807	n/a	n/a
Afterburner Flow						
Total A/B GH2 Flow Rate (lb_m/s)	0.0	0.0	0.0184	0.0236	0.0	0.0184

1-4 (DC), and the open, converging inlet was used for Cases 5 and 6 (SLS). All tests in this study were conducted for rocket chamber pressure of 200 psia and a thruster mixture ratio (O/F) of 4 or 8. The propellant flow rates in each of the twin thrusters were half of the totals stated in the table. Because of the open inlet, the air flow rate for the SLS cases was not controlled. The actual flow rate was measured for each of the sea-level static configurations and cases, and those values are reported in Chapter 5.

3. INSTRUMENTATION AND DIAGNOSTICS

All RBCC combustion experiments were designed to evaluate the rocket-ejector flowfield. Diagnostics were employed to evaluate the static pressure distribution within the airduct, engine heat transfer, total engine thrust, and major species profiles. The following sections describe in detail the PC based static pressure measurement system, the heat flux gauges, the load cell, and the Raman spectroscopy setup used for line measurements of major species profiles within the airduct for the GH_2/GO_2 Single and Twin rocket ejector experiments.

3.1. Flowrate Measurements

Conventional propulsion measurement systems were used in the PERC test facility. The gaseous propellant flow rates were metered with critical flow venturis. The gas pressure and temperature were measured upstream of the venturis (P_1 and T_1), and the resulting mass flow rates were calculated using the choked flow equation. For the direct connect configuration, the flow rate of the air supplied to the duct was also metered with a venturi. Liquid flowrate (JP-7) was controlled in a similar manner using a cavitating venturi.

3.2. Standard Airduct Wall Static Pressure Measurements

The static pressure values along one side and the top wall of the airduct were recorded with a PC based data acquisition system. For the Diffusion and Afterburning (DAB) geometry, sixteen channels were located along the centerline of the top wall and the vertical side wall. Along the top wall, the pressure ports begin upstream of the rocket/ejector and terminate at the airduct nozzle plane. The side wall ports are located slightly downstream of the rocket/ejector nozzle plane and also extend to the airduct exit plane. The data was acquired at 6 Hz and each pressure port has a corresponding transducer. The system lines are equipped with a purge source of N_2 to clear the lines of condensation between runs. The location of each transducer (x, y, z coordinates with the origin at the center of the rocket exit plane) is indicated in Table 3.1. The axial coordinate refers to the x-direction with positive values corresponding to locations downstream of the rocket nozzle exit and negative values corresponding to the upstream region. The y-direction refers to the height of the duct and extends from -2.5 in. to +2.5 in. with the origin corresponding to the centerline height. The z-direction refers to the width of the duct and extends from -1.5 in. to +1.5 in. again with the origin corresponding to the duct centerline.

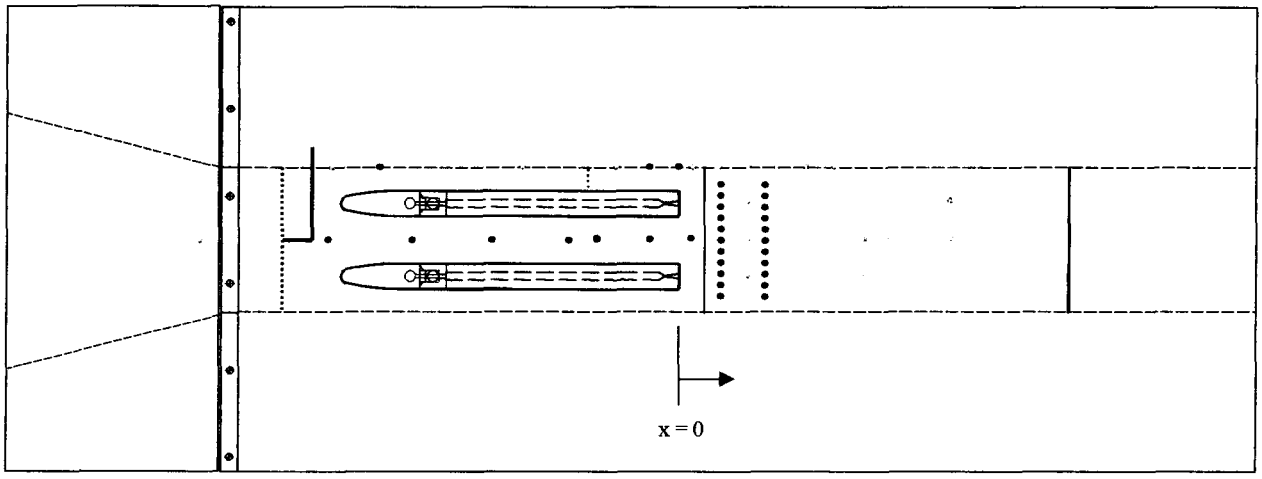

Fig. 3.1. Schematic showing additional measurement locations.

3.3. Additional Airduct Wall Static Pressure Measurements

One of the goals of the current investigation was to obtain detailed static pressure measurements in the near rocket exhaust region for the GH_2/GO_2 Twin rocket ejector setup. Consequently, one of the side walls of the setup was redesigned and fabrication for this purpose. In Fig. 3.1, theses modifications are summarized. A port for a traversable pitot static probe was implemented for velocity measurements upstream of the rockets. Additional pressure ports in the region between the two rockets and on the top wall (on top of rockets) were also implemented. Finally, the side wall downstream of the rockets was designed such that multiple arrays (up to three) of pressure ports (11 each) arranged in the transverse direction (y-coordinate) could be mounted at desired axial locations within the first 12 in. region downstream of the rocket exit plane. In Fig. 3.1, two transverse arrays of pressure ports indicated in red are evident. The data acquired from these ports were also recorded with the PC based data acquisition system.

3.4. Airduct Wall Heat Flux Measurements

Engine heat flux measurements were made for each operational case for both one side wall and the top wall of the airduct. Unlike the 32-channel static pressure system, only five heat flux gauges were available. The complete axial profiles were created by periodically moving the location of the gauges to compile a complete profile at each run condition. The top wall

Table 3.1. Typical static pressure measurement port locations.

Side Wall

Channel	X (inch)	Y (inch)	Z (inch)
1	8.53	0	-1.50
2	13.30	0	-1.50
3	15.53	0	-1.50
4	20.30	0	-1.50
5	22.30	0	-1.50
6	28.30	0	-1.50
7	35.08	0	-1.50
8	42.08	0	-1.50
9	49.15	0	-1.50
10	55.80	0	-1.50
11	62.40	-2.00	-1.50
12	67.32	2.50	-1.50
13	75.30	-2.50	-1.50
14	80.70	2.50	-1.50
15	87.30	-2.50	-1.50
16	92.55	0	-1.50

Top Wall

Channel	X (inch)	Y (inch)	Z (inch)
17	-11.70	2.50	0
18	-7.20	2.50	0
19	-2.70	2.50	0
20	0.65	2.50	0
21	3.90	2.50	0
22	7.90	2.50	0
23	11.15	2.50	0
24	15.80	2.50	0
25	21.80	2.50	0
26	33.80	2.50	0
27	42.39	3.01	0
28	49.12	3.49	0
29	55.11	3.92	0
30	61.09	4.35	0
31	74.35	5.00	0
32	85.85	5.00	0

Table 3.2. Heat flux measurement port locations.

Side Wall

Port	X (inch)	Y (inch)	Z (inch)
A	11.03	0	-1.50
B	18.03	0	-1.50
C	23.80	0	-1.50
D	26.80	0	-1.50
E	33.08	0	-1.50
F	40.08	0	-1.50
G	47.90	0	-1.50
H	54.30	0	-1.50
I	62.40	0	-1.50
J	75.30	0	-1.50
K	80.70	0	-1.50
L	87.30	0	-1.50

Top Wall

Port	X (inch)	Y (inch)	Z (inch)
M	2.90	2.50	0
N	8.90	2.50	0
O	11.90	2.50	0
P	20.30	2.50	0
Q	30.30	2.50	0
R	37.30	2.64	0
S	44.30	3.15	0
T	51.30	3.65	0
U	58.30	4.15	0
V	65.30	4.65	0
W	72.30	5.00	0
X	78.30	5.00	0
Y	84.30	5.00	0

locations correspond to the window locations. The top quartz window was replaced with a threaded copper blank to accept a heat flux gauge. The side wall locations were not at window locations and were also always along the airduct vertical centerline. The gauges were 0.5 in. Gardon type units that acquired heat flux data at 200 Hz. The heat flux measurement locations are summarized in Table 3.2.

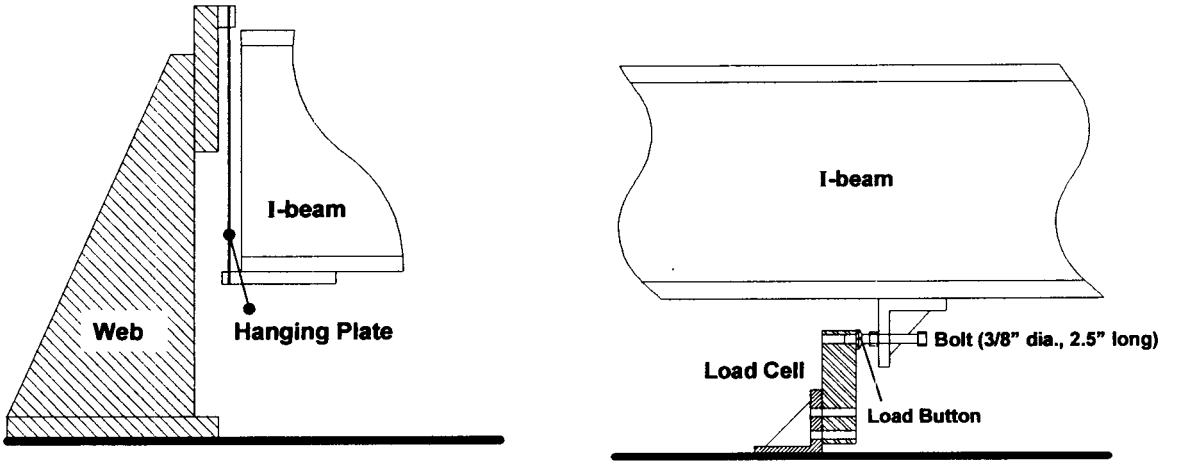

Fig. 3.2. Thrust measurement setup. (a) End of the I-beam and (b) load cell.

3.5. Engine Thrust Measurements

A calibrated load cell with a full scale range of 1000 lbf was used to measure the thrust during each firing. The entire RBCC test rig is mounted on an I-beam. The I-beam is bridged to a fixed web by a metal plate on each side as shown in Fig. 3.2. This mounting method provides a "hanging" condition to the I-beam and allows the measurement of thrust in terms of displacements of the I-beam using the load cell, which is mounted underneath the I-beam. The load cell was manually pre-loaded at the beginning of a day to provide a good mechanical connection. Signals (in volts) were acquired at 50 Hz and scaled to thrust (37733.0 lbf/volt) using the available LabVIEW software. The scaling factor was based on the calibration of the system.

3.6. Ejected Air Flow Rate Measurements

For SLS conditions, viz. Cases 5 and 6, the ejected airflow rate was estimated from a pressure differential measurement between a port in the inlet section and atmospheric pressure. The pressure measurement location is shown in Fig. 3.3. The port is located 9.67 in. downstream of the entrance plane of the open inlet (labeled as Location 3). The pressure differential, ΔP, was measured using a high accuracy pressure transducer. The ejected mass flowrate was then calculated using Bernoulli's equation and the assumption of one-dimensional flow.

For the GO_2/GH_2 Twin rocket configurations at SLS conditions, the pitot probe shown in Fig. 3.1 was also used to measure the transverse velocity profile in the inlet section of the rocket

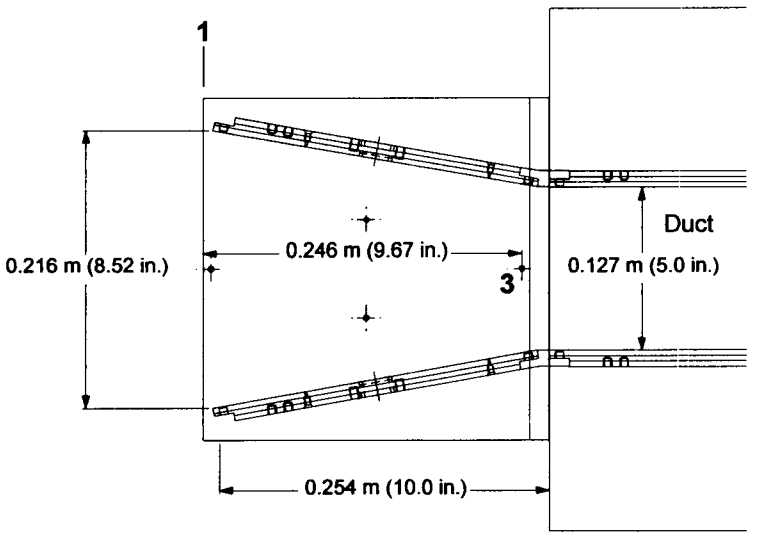

Fig. 3.3. Open inlet (SLS) showing pressure transducer location (labeled as "3") for ejected air calculations.

ejector system by traversing the probe in the normal (y) direction. Integration of the velocity profile was also used to establish, with more accuracy, the ejected air mass flow rate.

3.7. High Frequency Pressure Measurements

For the GH_2/GO_2 rocket ejector configuration, high frequency pressure measurements were also made in the constant area combustor section of the RBCC duct to assess the unsteady behavior of the flowfield. The measurements were made using PCB/Piezotronics sensors (Model 113A21) mounted in water-cooled jackets. Up to four transducer signals per test were recorded with a LeCroy Model 6810 Waveform Recorder. AC coupling was used to acquire only the fluctuating component of the pressure signals. The transducers have a natural frequency of ~500 kHz, and a flat frequency response curve to at least 100 kHz. Data was recorded at 50,000 samples per second, which resulted in an effective frequency measurement range of 0-25 kHz. The maximum operating pressure of the transducers is 200 psi, and they have a resolution of 0.003 psi.

High frequency pressure measurements were made primarily at x = 2.4 in. (downstream of the rocket exit plane). Adapter plates allowed the transducers to be mounted on the –Z side wall of the duct at nine transverse positions (y = 0.0, ±0.50, ±0.88, ±1.25, ±1.75 in.). Measurements were also made on the top and bottom walls (x = 2.4 in., y = ±2.50 in., z = 0.0 in.). Figure 3.4 shows the location of these 11 measurements, and Fig. 3.5 shows the

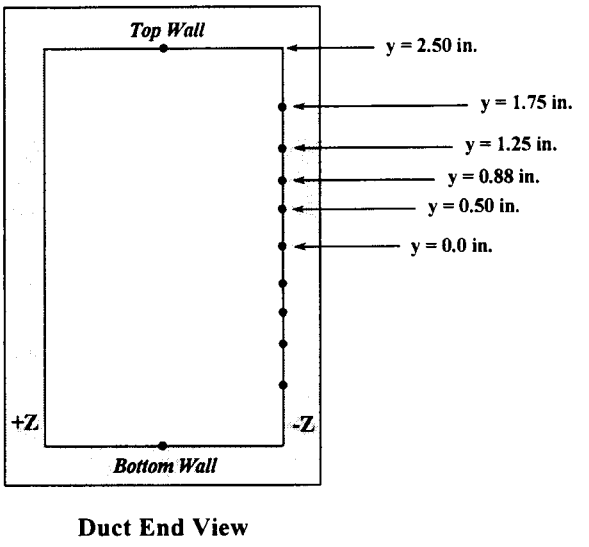

Fig. 3.4. High frequency pressure measurement locations.

basic geometry of a transducer and water jacket mounted on the side wall. In some cases, frequency measurements were also made at several axial locations along the top wall (y = 2.50 in.), the –Z side wall (y = 0.0 in.), or the +Z side wall (y = 0.0 in.).

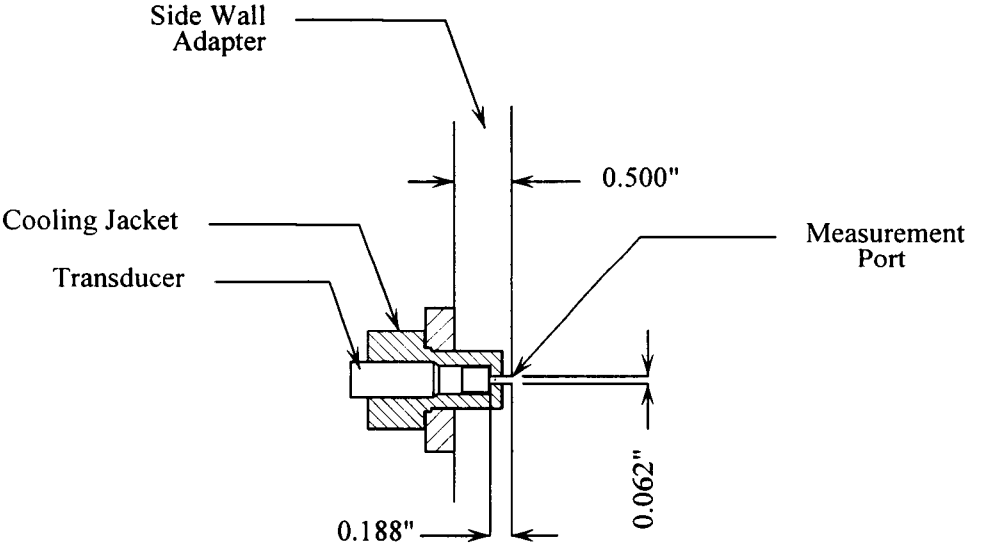

Fig. 3.5. High frequency pressure transducer mounting configuration.

4. JP-7/GO_2 ROCKET EJECTOR RESULTS

This chapter describes the JP-7/GO_2 RBCC rocket ejector results for the Diffusion and Afterburning (DAB) configuration. Results include static pressure and wall heat flux profiles, and overall engine thrust. The rocket was operated at a target chamber pressure of 500 psia for the sea level static (SLS) case. Target flow rates of all the experimental cases were previously discussed in Chapter 2 (see Table 2.6).

4.1 Rocket c* Efficiency

JP-7/GO_2 rocket ejector experiments reported in the addendum report [3] were conducted for a target rocket chamber pressure of 200 psia. Rocket performance for these experiments showed that for stoichiometric (O/F = 8) and fuel-rich operation (O/F = 4), the c* efficiencies were about 99% and 92%, respectively. These performance numbers are not surprising since the injector was designed for stoichiometric operation. For the current rocket ejector experiments at a target chamber pressure of 500 psia, the corresponding c* efficiencies were 86.5% and 84.6% for stoichiometric (Case 6, O/F = 8) and fuel-rich operation (Case 5, O/F = 4), respectively. Since the c* efficiencies for 500 psia rocket operation were relatively low, only a limited number of experiments were performed for this case. Based on discussions with NASA MSFC and their needs, it was decided that instead of redesigning the rocket injector (to yield higher efficiencies), the program would benefit from redirecting the remaining resources to conduct additional experiments for the GH_2/GO_2 twin rocket ejector configuration. The results obtained for the limited number of experiments conducted for this task are discussed next.

4.2 Static Pressure Measurements

The static pressure profiles for the SLS cases at the two target rocket chamber pressures, viz. 200 [3] and 500 psia, are contrasted in Fig. 4.1. The trends for the 200 psia rocket pressure are as follows: For the stoichiometric rocket case (Cases 6), the static pressure rises as the primary and secondary flows mix in the mixer section until the point where significant mixing has occurred (x ~ 20 in.). Once the mixing has reached near completion, the static pressure level stays constant in the mixer section. The mixed fluid, then, enters the diffuser section, in which the static pressure increases due to flow deceleration. GH_2 is injected at the end of the diffuser section. The heat addition due to the secondary combustion in the afterburner results in lowering

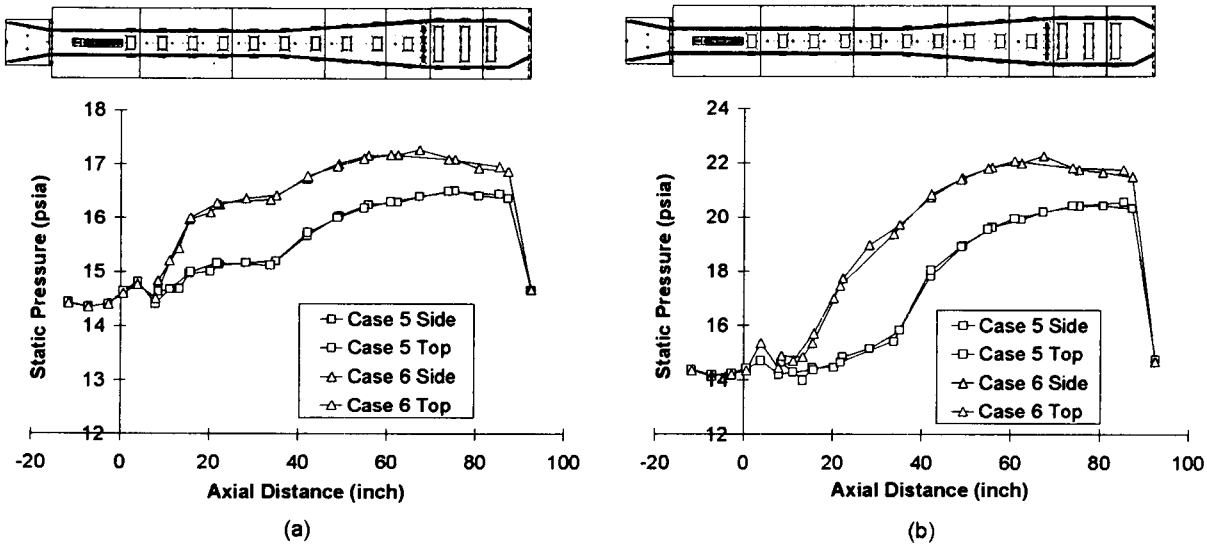

Fig. 4.1. Static pressure profiles for SLS Cases. (a) P_c = 200 psia, (b) P_c = 500 psia.

of the pressure. However, the secondary combustion tends to increase the back pressure throughout the duct. Thus the RBCC engine can be operated at a higher static pressure level, a desirable operating condition for a combustion device, with the afterburner operational.

The significant difference between the stoichiometric and fuel rich rocket operation cases (Cases 5 and 6) is the level of the static pressure. As discussed above, it is higher for the stoichiometric rocket operation case because of the afterburner operation. The pressure rise in the mixer section also differs due to the rocket stoichiometry. Since the secondary combustion between excess fuel and the air occurs in the mixer section when the rocket is operated at a fuel rich O/F, the resulting heat release affects the pressure rise in this region. The constant pressure profile observed in the afterburner section for the fuel rich rocket operation case occurs because no additional combustion takes place. At both rocket stoichiometries, the flow is accelerated through the converging nozzle so that the static pressure drops to atmospheric pressure at the exit plane.

The results shown in Fig. 4.1 also illustrate differences in the static pressure profile due to the rocket chamber pressure. The obvious difference is the static pressure level. A higher pressure level is achieved at P_c = 500 psia. The trends of the static pressure profiles are similar for both chamber pressures except in the mixer section. At P_c = 200 psia, the static pressure in the mixer section became constant once the mixing is complete. On the other hand, the static pressure keeps increasing in the entire mixer section for the target P_c = 500 psia cases, rather

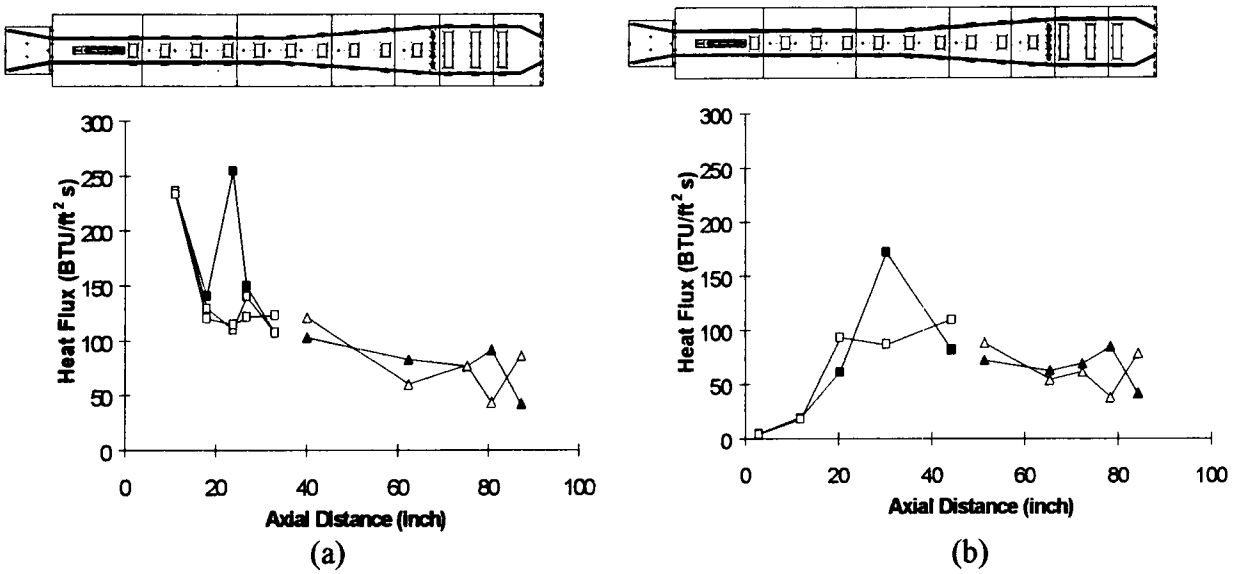

Fig. 4.2. Case 5 heat flux profiles at target P_c = 500 psia. (a) Side wall measurements, and (b) top wall measurements.

than staying at a constant level. This indicates that mixing is not complete within the mixer section.

4.3. Heat Flux Measurements

The heat flux profile for Case 5 at the target chamber pressure of 500 psia is shown in Fig. 4.2. For the side wall measurements, the heat flux profile shows an axial decrease from the rocket exit plane, whereas the top wall profile shows that the heat flux increases throughout the

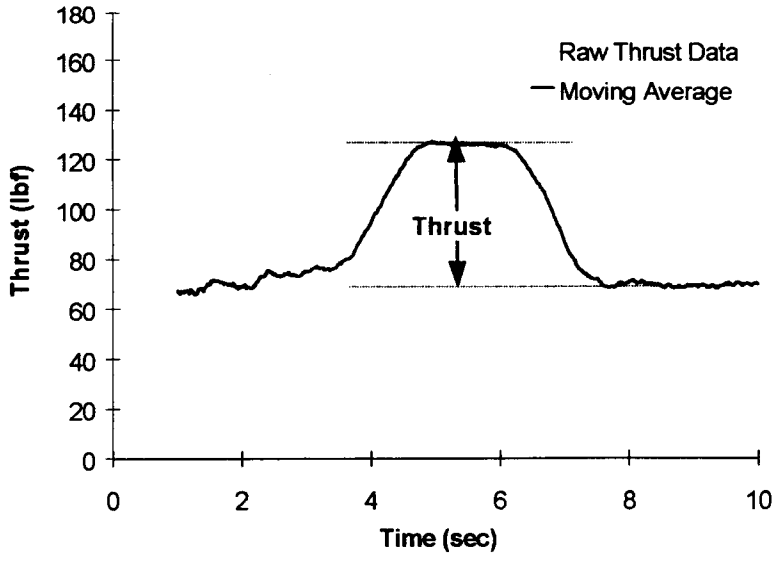

Fig. 4.3. Example of raw thrust data (200 psia case) and its moving average.

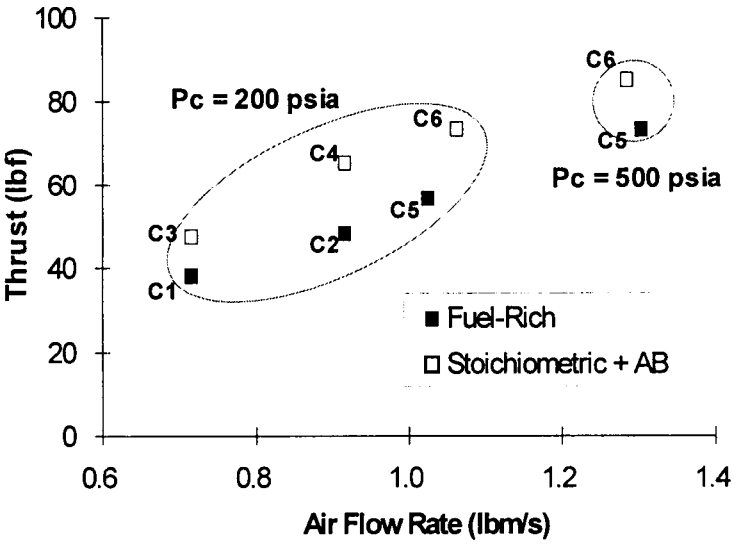

Fig. 4.4. Average thrust values versus air flow rate.

mixer section and then decreases slightly. These results are qualitatively similar to results reported for 200 psia rocket operation in the addendum report [3].

4.4. Thrust Measurements

An example of the raw voltage versus time data for thrust measurements is shown in Fig. 4.3. A moving average of 50 samples is also indicated in the figure. The averaging procedure reduces the level of noise while maintaining the magnitude of the data. The average thrust is obtained from the difference in load cell voltage readings at steady state during the hot fire (t ~ 6 s) and after the firing (t ~ 9 s), and the calibration.

The thrust data for both target rocket pressures (200 psia and 500 psia) are plotted versus the air flow rate in Fig. 4.4. Note that Cases 1-4 are for DC configurations, whereas Cases 5 and 6 are for the SLS configuration. For the SLS cases, the ejected air flow rate is measured (see Table 4.1), whereas for the DC cases, the air flow rate is supplied. These results show that

Table 4.1. Air flow rates for SLS cases (cases 5 and 6).

Pc	Air Flow Rate, kg/s (lb/s)	
	Case 5	Case 6
1.38 MPa (200 psia)	0.47 (1.03)	0.48 (1.06)
3.45 MPa (500 psia)	0.59 (1.30)	0.58 (1.28)

although both the ejected air flow rate and thrust values are higher for the target 500 psia rocket operation than the 200 psia case, the magnitudes do not scale with the rocket pressure. Clearly, the low c* efficiencies noted for the target 500 psia rocket cases affect the overall performance of the RBCC rocket ejector.

5. GH_2/GO_2 SINGLE AND TWIN ROCKET EJECTOR RESULTS AND ANALYSIS

In this chapter, results for the Twin rocket ejector RBCC setup are presented and discussed. These experimental results (referred to as the Phase II test series results) complement the earlier Twin rocket results (Phase I test series) that were described in the earlier addendum report [3]. All tests were conducted at sea-level static conditions, specifically Case 5 (O/F = 4) and Case 6 (O/F = 8) as described in Table 2.9. The primary objective of this test series was to compare the Twin thruster operating characteristics at different centerline spacings. A second objective was to study some of the effects observed in Phase I [3] in more detail, including: (1) the apparent differences between the secondary mass flow rates predicted by the CFD model (complementary calculation by NASA MSFC [12,13]) and the measured values; (2) the differences in thrust and secondary flow rate between the Single and Twin B configurations; (3) the transverse static pressure gradients downstream of the thruster exit plane; (4) the biasing of the Twin B primary flow streams toward the top and bottom walls; and, (5) the seemingly random shot-to-shot oscillations in the nitrogen Raman signal in the region between the Twin thrusters downstream of the thruster exit plane. Each of these points will be addressed separately in the sections that follow.

Tests were conducted with both the Twin A (Ψ = 1.75 in.) and Twin B (Ψ = 2.50 in.) configurations. A limited number of single thruster tests were conducted at the end of the test series at O/F = 8 only. Phase II measurements to be discussed in this section include thrust, static pressure, secondary inlet velocity and mass flow rate, and high frequency pressure fluctuations. Tables 5.1 through 5.3 summarize the types of measurements made for the Twin A, Twin B, and Single configurations, respectively. A shaded box in the tables indicates that measurements were not made at that condition. All the results identified in these tables are archived on the accompanying DVD. Test dates, and in some cases specific test numbers, are identified to simplify the process of accessing data files on the DVD.

The key results from the Phase II test series show that the Twin B configuration entrains ~ 20% more air than the Twin A or Single configurations, and as a result it produces ~ 8% more thrust with no additional fuel. In addition, the Twin B case has the shortest primary/secondary mixing length followed by the Twin A case. The single thruster configuration has the longest

Table 5.1. Data summary table for the Twin A configuration.

DATA TYPE	Case 5	Case 6
Static Pressure 2-D Maps	**Date: 11/19/02** *Test No.: 8-13, 15-20, 22-27, 29-35*	**Date: 11/12/02** *Test No.: 9-18, 22-28*
		Date: 11/19/02 *Test No.: 8-15, 17-22, 24-29*
Static Pressure Axial Profiles	**Date: 12/19/02** *Test No.: 9-17*	**Date: 11/12/02** *Test No.: 9-18, 22-28*
		Date: 12/20/02 *Test No.: 8-19*
Raman All Species		
X = 1.4 in.		**Date: 1/29/03**
X = 2.4 in.	**Date: 12/19/02**	**Date: 12/20/02**
X = 3.4 in.		**Date: 2/3/03**
X = 7.9 in.	**Date: 1/10/03**	**Date: 1/14/03**
Nitrogen Only		
X = 2.4 in.		**Date: 11/12/02**
High Frequency		**Date: 3/11/03**
		Date: 3/13/03
		Date: 3/24/03
Thrust	**Date: 11/19/02** *Test No.: 8-38*	**Date: 11/12/02** *Test No.: 9-40*
	Date: 12/19/02 *Test No.: 8-30*	**Date: 11/14/02** *Test No.: 8-32*
		Date: 12/20/02 *Test No.: 8-20*
Air Velocity & Mass Flow Rate	**Date: 11/19/02**	**Date: 11/12/02**
	Date: 12/19/02	**Date: 11/14/02**
	Date: 2/21/03	**Date: 12/20/02**

NOTE: Shaded boxes indicate no measurements were made

Table 5.2. Data summary table for the Twin B configuration.

DATA TYPE	Case 5	Case 6
Static Pressure 2-D Maps	**Date: 10/10/02** *Test No.: 9-15*	**Date: 10/16/02** *Test No.: 10-18*
	Date: 10/11/02 *Test No.: 10-15*	**Date: 10/17/02** *Test No.: 8-17*
	Date: 10/14/02 *Test No.: 8-15*	**Date: 10/18/02** *Test No.: 8-23*
	Date: 10/24/02 *Test No.: 10-30*	**Date: 10/29/02** *Test No.: 8-15, 22-29*
	Date: 10/28/02 *Test No.: 8-16, 29-36*	**Date: 11/01/02** *Test No.: 8-28*
Static Pressure Axial Profiles	**Date: 9/16/02** *Test No.: 9-12, 13-18*	**Date: 9/9/02** *Test No.: 11-15*
	Date: 9/19/02 *Test No.: 8-18, 19-28*	**Date: 9/12/02** *Test No.: 9-12, 13-16*
Raman Nitrogen Only		
X = 2.4 in.	**Date: 11/1/02**	**Date: 11/1/02**
X = 3.4 in.	**Date: 10/11-15/02**	**Date: 10/16-17/02**
X = 5.4 in.	**Date: 10/24/02**	**Date: 10/18/02**
X = 7.9 in.	**Date: 10/28/02**	**Date: 10/29/02**
High Frequency		**Date: 4/3/03, 4/4/03, 4/7/03** **Date: 4/15/03 (Pc=150 psia)**
Thrust	**Date: 10/14/02** *Test No.: 8-34*	**Date: 10/16/02** *Test No.: 9-23*
	Date: 10/15/02 *Test No.: 7-16*	**Date: 10/17/02** *Test No.: 8-26*
	Date: 10/24/02 *Test No.: 10-29*	**Date: 10/18/02** *Test No.: 8-23*
Air Velocity & Mass Flow Rate	**Date: 9/19/02, 9/23/02** **Date: 10/9/02, 10/10/02, 10/11/02** **Date: 10/14/02, 10/15/02** **Date: 10/24/02, 10/28/02** **Date: 11/01/02**	**Date: 10/16/02** **Date: 10/17/02** **Date: 10/18/02** **Date: 10/29/02** **Date: 11/01/02**

NOTE: Shaded boxes indicate no measurements were made

Table 5.3. Data summary table for the Single configuration.

DATA TYPE	Case 5	Case 6
Static Pressure 2-D Maps		**Date: 5/7/03** *Test No.: 9-14, 16-22, 24-29*
Static Pressure Axial Profiles		**Date: 5/5/03** *Test No.: 16-21, 25-30*
High Frequency Pressure		**Date: 5/5/03** **Date: 5/7/03**
Thrust		**Date: 5/7/03** *Test No.: 9-26*
Air Velocity & Mass Flow Rate		**Date: 5/5/03** **Date: 5/7/03**

NOTE: Shaded boxes indicate no measurements were made

mixing length. The high frequency pressure measurements show that the Twin B configuration sets up a strong acoustic coupling in the vertical transverse (y) direction. The available experimental results indicate that this acoustic coupling is responsible for the more efficient entrainment and mixing for the Twin B configuration. The following sections of this chapter review the details of these findings.

5.1. Thrust Measurements

Unlike the Phase I thrust measurements that were recorded at 50 samples per second, the Phase II thrust measurements were recorded at 200 samples per second. A thrust profile from a typical Phase II test is shown in Fig. 5.1. The steep rise in thrust occurs when the thrusters are ignited at ~3.2 sec., and the thrust decays after the shutdown sequence is initiated at 5.0 sec. Scatter in the data points was smoothed using a 100 point moving average. Since a pre-load was always applied to the load cell, the measured thrust was the difference between an average value before ignition ($2.0 < t < 2.5$ sec.) and an average value during the steady state portion of the test ($4.5 < t < 5.0$ sec.).

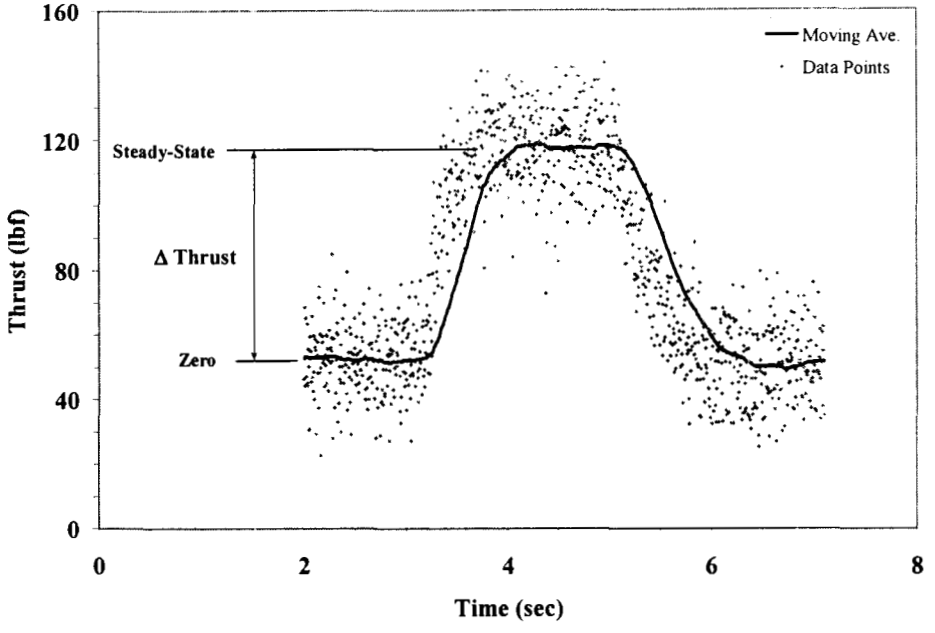

Fig. 5.1. Typical thrust profile (original data points plus moving average).

Table 5.4 summarizes the Phase II thrust measurements for each configuration and set of run conditions. This table includes the average thrust and standard deviation for each set of tests, and the total number of tests at each operating point. The average thrust values for the Single and the Twin A configurations are nearly identical. The average thrust for the Twin B configuration is ~7-9% higher than the other two configurations. Since the propellant flow rates were the same for all three configurations, this increase in thrust indicates that the Twin B configuration entrains more air than the other two configurations. Confirmation of this trend is seen in the inlet velocity measurements (Section 5.3.1).

Since the measured thrust increase was relatively small (~ 8%), a statistical analysis was performed to determine the level of significance of these results. When considering the difference between the mean values of two samples ($\Delta = \overline{X}_1 - \overline{X}_2$), the limits of a confidence interval ($\pm \alpha$) can be calculated. For sample sizes (N_i) of 30 or greater, the samples are assumed to have a normal distribution. The confidence interval for the normally distributed difference between two sample means is given by Scheaffer and McClave [14] as:

$$\Delta \pm \alpha = \left(\overline{X}_1 - \overline{X}_2\right) \pm z_c \cdot \sqrt{\frac{\sigma_1^2}{N_1} + \frac{\sigma_2^2}{N_2}} \qquad [5.1]$$

where

Table 5.4. Summary of Phase II thrust measurements.

Thruster Configuration	Thruster Spacing Ψ (in.)	Case 5 (O/F = 4) Ave. Thrust X_i (lb_f)	Std. Dev. σ_i (lb_f)	Total Tests N_i	Case 6 (O/F = 8) Ave. Thrust X_i (lb_f)	Std. Dev. σ_i (lb_f)	Total Tests N_i
Single	--				**66.7**	2.45	15
Twin A	**1.75**	**54.9**	1.75	36	**66.1**	1.19	45
Twin B	**2.50**	**59.6**	1.29	54	**71.3**	1.60	50
Comparisons							
1) Single vs. Twin B							
Nominal Thrust Difference (Δ) =					**4.51**	lb_f	
% Difference =					6.8	%	
Minimum Δ Thrust (95% confidence) =					**3.60**	lb_f	
% Difference (95% confidence) =					5.4	%	
2) Twin A vs. Twin B							
Nominal Thrust Difference (Δ) =		**4.74**	lb_f		**5.17**	lb_f	
% Difference =		8.6	%		7.8	%	
Minimum Δ Thrust (95% confidence) =		**4.18**	lb_f		**4.70**	lb_f	
% Difference (95% confidence) =		7.6	%		7.1	%	

NOTE : Shaded boxes indicate no information is available

$\Delta \equiv$ difference of the means, $(\bar{X}_1 - \bar{X}_2)$

$\alpha \equiv$ confidence limit

$\bar{X}_i \equiv$ sample mean

$\sigma_i \equiv$ sample standard deviation

$N_i \equiv$ number of samples

$z_c \equiv$ confidence coefficient

When a normal distribution cannot be assumed ($N_i < 30$), the Student's t-distribution statistics are used. In this case the confidence interval becomes:

$$\Delta \pm \alpha = \left(\bar{X}_1 - \bar{X}_2\right) \pm t_c \cdot \sqrt{\frac{1}{N_1} + \frac{1}{N_2}} \cdot \sqrt{\frac{N_1\sigma_1^2 + N_2\sigma_2^2}{\nu}} \qquad [5.2]$$

where

$\nu \equiv$ degrees of freedom, $(\nu = N_1 + N_2 - 2)$

$t_c \equiv$ confidence coefficient

In the present case, only the minimum limit of the thrust difference $(\Delta - \alpha)$ is of interest, so the confidence coefficients are based on a "one-tailed" distribution. At the 95% confidence level, the confidence coefficients are 1.645 for a normal distribution and 1.67 for a t-distribution with $\nu \sim 60$. Equation 5.2 was used for the Single/Twin B comparison, and Equation 5.1 was used for the Twin A/Twin B comparisons.

The results of the statistical analysis are also summarized in Table 5.4. At the 95% confidence level, the minimum thrust difference between the Twin B configuration and the other two configurations is still ~ 5.5-7.5%. Therefore, it is highly probable that the observed difference in thrust level indicates a real change in the flow field for the Twin B configuration. However, the thrust data alone does not provide any physical insight into the reason for the increased air entrainment for the Twin B configuration.

The thrust differences between Twin B and the other two configurations would be even greater than the reported values if all the tests were performed at the same equivalence ratio (Φ). Because the Twin B configuration entrains more air than the other two cases, its Φ is lower than those cases. If additional fuel had been injected in the afterburner for the Twin B tests to match the Φ of the Single and Twin A tests, the higher energy release would have generated more thrust than the reported Twin B value. It should be noted that the additional energy release would also raise the afterburner pressure. As a result, the ejector would not be able to entrain as much air because of the higher back pressure.

The effects of afterburner fuel flowrate are illustrated in Fig. 5.2, which presents normalized results from a set of Twin A tests. In these tests, the afterburner operated with 100, 89, and 84 percent of its nominal fuel flow rate. At the lowest flow rate (84%), the thrust was ~88% of its baseline value, and the air mass flow rate was 104% of its baseline value. The opposite trends would occur if the afterburner fuel flow was increased rather than decreased, that is thrust would increase and air flow would decrease. These tests were conducted only for the Twin A configuration, but similar trends should occur with the Twin B configuration.

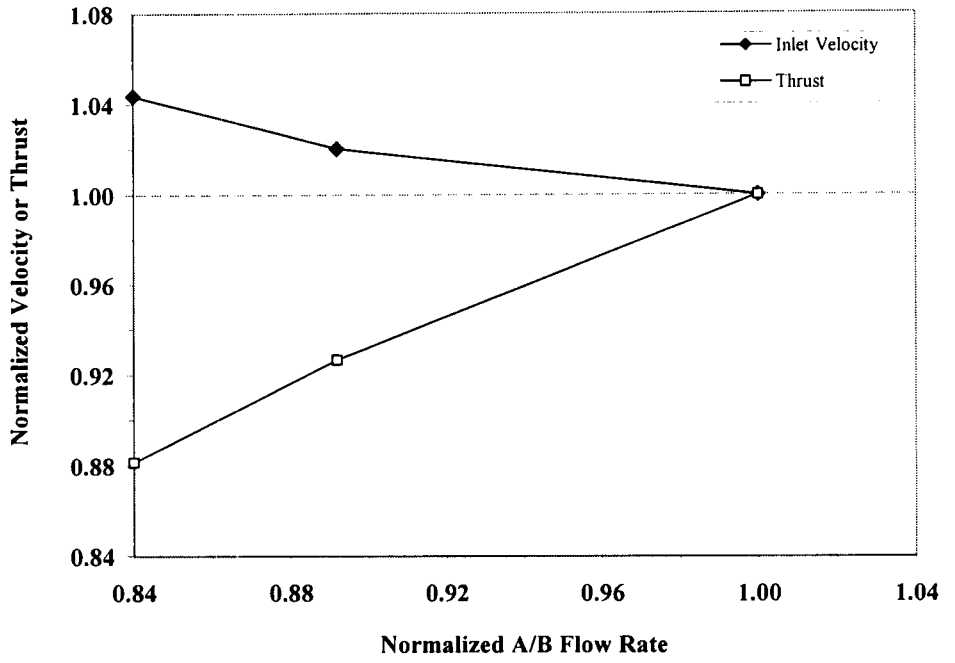

Fig. 5.2. Normalized inlet velocity and thrust as a function of afterburner fuel flow rate (Twin A, O/F = 8).

5.2. Static Pressure Measurements

Based on the Phase I results, several changes were made to the static pressure measurement locations. Ports were added between the thrusters (x = -12.0, -11.18, -8.60, -1.18 in., y = 0.0 in., z = -1.5 in.) for the Twin B configuration in order to characterize the flow split between the center region ($A_{2,center}$) and the near-wall regions ($A_{2,upper}$ and $A_{2,lower}$). Physical constraints prevented static pressure measurements from being made between the thrusters for the Twin A configuration. Additional static pressure measurements ports were added on the top and side walls immediately downstream of the thruster exit plane to provide a more detailed view of the mixing process for all three configurations.

In order to develop a better understanding of the transverse pressure differences observed in the Phase I testing, modular side wall sections were modified to accommodate 11 static pressure ports in a vertical column (see Fig. 3.1). These ports were located at y = 0.0, ± 0.50, ± 0.875, ± 1.25, ± 1.625, and ± 2.00 in. Three of these pressure port columns were available, and they were installed on the +Z side wall (z = +1.5 in.) at various axial locations between x = 1.15 and 12.65 in.

5.2.1. Axial Static Pressure Measurements

Figures 5.3 through 5.5 depict the Case 6 axial static pressure profiles for the Twin B, Twin A, and Single configurations, respectively. Each figure includes three profiles, viz., the pressure along the top wall centerline, the -Z side wall (z = -1.5 in.) centerline, and the +Z side wall (z = +1.5 in.) centerline. The +Z side wall data pressure was only measured in the region immediately downstream of the thruster exit plane. The other two profiles typically extend from upstream of the thrusters (x ~ -12 in.) to the duct exit (x = 93.3 in.).

Figure 5.3 shows that in the region upstream of x = 0.0 in. for the Twin B configuration, the static pressure in $A_{2,upper}$ (top wall) is higher than the pressure in $A_{2,center}$ (side wall, +Z) This pressure difference is approximately 1.5 psid just upstream of the thruster exit plane. Assuming the flows in these two regions accelerate isentropically from the same inlet conditions, the flow in $A_{2,center}$ is at a higher velocity than the flow in $A_{2,upper}$. The velocity measurements and the corresponding air flow rates in these regions are discussed in Section 5.3.2. Although the Twin A configuration does not have pressure ports between the thrusters, there are side wall measurements just upstream (x = -16.5 in.) and downstream (x = 0.3 in.) of the thruster bodies. Since those pressures (see Fig. 5.4) are approximately equal to the corresponding values for the Twin B configuration, the Twin A side wall profile from x = -16.5 to 0.3 in. should be similar to

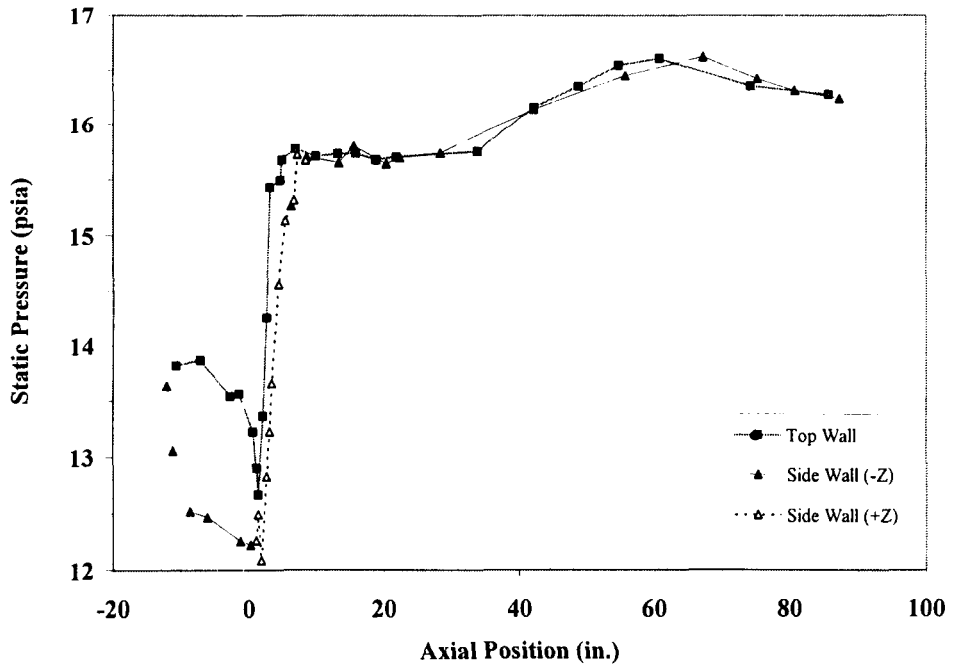

Fig. 5.3. Axial pressure profile for the Twin B configuration (O/F = 8).

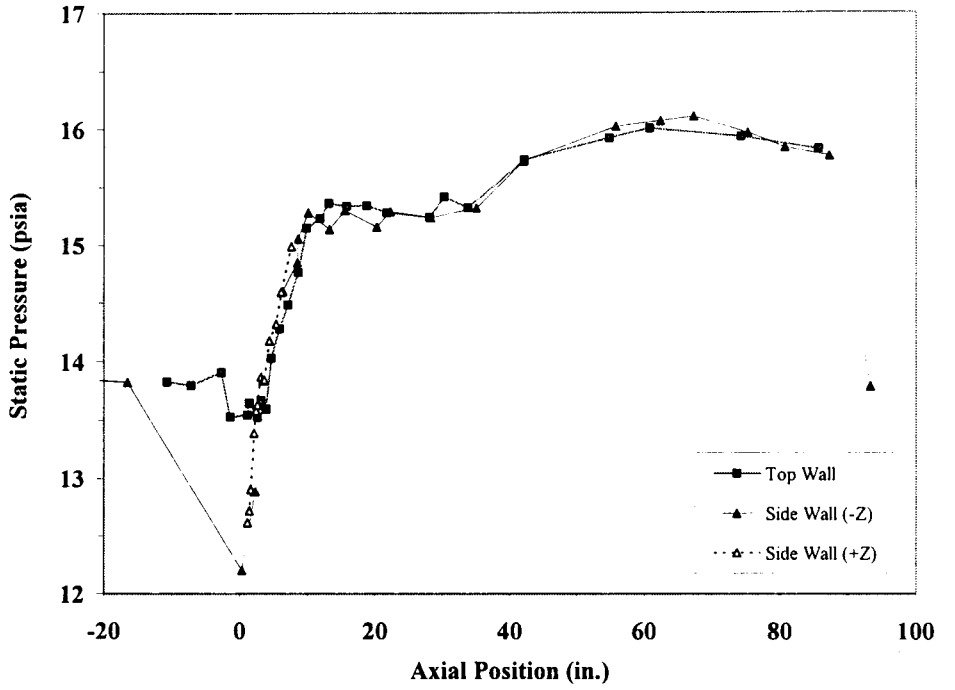

Fig. 5.4. Axial pressure profile for the Twin A configuration (O/F = 8).

the Twin B results shown in Fig. 5.3. A velocity difference between the center and top regions would also occur for the Twin A configuration.

Downstream of the steep rise in axial pressure in the mixer section, there are virtually no differences between the top and side wall pressure profiles for either Twin thruster configuration.

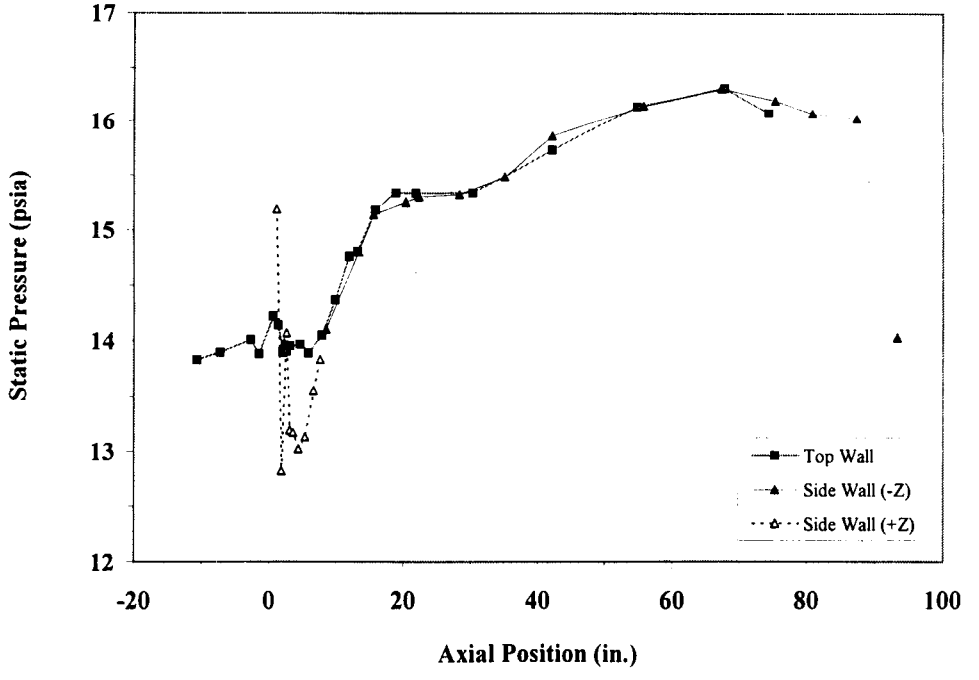

Fig. 5.5. Axial pressure profile for the Single configuration (O/F = 8).

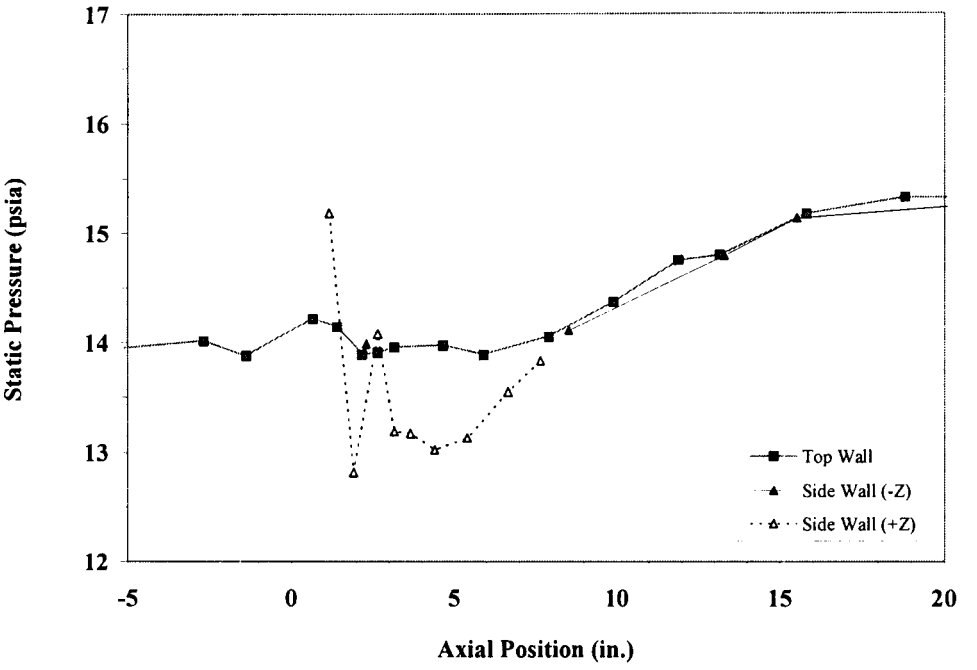

Fig. 5.6. Single thruster axial pressure profile near the thruster exit plane.

By this point, the primary and secondary flow streams have mixed thoroughly, and the flow is essentially one-dimensional. Finally, it should be noted that the pressure was not measured at the duct exit for the Twin B tests, which explains why the pressure profile in Fig. 5.3 does not drop sharply near the exit as it does in Fig. 5.4.

Immediately downstream of the thruster exit plane, the side wall pressure profile for the Single configuration (Fig. 5.5) shows high-amplitude variations in pressure with axial distance. These variations are more obvious in Fig. 5.6 which has an expanded scale. Since the side wall measurements were made along the centerline of the primary flow, the axial pressure variations probably indicate the presence of a shock structure typical of supersonic jet flow [15]. Downstream of these axial pressure variations, there is a static pressure difference of approximately 1 psid between the centerline and the top wall. As with the Twin thruster configurations, this difference vanishes after the steep pressure rise indicating the extent of the primary/secondary mixing.

The top wall pressure profiles in the mixer section for all three configurations are compared in Fig. 5.7. The Phase I results [3] showed that the point in the mixer section where the pressure plateau begins is a reasonable indication of the primary/secondary mixing length. The Twin B profile has the steepest gradient and reaches a plateau first, followed by the Twin A

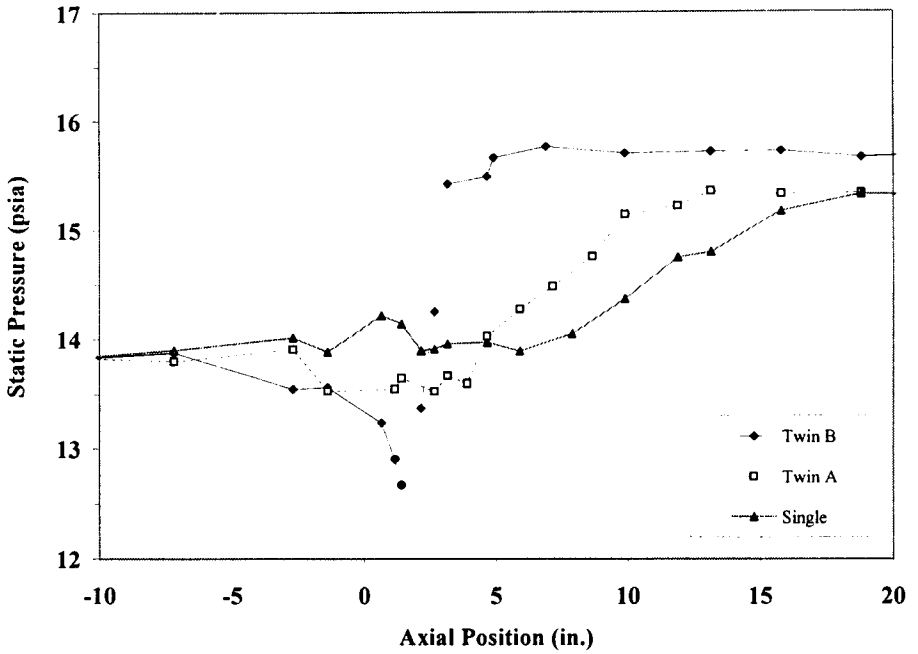

Fig. 5.7. Top wall static pressure comparison (O/F = 8).

configuration, and finally the Single configuration. The corresponding mixing lengths are approximately 5, 12 and 19 in., respectively. The fact that the Twin B plateau is higher than the other two is another indication that this configuration entrained the most air.

Figure 5.8 compares the side wall pressure profiles in the mixer section. Measurements from both side walls were used to generate this and other side wall pressure plots, so some

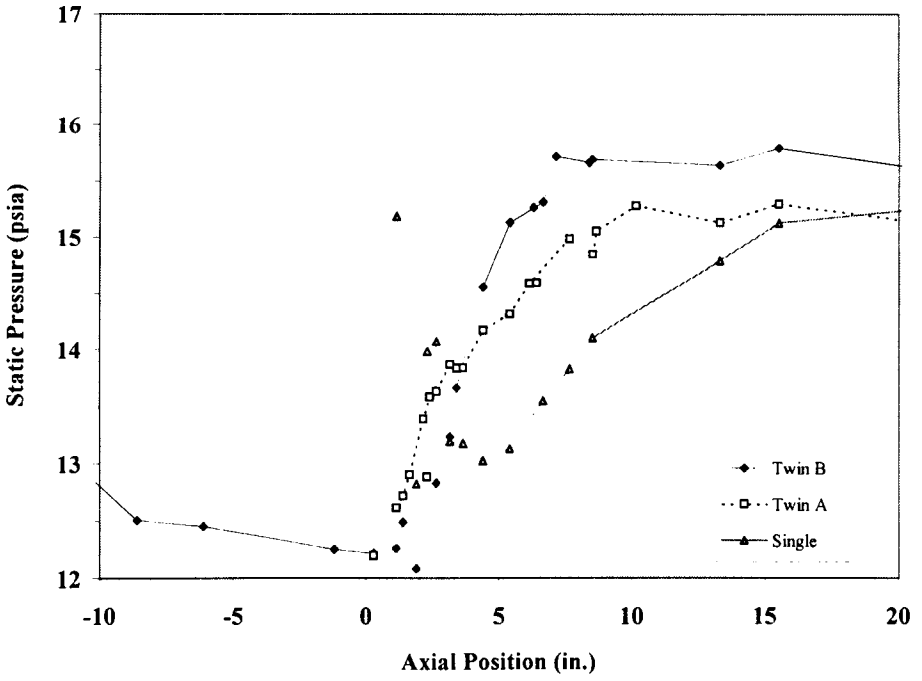

Fig. 5.8. Side wall static pressure comparison (O/F = 8).

discontinuities appear in the figure. In general, the same trends seen in the top wall profiles are also seen along the side wall. The Twin A and B pressure gradients are exceptions. The Twin A axial pressure on the side wall centerline begins to rise within one inch of the thruster exit plane compared to four inches on the top wall (see Fig. 5.7). This difference suggests that mixing begins earlier between the thrusters than it does near the top and bottom walls. In fact, the Twin A pressure rise on the side wall begins before the Twin B rise (x = 1 in. vs. 3 in.). Because the Twin B side wall pressure gradient is steeper, it overtakes the Twin A profile, resulting in a shorter mixing length for the Twin B configuration (7 vs. 10 in.). The Twin B pressure rise on the side wall is further downstream than the corresponding top wall rise. This difference between the Twin B side wall and top wall pressure rise is more apparent in Fig. 5.3. The fact that the Twin B mixing occurs sooner near the top wall than it does in the center region is consistent with the observed "wall biasing" of the primary jets discussed in the addendum report on Phase I results [3]. With the primary jets closer to the top and bottom walls, these regions will tend to mix out, while the air flow stream in the center region remains intact longer.

Figures 5.9 and 5.10 are the axial pressure profiles for the Twin B and Twin A configurations operating at O/F = 4, respectively. These pressure profiles have the same general characteristics as the profiles for O/F = 8 (Figs 5.3 and 5.4), except at the end of the steep

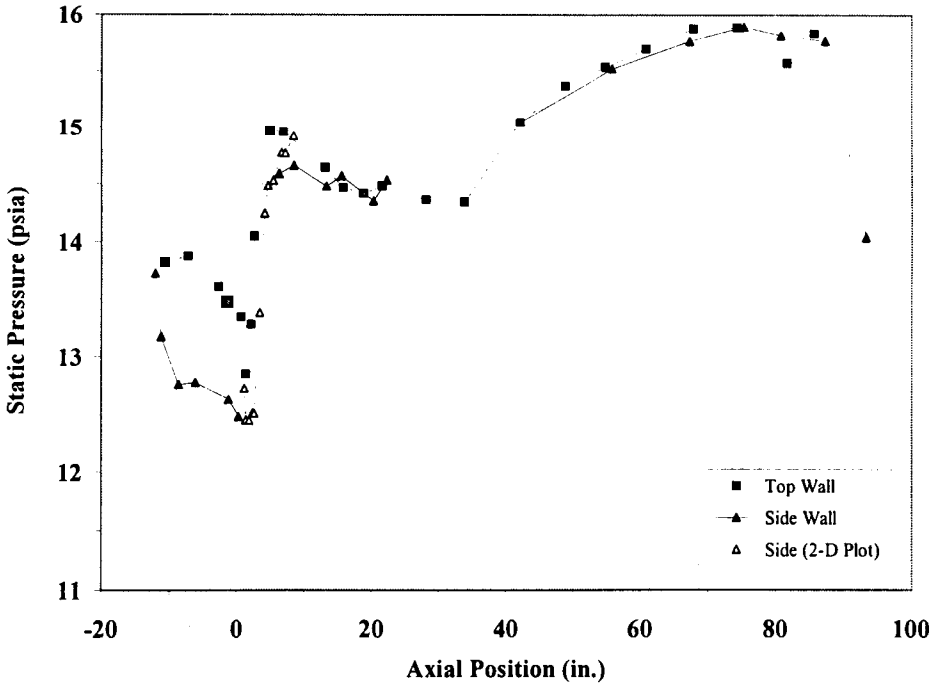

Fig. 5.9. Axial pressure profile for the Twin B configuration (O/F = 4).

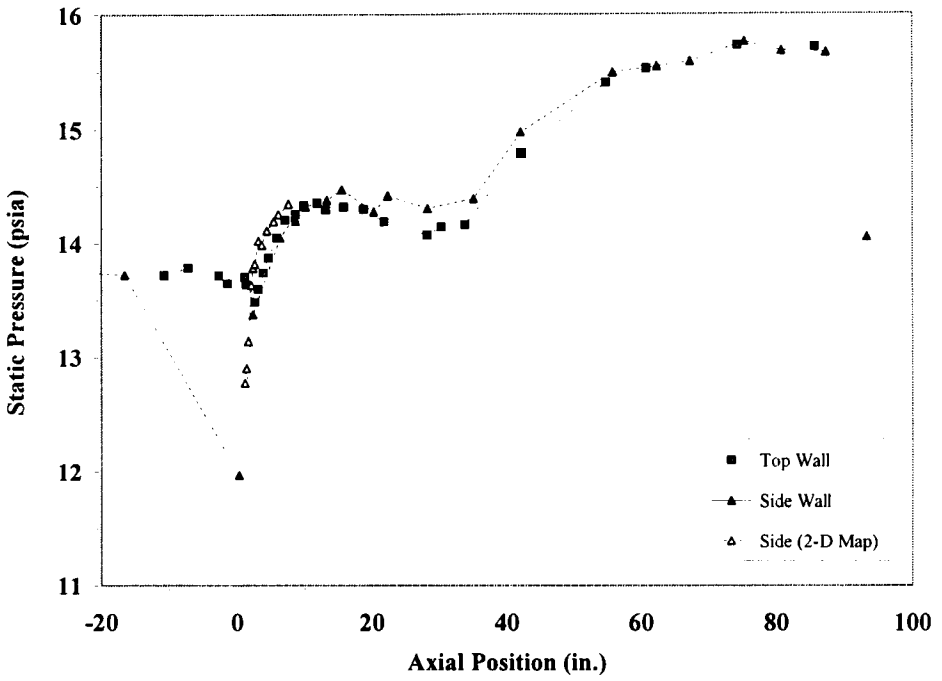

Fig. 5.10. Axial pressure profile for the Twin A configuration (O/F = 4).

pressure rise in the mixing section ($0 < x < 15$ in.). These differences are more apparent in Figs 5.11 and 5.12, which compare the Twin A and Twin B profiles along the top and side walls, respectively. In both Fig. 5.11 and 5.12, the Twin B pressure reaches a peak value within ~5-8 in. The pressure then decreases until $x \sim 15$ in., where it reaches a plateau. On the other

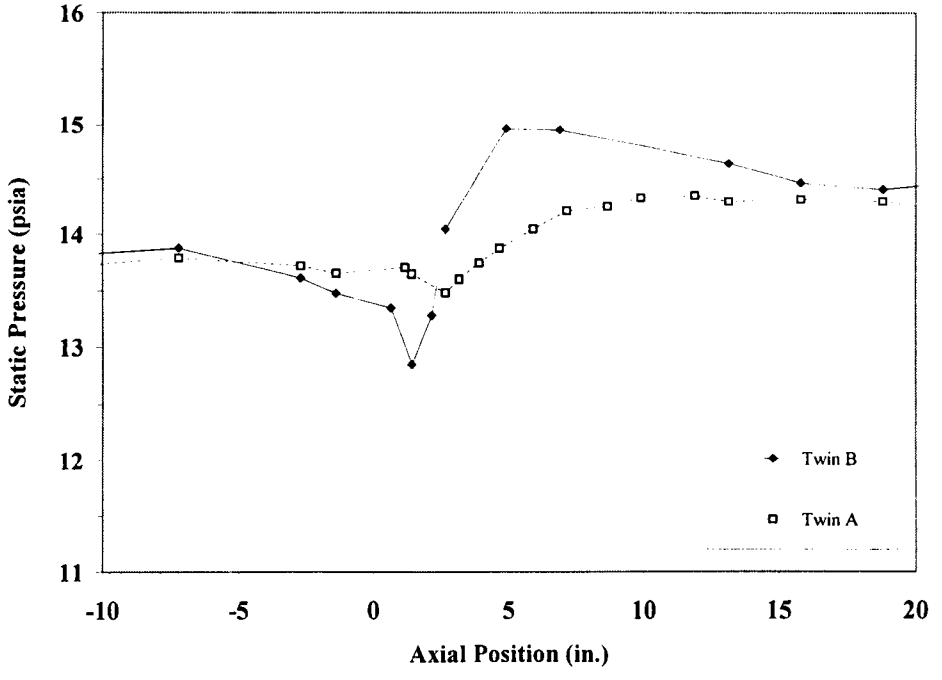

Fig. 5.11. Top wall static pressure comparison (O/F = 4).

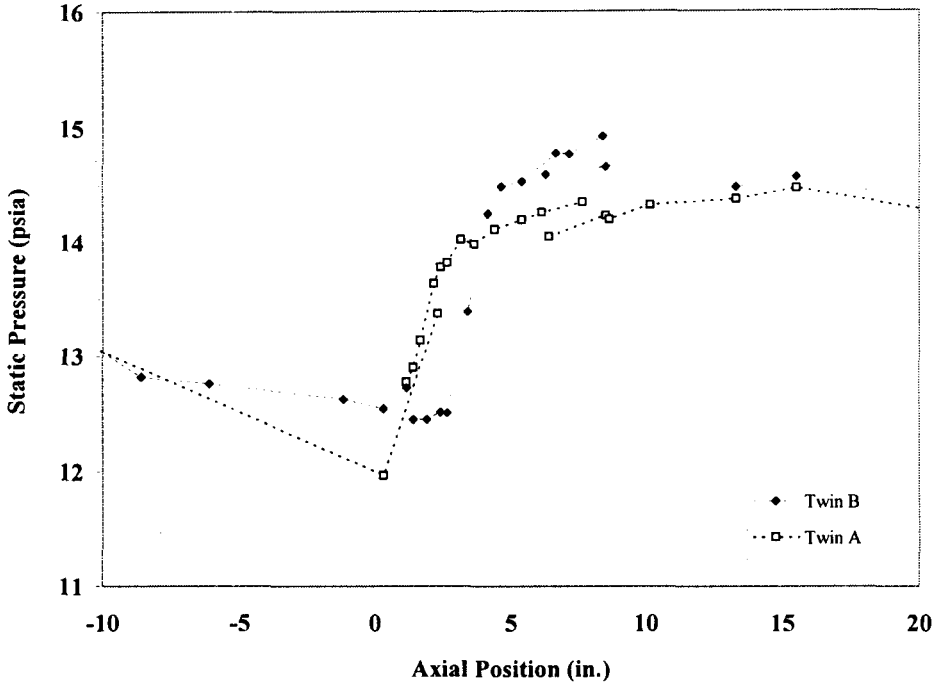

Fig. 5.12. Side wall static pressure comparison (O/F = 4).

hand, the Twin A profiles rise at a slower rate, and they asymptotically approach a plateau pressure at approximately the same point as the Twin B configuration.

With the Twin B configuration, the fuel-rich primary flow and the secondary flow mix rapidly at the macro-scale, but the micro-scale mixing required for complete combustion takes additional time. The pressure decrease beyond x ~ 5 in. indicates that heat release continues to occur in this region, lowering the density of the mixture and accelerating the flow. The beginning of the pressure plateau indicates the end of the heat release. The more rounded shape of the Twin A profiles indicates that the macro-scale mixing and the micro-scale mixing/combustion occur roughly at the same rate. The fact that both Twin configurations reach a pressure plateau at x ~ 15 in. indicates that the more rapid macro-scale mixing of the Twin B does not necessarily lead to a shorter overall mixing length when combustion is also occurring. The combined effects of turbulent mixing and combustion will determine the required length of the constant area combustor.

Downstream of the mixing region, the top and side wall profiles are nearly identical as shown in Figs. 5.9 and 5.10. The Twin B pressure profiles are higher than the Twin A profiles, again indicating that more air is entrained by the Twin B configuration.

5.2.2. Two-Dimensional Static Pressure Maps

The transverse pressure measurements on the +Z side wall were converted to two-dimensional contour maps in the x-y plane. These maps for Case 6 are presented as Figs 5.13 through 5.15 for the Twin B, Twin A, and Single configurations, respectively. Measurements were made simultaneously at the 11 transverse locations discussed in Section 3.3. These measurements do not extend all the way to the top and bottom walls ($y = \pm 2.5$ in.). Measurements were made at 9-13 axial locations between $x = 1.15$ in. and $x = 8.4$ in. The dark contour lines in the figures represent intervals of 0.5 psi, and the lighter lines are at intervals of 0.25 psi. The color coding is the same in all three figures. The numbers in the legend represent the upper limit of a 0.5 psi pressure interval. For example, the orange regions, labeled 15.5 in the legend, cover the range 15.0-15.5 psia. The location of the thruster centerlines are superimposed as horizontal dashed lines on the contour plots for reference.

The contour maps show that all three configurations have transverse pressure gradients ($\partial p/\partial y$) in the region where the primary/secondary mixing occurs. Gradients on the order of 1-4 psi/in. are present in all three figures. For the Twin configurations, the pressure field becomes essentially one-dimensional at $x \sim 6$-8 in. The single thruster pressure map does not extend far enough downstream to show the expected transition to a one-dimensional pressure field.

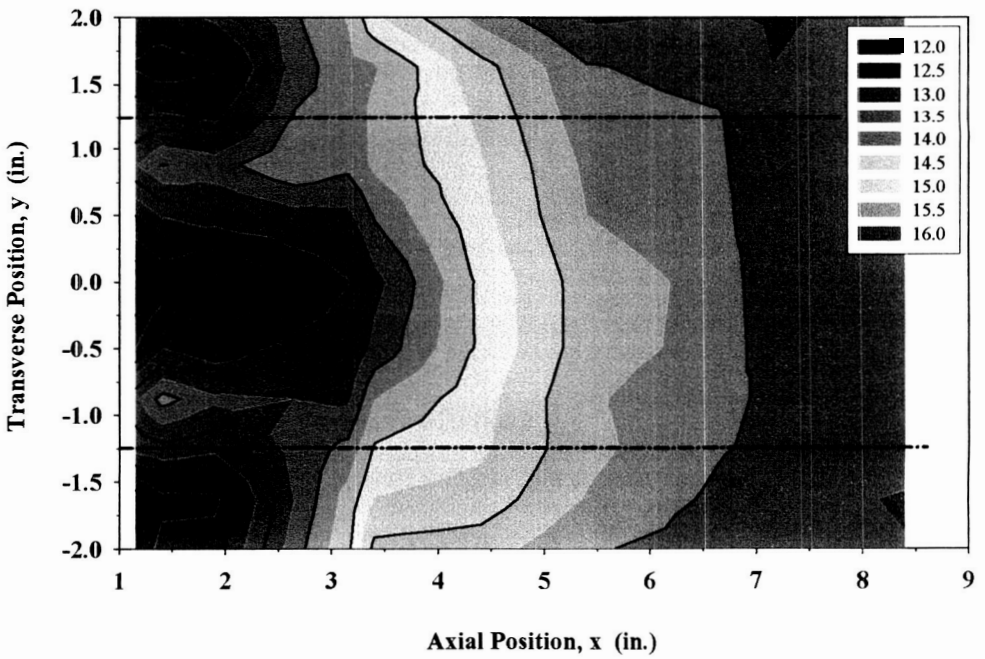

Fig. 5.13. Twin B configuration side wall static pressure map (psia) for O/F = 8.

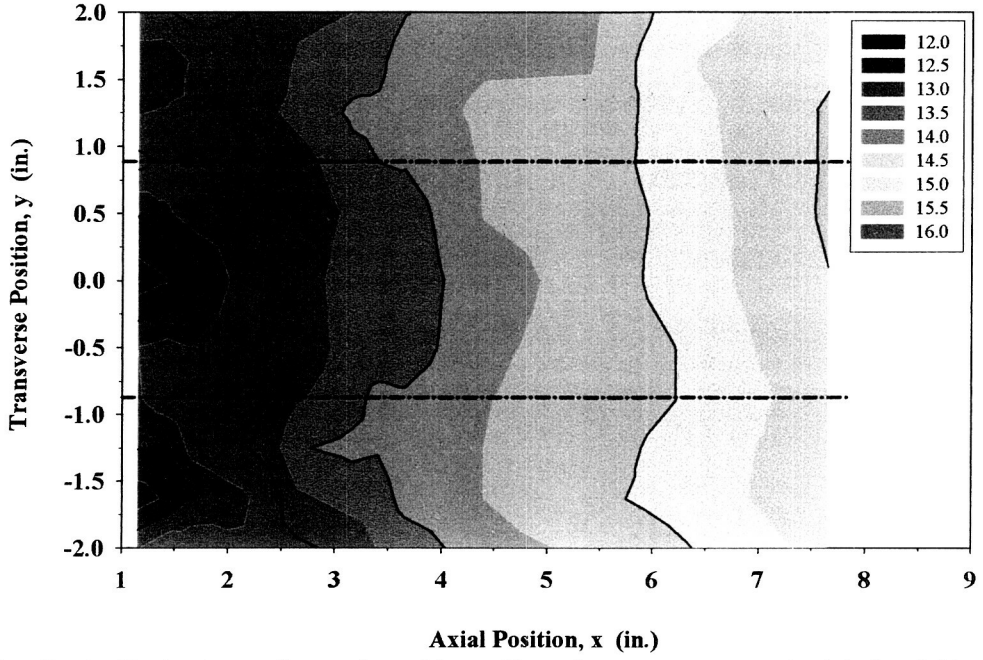

Fig. 5.14. Twin A configuration side wall static pressure map (psia) for O/F = 8.

The Twin B (Fig. 5.13) contours between x = 3 and 7 in. have a concave shape, suggesting that the static pressure is rising faster near the top/bottom walls than in the center. As the axial pressure profiles suggested, it appears that the primary/secondary mixing occurs sooner near the walls than it does in the central core. In the region $0 < x < 2.5$ in., the pressure inside the thruster centerlines is higher than the pressure outside the centerlines. This pressure difference, which is ~1.0-1.5 psid at x = 1.5 in., helps explain the biasing of the thruster jets toward the top and bottom walls observed in the Phase I investigation [3]. The origin of this pressure difference is not completely understood from the available data. One possibility is that these high pressure regions are recirculation zones for the low pressure/high velocity air flowing between the thrusters.

Unlike the Twin B pressure map, the Twin A contour lines in Fig. 5.14 have a very slight convex shape. The Twin A mixing in the center of the duct occurs at the same rate or slightly faster than mixing near the top/bottom walls. Except for a few irregularities, the Twin A pressure field is essentially one-dimensional at $x \sim 2$ in. The vertical contour lines are spaced further apart than the lines in Fig. 5.13, indicating that the mixing rate is slower for the Twin A than the Twin B. Unlike the Twin B pressure field, the pressures on either side of the thruster centerlines are approximately equal for the Twin A configuration.

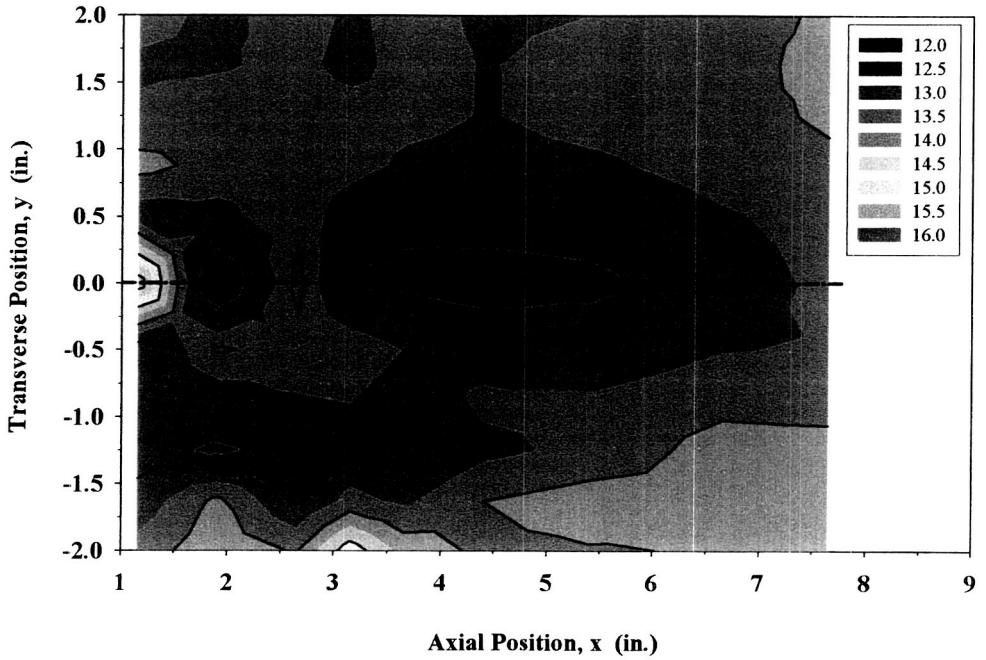

Fig. 5.15. Single configuration side wall static pressure map (psia) for O/F = 8.

Figure 5.15 provides a clearer view of the nature of the axial pressure variations observed along the side wall centerline in Figs. 5.5 and 5.6. For comparison, Fig. 5.16 is a photograph of a typical supersonic gas jet [16]. The pressure islands located on the centerline at $x < 3$ in. in Fig. 5.15 have the same basic structure as the shock diamonds seen in the supersonic jet photograph. In addition, the low-pressure region located downstream of these islands ($3 < x < 6$ in.) correlates well with the turbulent jet break-up region seen on the right-hand side of Fig. 5.16.

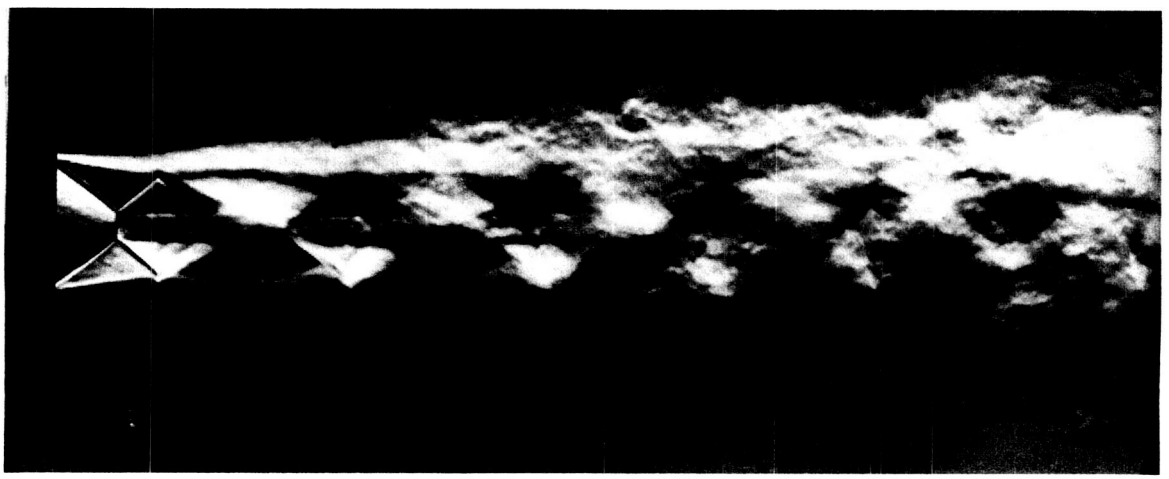

Fig. 5.16. Shock cell structure in a supersonic jet (from Van Dyke [16]).

All three contour maps show a degree of asymmetry near the thruster exit plane. Another view of this trend is shown in Fig. 5.17, where the transverse profiles for all three configurations at x = 1.15 in. are plotted. The pressures near the bottom wall are 0.1-0.4 psi lower than the corresponding values near the top wall. This asymmetry is also seen in the air velocity and flow rate measurements, and is discussed further in Section 5.3. The asymmetry vanishes by x ~ 2 in. for the Twin configurations (Figs 5.13 and 5.14), but it is still present at the end of the Single thruster pressure map (x = 7.65 in., Fig. 5.15).

Figure 5.18 compares the experimental and CFD results [12, 13] of transverse pressure profiles for the Twin B configuration at O/F = 8. The dashed vertical lines represent the ambient pressure for the experiment (14.1 psia) and the model (14.7 psia), and the horizontal lines represent the thruster centerlines. Several differences between the two pressure profiles are apparent. Whereas the CFD static pressures are ~0.2-0.3 psi below ambient, the measured values are ~1 psi below ambient on average. Only minor variations (~ 0.1 psi) are seen in the CFD static pressure, most notably near the thruster centerlines. On the other hand, there is a difference of nearly 2 psi between the minimum and maximum measured values. The model does not predict these large transverse pressure gradients, nor does it identify the local maxima and minima seen in the measurements.

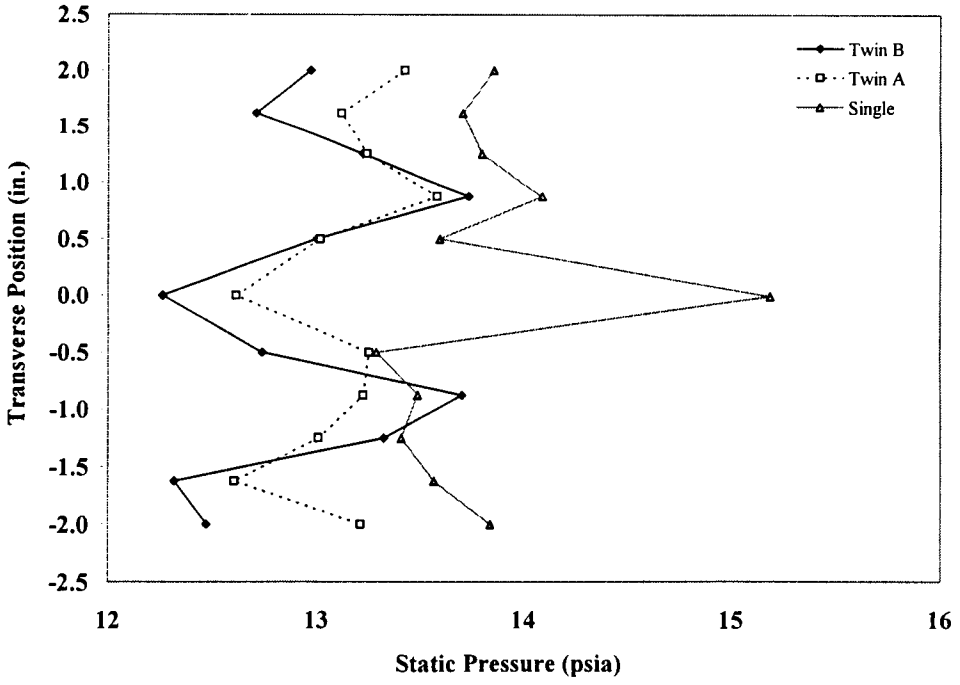

Fig. 5.17. Transverse pressure profiles at x = 1.15 in. (O/F = 8).

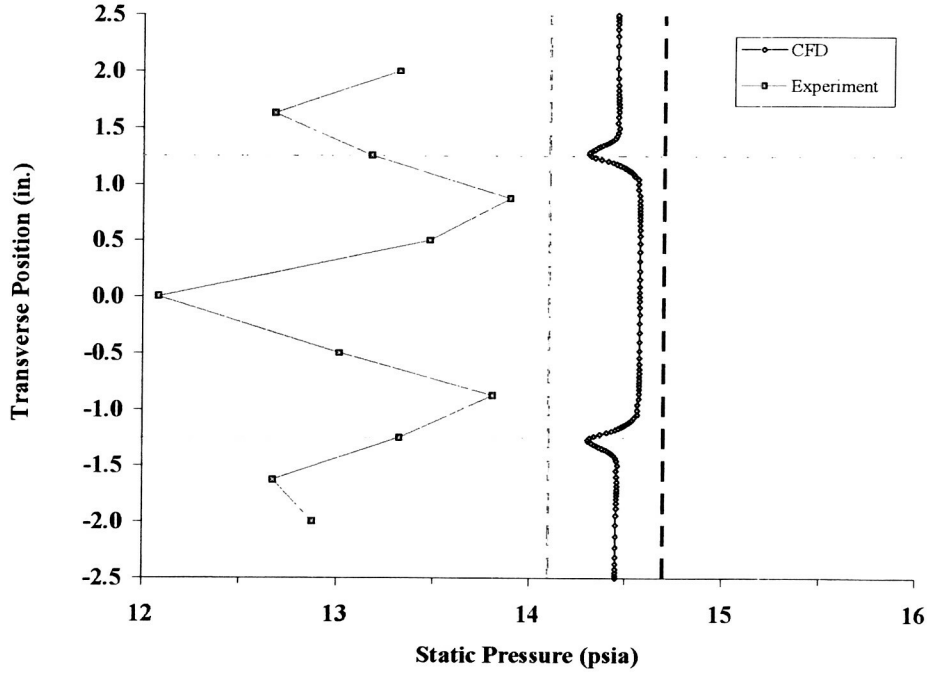

Fig. 5.18. Transverse pressure profiles for Twin B configuration for O/F = 8 at x = 1.90 in., CFD versus experimental data.

Figure 5.19 is the pressure contour map for the Twin B configuration operating at O/F = 4. In general, it looks very similar to the corresponding pressure map at O/F = 8 (Fig. 5.13). The high pressure regions on the inside edges of the primary flow streams ($y \approx \pm 0.8$ in.) are even more prominent in Fig. 5.19 than in Fig. 5.13. The pressure difference

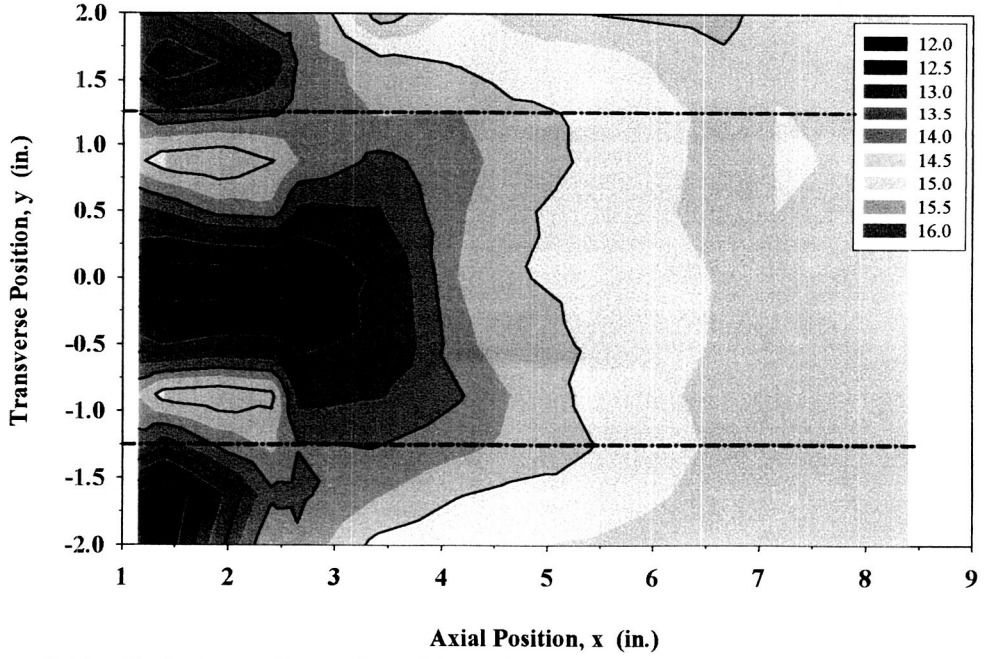

Fig. 5.19. Twin B configuration side wall static pressure map (psia) for O/F = 4.

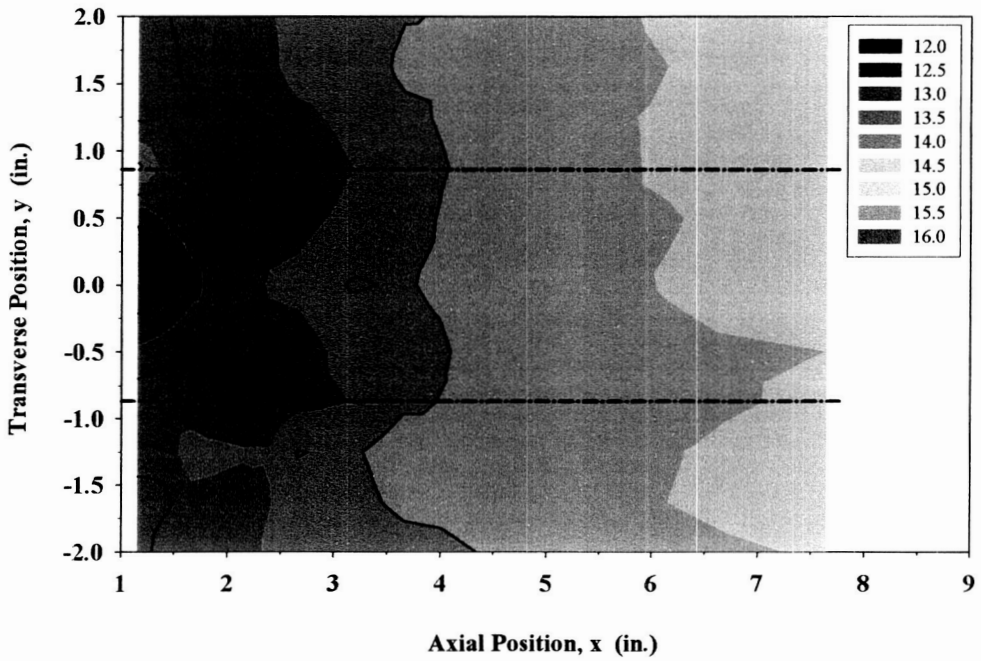

Fig. 5.20. Twin A configuration side wall static pressure map (psia) for O/F = 4.

between the inside and outside edges of the primary jets is ~1.5-2.0 psid for O/F = 4. The central low pressure region bulges out toward the top and bottom walls at x = 3 – 4 in. This pattern supports the idea that the high pressure regions are recirculation zones for the air flowing between the thrusters.

Figure 5.20 is the static pressure map for the Twin A operating at O/F = 4. Its characteristics are very similar to Fig. 5.14 (Twin A at O/F = 8). A comparison of the contours in Figs. 5.19 and 5.20 shows that the Twin B mixes the flow and raises the pressure much more rapidly than the Twin A. Some top-to-bottom asymmetry is seen in Figs. 5.19 and 5.20. The transverse pressure profiles (x = 1.15 in.) in Fig. 5.21 show this asymmetry to be more pronounced for the Twin B configuration. The effect of the asymmetry will be discussed further in the discussion of the air flow measurements (Section 5.3.2).

5.3. Air Velocity and Mass Flow Rate Measurements

5.3.1. Inlet Region

The velocity of the secondary flow stream was measured in order to calculate the entrained air mass flow rate. A 0.125-in. diameter pitot-static probe was installed upstream of the thruster nose fairings with the sensing tip located at x = -13.65 in. As shown in Fig. 5.22, the probe could be moved to different transverse positions between tests to produce a velocity profile

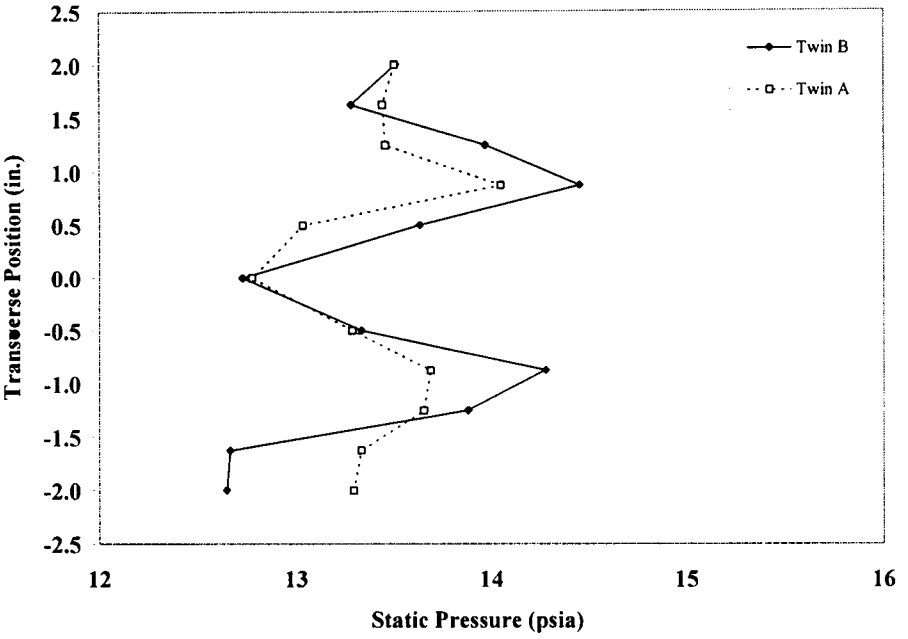

Fig. 5.21. Transverse pressure profiles at x = 1.15 in. for O/F = 4.

in the vertical (y) direction. In all cases the probe was located at the midpoint of the duct width (z= 0.0 in.). The difference between the stagnation (P_o) and static (p) pressure outputs of the pitot-static probe was measured with a differential pressure gage. Assuming the stagnation pressure and temperature (T_o) were the ambient values in the lab, the local velocity of the air stream was calculated using the isentropic compressible flow relationships [17]:

$$V = M \cdot a \qquad [5.3]$$

$$M = \sqrt{\left[\left(\frac{P_o}{p}\right)^{\gamma-1/\gamma} - 1\right] \cdot \left(\frac{2}{\gamma - 1}\right)} \qquad [5.4]$$

$$a = \sqrt{\gamma \frac{R_u}{MW} T} \qquad [5.5]$$

$$T = T_o \Big/ \left(1 + \frac{\gamma - 1}{2} M^2\right) \qquad [5.6]$$

where,

$M \equiv$ Mach number

$a \equiv$ speed of sound

$\gamma \equiv$ ratio of specific heats (C_p/C_v)

$R_u \equiv$ universal gas constant

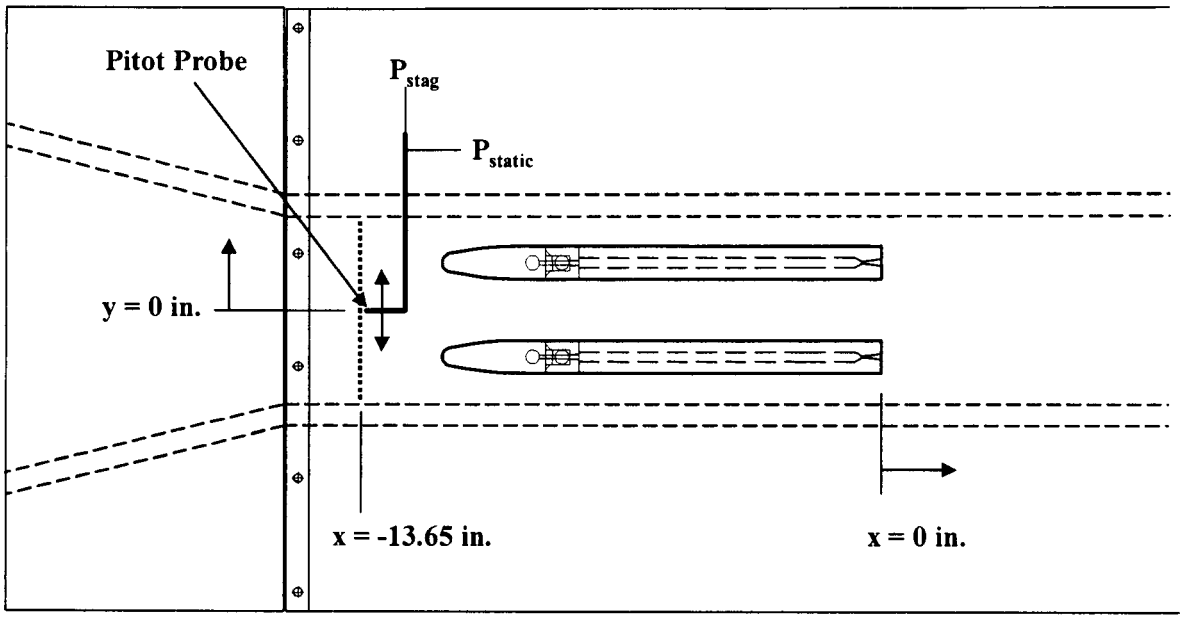

Fig. 5.22. Pitot-static probe measurement locations.

$MW \equiv$ molecular weight of the gas

$T \equiv$ static temperature

An error analysis was performed for the velocity calculations based on Equations 5.3 through 5.6. The potential sources of error include the pressure difference measurement (Δp) and the uncertainty in determining the stagnation pressure and temperature. The accuracy of the Δp measurement depends on the pitot-static probe, which is accurate to $\pm$ 0.5% up to Mach numbers of 0.5, and the differential pressure gage which is accurate to $\pm$ 0.25% of the values measured in the experiments. The ambient pressure usually changed during a test day, and a representative range of variation is $\pm$ 0.05 psi. Uncertainty in ambient temperature was estimated to be $\pm$ 5°R, or approximately $\pm$ 1%. Using standard error analysis techniques [18], the error in the speed of sound (Equation 5.5) was estimated to be $\pm$ 0.50%, and the error in Mach number (Equation 5.4) was $\pm$ 0.25%. The combination of these two terms resulted in an error estimate of $\pm$ 0.56% for the velocity calculation (Equation 5.3).

Figures 5.23 through 5.25 show the measured air velocity profiles for the O/F = 8 experiments with the Twin A, Twin B and Single configurations, respectively. The scale and position of the thrusters in the transverse direction are depicted in the figures for reference. Measurements were made on the centerline (y = 0.0 in.) and in 0.5-in. increments above and below the centerline. In some cases, additional measurements were made at intermediate

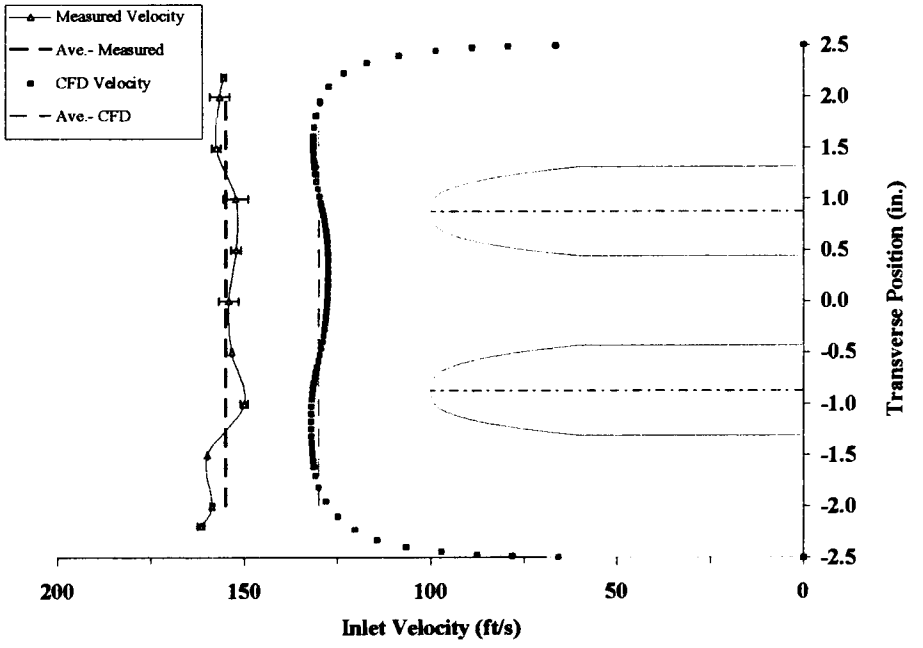

Fig. 5.23. Inlet velocity profile for the Twin A configuration at O/F = 8 (x = -13.65 in.).

locations. The data points are the average velocity from several tests, typically 3-5, at each transverse position. The error bars on the data points represent ± one standard deviation, which is probably more representative of the uncertainty in the data than the measurement error (± 0.56%).

Measurements were made near the bottom wall for the Twin B configuration (Fig. 5.24) in order to characterize the velocity profile in the boundary layer. In general though, pitot probe

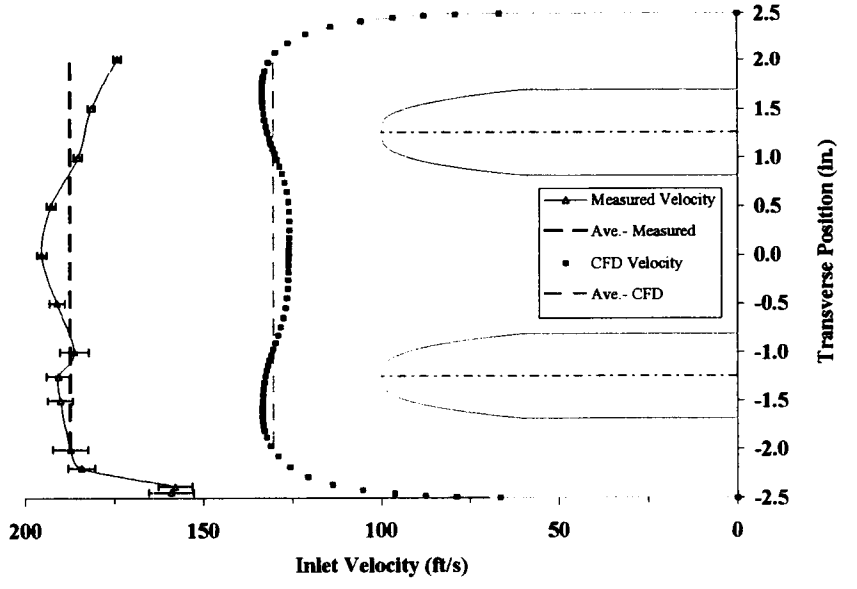

Fig. 5.24. Inlet velocity profile for the Twin B configuration at O/F = 8 (x = -13.65 in.).

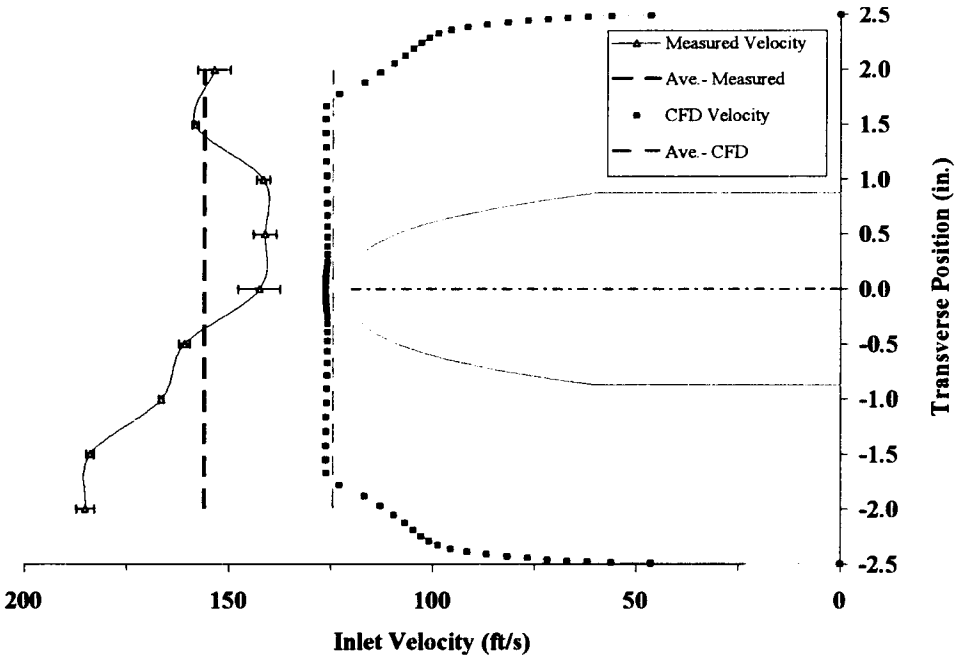

Fig. 5.25. Inlet velocity profile for the Single configuration at O/F = 8 (x = -13.65 in.).

measurements were not made further out from the centerline than y = ± 2.0 in. As the probe approaches a parallel wall, the region between the probe and the wall begins to act as a venturi. The resulting static pressure decrease in this region affects the accuracy of the pitot probe reading. These effects are significant at distances of less than $5d_p$ from a wall, where d_p is the probe diameter. The error in the inlet measurements at y = ± 2.0 in. ($4d_p$) is ~1.2%, which is still reasonable. At a distance of $2d_p$ from a wall, the measurement error increases to 2%.

The velocity profiles from the NASA/Marshall CFD analysis [12, 13] at approximately the same axial position (x = -13.5 in.) are also shown in Figs. 5.23-5.25. The CFD velocity profiles are at the center of the duct width (z= 0.0 in.) and they extend from the bottom wall to the top wall (-2.5 ≤ y ≤ 2.5 in.). The x-component of velocity is plotted, which is typically greater than 99.99% of the total velocity magnitude. There are a total of 81 grid points in the y direction, with a variable grid spacing of ~0.05 in.

The dashed vertical lines in Figs. 5.23-5.25 represent the average velocity from y = -2.0 in. to y = 2.0 in. for both the experimental and CFD profiles. In general, the velocity data points do not deviate significantly from the average value. The CFD velocities are within ± 3.5% of the average, the Twin A measurements are within ± 3.2% of the average, and the Twin B measurements are within +4 / -7 % of the average. However, the Single configuration

Table 5.5. Summary of inlet velocity and mass flow rate data at O/F = 8.

		Single Thruster			Twin A (Ψ= 1.75 in.)			Twin B (Ψ= 2.50 in.)		
		CFD	xperiment		CFD	xperiment		CFD	xperiment	
Parameter	Units	Value	Value	% Δ	Value	Value	% Δ	Value	Value	% Δ
Average Velocity	(ft/s)	124.4	156.1	25.5	129.9	155.0	19.3	130.2	187.1	43.7
Geometric Area	(in^2)	15.0			15.0			15.0		
Area Correction Factor	--	0.890			0.870			0.874		
Effective Area	(in^2)	13.4			13.1			13.1		
Density	(lb_m/ft^3)	0.0726	0.0729	0.4	0.0725	0.0740	2.1	0.0725	0.0748	3.2
Air Flow Rate (Nom.)	(lb_m/s)	0.837	1.055	26.0	0.853	1.039	21.8	0.859	1.274	48.3
Air Flow (Min)	(lb_m/s)		1.029			1.028			1.238	
Air Flow (Max)	(lb_m/s)		1.083			1.052			1.311	
Min / Max Range	(%)		-2.5 / +2.6			-1.1 / +1.2			-2.8 / +2.9	
Overall Phi	--	0.756	0.600	-20.6	0.742	0.609	-17.9	0.736	0.497	-32.5
Mass Flux	(lb_m/in^2-s)	0.0558	0.0703	26.0	0.0569	0.0693	21.8	0.0573	0.0849	48.3

NOTE : Shaded boxes indicate no information is available

measured velocities deviate from the average by +19 / -10 %. In addition, this measured velocity profile is asymmetric. The average velocity above the centerline is ~17% lower than the average below the centerline. Despite these irregularities, the average velocity was used as the representative value for the Single configuration in order to keep the analyses consistent throughout.

These average velocities are a convenient basis for comparing results, and Table 5.5 summarizes the values for all three configurations at O/F = 8. The average CFD velocities are approximately the same for all three configurations, although the single thruster velocity is ~4% lower than the Twin thruster values. In all cases, the average measured velocity is larger than the average CFD value. These velocity differences, which range from 19% to 44%, confirm a similar trend observed in the Phase I test series [3].

These velocity results suggest two potential areas of improvement in the CFD model. The fact that the model consistently under-predicts the air flow rate suggests that the physics of the entrainment/mixing process has not been modeled adequately. Recent research that has focused on anisotropic turbulence models for compressible flow fields may help resolve the current problem [19]. The second potential area for improvement is in modeling the phenomena that cause the differences between Twin B and the other two configurations. One of the

motivations for continuing to study this problem experimentally was to gain additional insight into the physical phenomena that cause these differences.

In addition to the average velocity comparisons, Table 5.5 summarizes the entrained air mass flow rate calculations. The CFD values for mass flow rate were obtained by summing the mass flow at each point in the grid cross-section at one axial location:

$$\dot{m}_{CFD} = \sum_{j=1}^{n_j} \sum_{k=1}^{n_k} \rho_{j,k} \cdot A_{j,k} \cdot U_{j,k} \qquad [5.7]$$

where n_j and n_k represent the number of grid points in the y and z directions, respectively.

In order to accurately calculate the experimental air mass flow rate, the effect of the boundary layers in the inlet had to be taken into account. A simple one-dimensional calculation was used:

$$\dot{m}_{Exp} = \rho_{ave} \cdot A_{Eff} \cdot U_{ave} \qquad [5.8]$$

where A_{Eff} is an effective cross-sectional area that accounts for the boundary layer effects. This effective area was derived from the available CFD data. At these relatively low Mach numbers ($M < 0.2$), the density varies less than ±0.2% across the CFD grid cross section. Therefore, an average density was defined simply as the average value of all the grid points at x = -13.5 in. The effective area was calculated using this average density, the average CFD velocity in Table 5.5, and the air flow rate calculated using Equation 5.7:

$$A_{Eff} = \frac{\dot{m}_{CFD}}{\rho_{ave,CFD} \cdot U_{ave,CFD}} \qquad [5.9]$$

Figure 5.24 shows that the measured velocity profile in the boundary layer follows the general shape of the CFD profile. Based on this similarity, it was assumed that the effective area derived from the CFD data was valid for the experimental data as well. The experimental air mass flow rate was calculated for each configuration using A_{Eff} from Equation 5.9, the average measured velocity in Table 5.5, and an average density. The average static density was calculated using a stagnation density (ρ_o) based on the ambient pressure and temperature in the lab, and the Mach number corresponding to the average velocity [17]:

$$\rho = \rho_o \Big/ \left(1 + \frac{\gamma - 1}{2} M^2\right)^{1/\gamma - 1} \qquad [5.10]$$

Since the pitot probe measurements for one configuration were taken over several days, a range of ambient pressures and temperatures were encountered during the testing. Over the course of the entire test program, the range of ambient pressures, corrected to the local altitude of 1200 ft., was 13.9-14.3 psia, and the temperature range was 490-550°R. Typically these ranges were smaller for the set of tests required to produce one profile. The overall minimum and maximum ambient pressure and temperature were identified for the test days associated with each velocity profile. The nominal air density and mass flow rate were calculated using values of ambient pressure and temperature midway between the recorded extremes. The effect of daily variation in ambient pressure and temperature on the mass flow rate for each configuration was estimated by calculating artificial minimum and maximum densities. The minimum density was based on the minimum recorded ambient pressure and the maximum ambient temperature during the set of tests for that configuration, even if these values did not occur on the same test day. The maximum density used the values at the opposite extremes of pressure and temperature. The resulting minimum and maximum mass flow rates are included in Table 5.5. The variation in ambient conditions results in potential flow rate variations of less than ± 3%. Therefore, the nominal values of air flow rate provide a reasonable basis for comparing results.

Finally, Table 5.5 summarizes the overall equivalence ratio (Φ_{total}) and mass flux ($\dot{m}''$) for each case. The propellant flow rates listed in Table 2.9 were used to calculate Φ_{total}. The nominal air flow rates in Table 5.5 were used to calculate the experimental values of Φ_{total} and $\dot{m}''$. In all cases, the geometric areas, not the effective areas, were used to calculate $\dot{m}''$.

The experimental mass flow rates correlate well with the Phase I results [3], where a static pressure measurement on the inlet side wall was used to calculate the velocity and flow rate of the air. The single thruster flow rate at O/F = 8 is nearly identical to the Phase I value, and the Twin B flow rate is ~5% higher than the Phase I value. These results confirm the differences between predicted (CFD) and measured air mass flow rates identified in Phase I. The Phase II measurements also confirm that the technique used in Phase I to calculate the air flow rate is reasonable.

The Twin B configuration entrains approximately 20% more air than the other two configurations. As with the thrust measurements, this trend indicates that the Twin B flow field is fundamentally different from the other two. However, these measurements do not explain why

Table 5.6. Summary of inlet velocity and mass flow rate data at O/F = 4.

Parameter	Units	Single Thruster Experiment Value	Twin A (Ψ= 1.75 in.) Experiment Value	Twin B (Ψ= 2.50 in.) Experiment Value
Average Velocity	**(ft/s)**		**151.6**	**180.8**
Geometric Area	**(in^2)**		15.0	15.0
Area Correction Factor	**--**		0.870	0.874
Effective Area	**(in^2)**		13.1	13.1
Density	**(lb_m/ft^3)**		**0.0752**	**0.0732**
Air Flow Rate	**(lb_m/s)**		**1.033**	**1.205**
Air Flow (Min)	**(lb_m/s)**		1.018	1.158
Air Flow (Max)	**(lb_m/s)**		1.048	1.256
Min / Max Range	**(%)**		-1.4 / +1.4	-3.9 / +4.1
Overall Phi	**--**		**0.781**	**0.670**
Mass Flux	**(lb_m/in^2-s)**		0.0688	0.0803

NOTE : Shaded boxes indicate no information is available

the Twin B configuration is different. Additional tests were performed to study these differences, and the results of the tests will be discussed in Section 5.4.

Table 5.6 contains a similar set of velocity and flow rate results for the Twin A and Twin B experiments at O/F = 4. Pitot probe measurements were not made for the Single configuration at O/F = 4, and no CFD analyses were performed at O/F = 4. The area correction factors in Table 5.6 were assumed to be the same as the corresponding values in Table 5.5.

The Case 5 values of average velocity and nominal mass flow rate are within 5% of the Case 6 values. The same ~20% difference in entrained air flow rate between Twin A and Twin B configurations is present at O/F = 4. The mechanism driving the higher entrainment for the Twin B configuration does not appear to be affected by the heat release in the constant-area combustor for Case 5.

5.3.2. Thruster Body Region

The thruster body regions for all three configurations are shown in Fig. 5.26. This region consists of the secondary flow areas between the thruster bodies and the top and bottom duct walls, $A_{2,upper}$ and $A_{2,lower}$, respectively. Note that for the Twin thruster configurations, there is

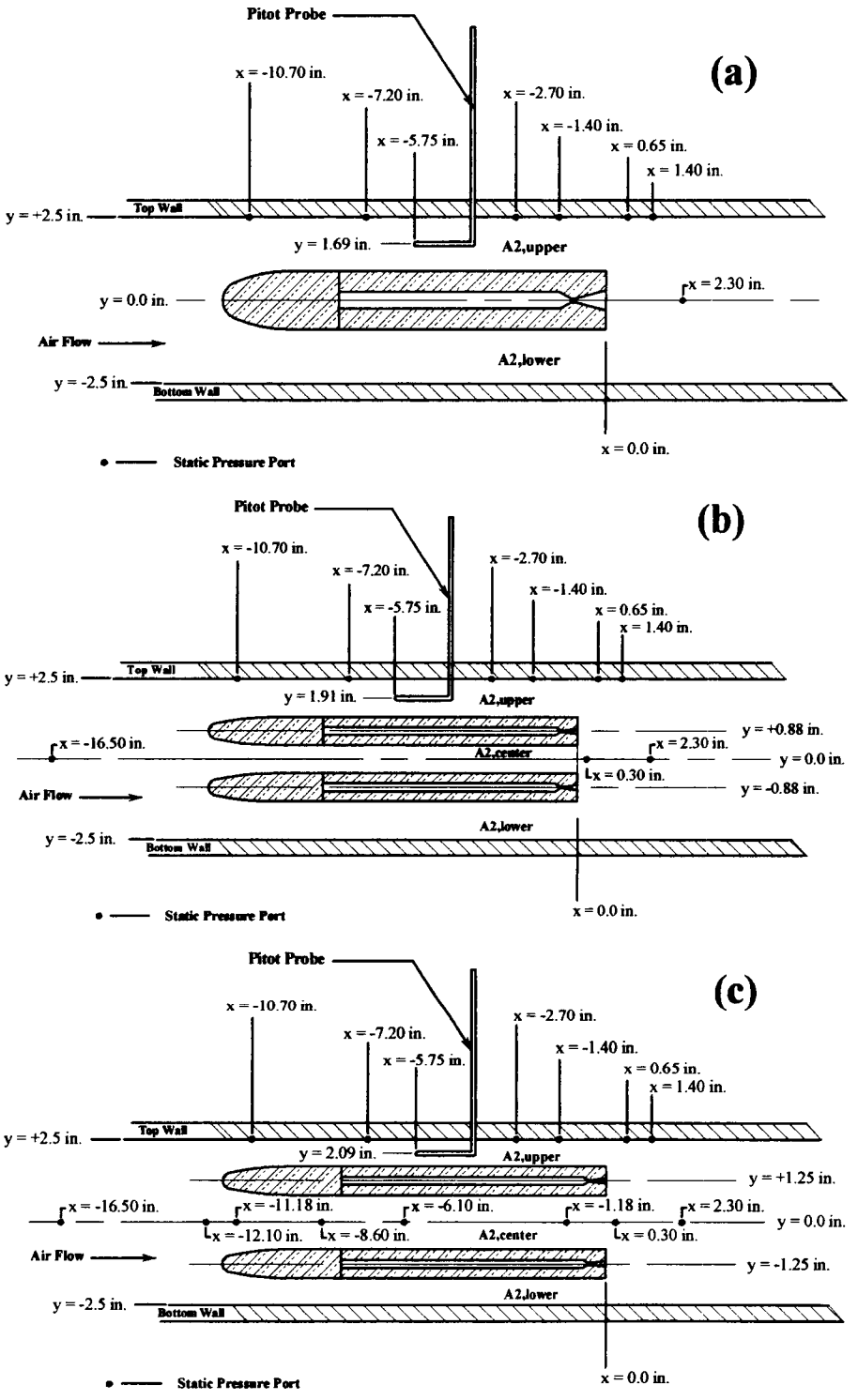

Fig. 5.26. Thruster body regions for the three configurations showing instrumentation locations. (a) Single configuration, (b) Twin A configuration, and (c) Twin B configuration.

another area between the thrusters ($A_{2,center}$). Clearly, for the Single configuration there is no $A_{2,center}$. The air flow rates in these regions were analyzed in order to develop a better understanding of the effect of thruster geometry on the air entrainment process.

Velocities in the thruster body region were measured in two ways. The first approach used the pitot-static probe installed in the $A_{2,upper}$ section at x = -5.75 in., as shown in Fig. 5.26. The transverse (y) position of the probe was midway between the upper surface of the top thruster and the top wall. Equations 5.3 through 5.6 were again used to calculate the velocity based on the measured Δp. The second approach for measuring the air velocity used static pressure measurements along the top wall for $A_{2,upper}$ or on the sidewall centerline for $A_{2,center}$. Assuming the values at the wall were representative of the values in the center of the corresponding region, these static pressures were used in Equation 5.4 to calculate the air velocity. Figure 5.26 also shows the location of the static pressure measurement ports in the thruster body region for each of the configurations. In order to make a direct comparison with the pitot probe velocities, the static pressure measurements were interpolated in the axial direction (x) to obtain values at x = -5.75 in. Because of physical constraints the static pressure could not be measured in the $A_{2,center}$ region for the Twin A configuration. In this case, the only representative static pressure measurement along the sidewall centerline was at x = 0.30 in. Static pressure measurements were not made in the $A_{2,lower}$ region for any of the configurations, again because of physical constraints.

Figures 5.27 through 5.29 depict the velocity results for the three thruster configurations at O/F = 8. In each figure, the areas occupied by the thruster bodies are shaded for reference. Also included in the figures are the CFD transverse velocity profiles at approximately the same axial location. The velocities derived from the pitot probe measurements and from the wall static pressure in each of the $A_{2,upper}$ regions differ by ~1%. This small difference indicates that the static pressure approach is valid for estimating the centerline velocity in each region, as long as the assumption that the stagnation pressure and temperature are the ambient values is still valid. However, some of the results that will be discussed later in this section suggest that this assumption may not be valid.

For the Twin A configuration (Fig. 5.27), the measured velocity in the $A_{2,upper}$ region is 16% higher than the CFD value. This difference is consistent with the difference between the CFD and measured velocities in the inlet (19%). The measured velocity in the center region is

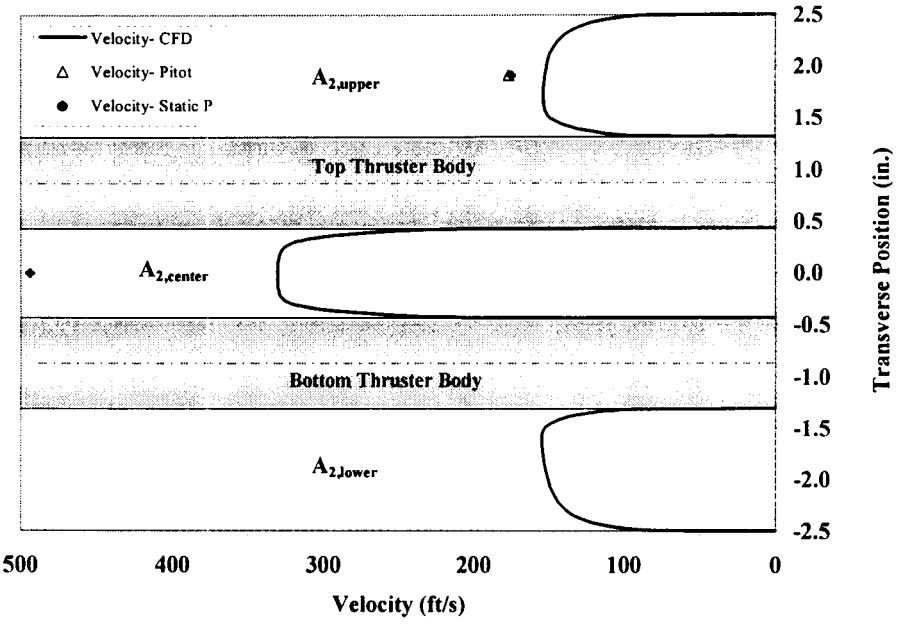

Fig. 5.27. Thruster body region velocity profiles for the Twin A configuration, O/F = 8 (x = -5.75 in.).

49% higher than the CFD prediction. One possibility for this large difference may be that the actual velocity profile in $A_{2,center}$ is not as flat as the CFD profile. For a given flow rate, thicker boundary layers would tend to increase the centerline velocity. A similar trend is seen in the Twin B velocity measurements (Fig. 5.28). In this case, the measured velocity is within 4% of

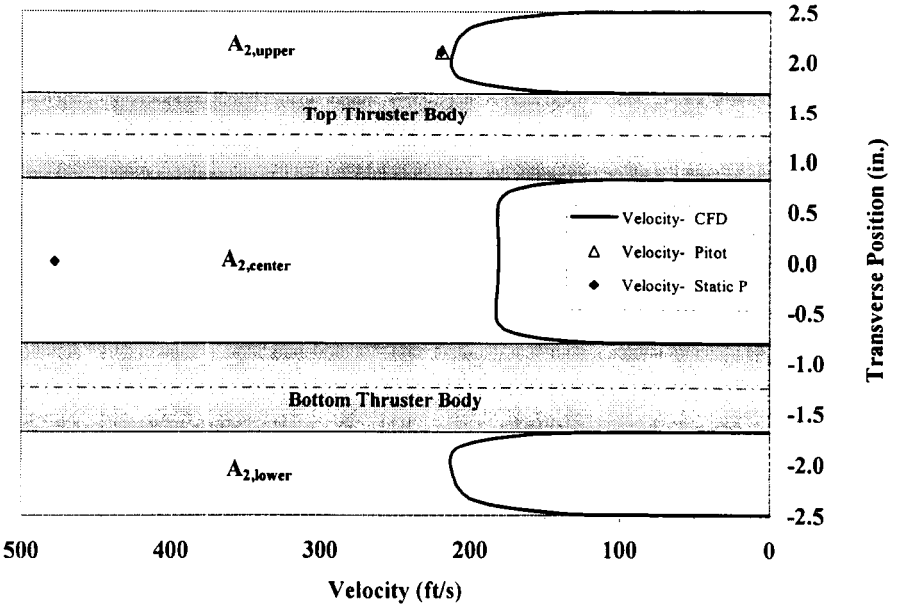

Fig. 5.28. Thruster body region velocity profiles for the Twin B configuration, O/F = 8 (x = -5.75 in.).

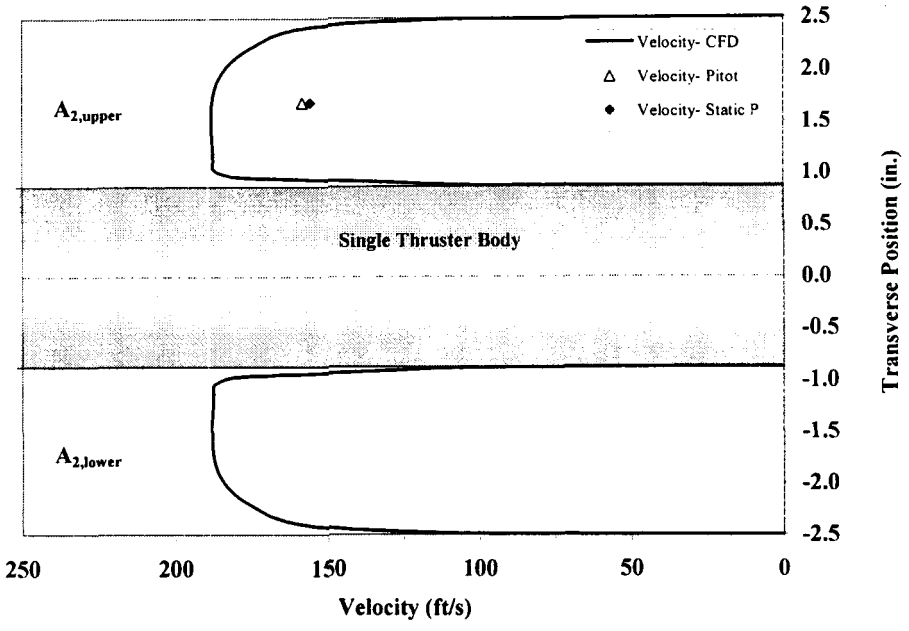

Fig. 5.29. Thruster body region velocity profiles for the Single configuration, O/F = 8 (x = -5.75 in.).

the CFD value in $A_{2,upper}$. The measured value in $A_{2,center}$, on the other hand, is ~2.6 times the CFD value (476 vs. 181 ft/s).

The measured velocity in $A_{2,upper}$ for the single thruster (Fig. 5.29) is lower than the CFD prediction by ~ 16%. As noted in the discussion of Figs. 5.15 and 5.25, there is an asymmetry in the air flow upstream and downstream of the thruster body region for the Single configuration. Those two figures show that the air velocity below the centerline is higher than the velocity above it. The same trend would be expected in the thruster body region. The velocity in $A_{2,lower}$ should be greater than the measured value in $A_{2,upper}$.

Velocities and flow rates for all three configurations at O/F = 8 are summarized in Table 5.7. In general, the procedures for calculating the effective areas and static densities were the same as those used to generate the results in Table 5.5. One difference is that the velocities in Table 5.7 are the values at the center of each region in the transverse direction (y), rather than an average over some transverse distance. The percentage of the total air flow rate in each region is included in Table 5.7. The CFD mass flow rates in each region were calculated using Equation 5.7. The total flow rates from all regions for the CFD results shown in Table 5.7 were within ± 0.25% of the CFD values in Table 5.5 for each configuration. Since the velocity was not measured in the $A_{2,lower}$ region, a different procedure was used for the experimental mass

Table 5.7. Summary of velocity and mass flow rate data at O/F = 8 in the thruster body region.

		Single			Twin A			Twin B		
Parameter	Units	CFD Value	xperiment Value	% Δ	CFD Value	xperiment Value	% Δ	CFD Value	xperiment Value	% Δ
Inlet Air Flow Rate	(lb_m/s)	**0.837**	**1.055**	**26.0**	**0.853**	**1.039**	**21.8**	**0.859**	**1.274**	**48.3**
Isolator Air Flow Rate	(lb_m/s)	**0.837**			**0.851**			**0.857**		
Upper Region ($A_{2,upper}$)										
Centerline Velocity	(ft/s)	**187.9**	**158.2**	**-15.8**	**152.5**	**176.8**	**15.9**	**212.2**	**219.6**	**3.5**
Geometric Area	(in^2)	4.88			3.56			2.44		
Area Correction Factor	--	0.915			0.855			0.881		
Effective Area	(in^2)	4.46			3.05			2.15		
Density	(lb_m/ft^3)	0.0719	0.0726	1.0	0.0722	0.0724	0.3	0.0715	0.0745	4.2
Air Flow Rate	(lb_m/s)	**0.419**	**0.356**	**-15.0**	**0.233**	**0.271**	**16.3**	**0.226**	**0.244**	**7.8**
Percent of Total	(%)	50.0	33.7	-32.5	27.4	26.1	-4.8	26.4	19.1	-27.5
Mass Flux	(lb_m/in^2-s)	0.0859	0.0730	-15.0	0.0654	0.0760	16.3	0.0928	0.1000	7.8
Center Region ($A_{2,center}$)										
Centerline Velocity	(ft/s)				**330.3**	**493.6**	**49.4**	**181.4**	**476.3**	**162.6**
Geometric Area	(in^2)				2.63			4.88		
Area Correction Factor	--				0.920			0.916		
Effective Area	(in^2)				2.42			4.47		
Density	(lb_m/ft^3)				0.0695	0.0663	-4.6	0.0719	0.0690	-4.0
Air Flow Rate	(lb_m/s)				**0.385**	**0.549**	**42.6**	**0.404**	**1.019**	**152.1**
Percent of Total	(%)				45.2	52.8	16.8	47.2	80.0	69.5
Mass Flux	(lb_m/in^2-s)				0.1466	0.2091	42.6	0.0829	0.2091	152.1
Lower Region ($A_{2,lower}$)										
Centerline Velocity	(ft/s)	**187.9**			**151.9**			**211.6**		
Geometric Area	(in^2)	4.88			3.56			2.44		
Area Correction Factor	--	0.915			0.860			0.883		
Effective Area	(in^2)	4.46			3.06			2.15		
Density	(lb_m/ft^3)	0.0719			0.0722			0.0715		
Air Flow Rate	(lb_m/s)	**0.419**	**0.699**	**67.0**	**0.233**	**0.220**	**-5.9**	**0.226**	**0.010**	**-95.4**
Percent of Total	(%)	50.0	66.3	32.5	27.4	21.1	-22.9	26.4	0.8	-96.9
Mass Flux	(lb_m/in^2-s)	0.0859	0.1434	67.0	0.0655	0.0616	-5.9	0.0927	0.0043	-95.4

NOTES :
1) Shaded boxes indicate no information is available
2) Flow rate in Lower Region is assumed to be the remainder of the total flow.

flow splits. Mass flow rates were calculated in the regions where velocity results was available. The flow rate in $A_{2,lower}$ was assumed to be the difference between the total measured inlet flow (Table 5.5) and the sum of the flows in the remainder of A_2.

The estimated Twin A mass flow split is fairly symmetric from top to bottom (26/53/21% for $A_{2,upper}/A_{2,center}/A_{2,lower}$), which is consistent with the symmetric inlet velocity profile (Fig. 5.23). The resulting mass flux through $A_{2,center}$ is ~3 times the value in the wall regions. The Twin B flow split appears to be unreasonable (19/80/1%), but without measurements in $A_{2,lower}$, no better estimate can be calculated. A key assumption in these air velocity and flow rate calculations is that the gas in the thruster body regions is pure air with a total pressure and temperature equal to the ambient values. The biasing of the primary flow streams toward the top and bottom walls for the Twin B configuration [3] may result in some hot gas recirculating back into $A_{2,upper}$ and $A_{2,lower}$. If hot gas did flow back into these regions, the calculated velocities and flow rates would no longer be accurate. Even with these uncertainties, it is clear that the highest mass flux for the Twin B configuration is through the center region.

In the case of the single thruster, the CFD model assumes symmetry about y = 0 in. Therefore, the single thruster CFD results in Table 5.7 are identical in $A_{2,upper}$ and $A_{2,lower}$ regions. The estimated air flow split based on the measured velocity is ~1/3 in the upper region and ~2/3 in the lower region. This split is consistent with the velocity asymmetry discussed earlier.

Table 5.8 summarizes the measured velocity and mass flow rate results for O/F = 4. The same calculation procedures were used to generate these results. Since there were no CFD results at O/F = 4, the effective areas from Table 5.7 were used. As with the results in Table 5.7, the measured velocities in $A_{2,center}$ are 2-4 times higher than the velocities in $A_{2,upper}$. The procedure for estimating the mass flow splits for both the Twin A (26/68/6%) and the Twin B (18/73/9%) configurations does not seem to produce reasonable results. The flow rates in $A_{2,lower}$ appear to be too low. The same issues related to the O/F = 8 results (Table 5.7) apply to the results in Table 5.8 as well. Despite this uncertainty with the flow split, it does appear that the mass flux through $A_{2,center}$ is significantly higher than it is through the near-wall regions.

Table 5.8. Summary of velocity and mass flow rate data at O/F = 4 in the thruster body region.

Parameter	Units	Single Thruster Experiment Value	Twin A (Ψ= 1.75 in.) Experiment Value	Twin B (Ψ= 2.50 in.) Experiment Value
Inlet Air Flow Rate	(lbm/s)		1.033	1.205
Upper Region ($A_{2,upper}$)				
Centerline Velocity	(ft/s)		173.8	191.2
Geometric Area	(in^2)		3.56	2.44
Area Correction Factor	--		0.855	0.881
Effective Area	(in^2)		3.05	2.15
Density	(lb_m/ft^3)		0.0737	0.0748
Air Flow Rate	(lb_m/s)		**0.271**	**0.213**
Percent of Total	(%)		26.2	17.7
Mass Flux	(lb_m/in^2-s)		0.0760	0.0875
Center Region ($A_{2,center}$)				
Centerline Velocity	(ft/s)		**690.1**	**426.7**
Geometric Area	(in^2)		2.63	4.88
Area Correction Factor	--		0.920	0.916
Effective Area	(in^2)		2.42	4.47
Density	(lb_m/ft^3)		0.0610	0.0663
Air Flow Rate	(lb_m/s)		**0.706**	**0.878**
Percent of Total	(%)		68.4	72.8
Mass Flux	(lb_m/in^2-s)		0.269	0.180
Lower Region ($A_{2,lower}$)				
Centerline Velocity	(ft/s)			
Geometric Area	(in^2)		3.56	2.44
Area Correction Factor	--			
Effective Area	(in^2)			
Density	(lb_m/ft^3)			
Air Flow Rate	(lb_m/s)		**0.056**	**0.114**
Percent of Total	(%)		5.4	9.4
Mass Flux	(lb_m/in^2-s)		0.0156	0.0467

NOTES:
1) Shaded boxes indicate no information is available
2) Flow rate in Lower Region is assumed to be the remainder of the total flow.

5.4. High Frequency Pressure Measurements

5.4.1. Background

The preceding sections have discussed the differences in the performance characteristics of the three thruster configurations. In particular, the higher air entrainment (~ 20%) and thrust (~ 8%) of the Twin B configuration differentiates it from the other two configurations. In an effort to understand the source of these differences, the available Twin B measurements were studied in detail.

One notable feature of the Twin B results was the shot-to-shot variation in the Raman images. Figure 5.30 includes a series of 13 consecutive nitrogen Raman images taken at 0.1 sec intervals during the steady-state portion of a Twin B configuration test. The images cover the

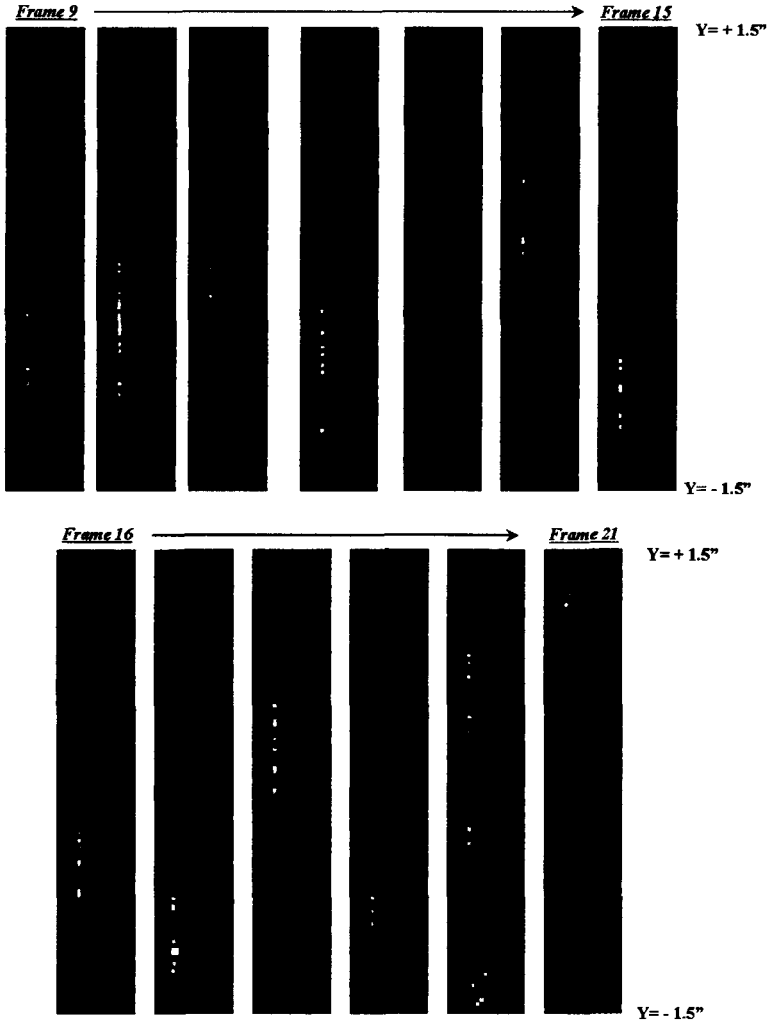

Fig. 5.30. Sequence of nitrogen Raman images for the Twin B configuration, O/F = 8.

transverse region from y = -1.5 in. to y = 1.5 in. at the axial position x = 2.4 in. The thruster centerlines are at y = ± 1.25 in., or just slightly inside the top and bottom edges of the images. The bright region in each image indicates the area with a high nitrogen number density. Since little mixing has occurred in the combustor at this point, these images may be viewed as the transverse extent of the air flow between the thrusters. In this sequence of images, the air stream moves up and down from one thruster centerline to the other in a seemingly random manner. This phenomenon suggests that large scale unsteadiness exists in this region. Since there is no discernible pattern in the sequence of images, this unsteadiness is either random or at a frequency higher than the Raman imaging frequency (10 Hz).

A literature review of ejector research showed several experimental studies where unsteady flow phenomena have been examined [20-26]. These experiments typically used a supersonic primary jet discharging into a duct, which was open to the ambient surroundings. Usually the primary stream was ambient-temperature, high-pressure air flowing through a converging nozzle. The main variable in these experiments was the ratio of the primary total pressure (P_o) to ambient pressure (P_a), which is denoted by the symbol R ($R \equiv P_o/P_a$). This ratio determines the pressure mismatch at the nozzle exit and the dominant frequency of the jet noise, which is often referred to as "screech."

Powell [27] originally described the mechanism that generates the screech tone of a supersonic jet in open air. He observed that the periodic Kelvin-Helmholtz instabilities in the primary/secondary shear layer grow in size and strength as they are convected downstream. He proposed that at some point these instabilities interact with the shock cell structures in the primary jet (Fig. 5.16) forming an acoustic source on both sides of the jet. The resulting sound waves emanate from these sources in all directions, but most strongly in the upstream direction. These sound waves have the same frequency as the instabilities in the shear layer. Some of the acoustic energy reaches the nozzle lip where the shear layer instabilities originate. This acoustic energy amplifies the instabilities, thus completing a feedback loop and locking in the screech frequency.

Unsteady ejector experiments have been performed with both axisymmetric [20-23] and rectangular [24-26] nozzles and ducts. Quinn [20, 21] used axisymmetric hardware in one of the first studies of unsteady ejector behavior. He observed that as the pressure ratio, R, was varied, the mass entrainment ratio ($\dot{m}_s/\dot{m}_p$) would suddenly increase on the order of 10%. Quinn noted

that the jumps corresponded to sudden shifts in the dominant frequency of the jet noise in the duct. He concluded that these sudden shifts were due to acoustic coupling between the jet screech tone and the natural frequencies of the duct. When the screech tone excited one of the duct modes, that mode frequency would become dominant in the duct. In turn, the acoustic energy at that mode frequency amplified the instabilities in the shear layer, thereby coupling the mode frequency and the screech tone. The net effect of this acoustic coupling is an amplification of the size and strength of the shear layer vortices. The spiral motion within these vortices is the mechanism that mixes the primary and secondary flow streams. Ultimately, it is this amplification of the vortices by acoustic coupling that is responsible for increasing the entrainment of the secondary flow.

Viets *et al.* [24] conducted similar experiments with rectangular hardware. They observed behavior similar to what Quinn reported, although with more modest increases in performance. They attributed the smaller performance gain to a mismatch between the jet screech frequency and the transverse acoustic modes of the duct. The screech tones were at high frequencies compared to the frequencies of the lowest duct modes. As a result, only the higher duct modes were excited. Viets *et al.* contend that acoustic energy concentrated in the higher modes is less effective in enhancing the entrainment process than it would be in lower modes.

In order to determine whether or not acoustic coupling was occurring in the RBCC experiments, the characteristics of the duct modes were examined. The frequency of a transverse acoustic mode in a rectangular duct is given by [24]:

$$f_{n,m} = \frac{a}{2}\sqrt{\left(\frac{n}{h}\right)^2 + \left(\frac{m}{w}\right)^2} \qquad [5.11]$$

where a is the acoustic velocity in the medium, and n and m are the mode numbers associated with the duct height (h) and width (w), respectively. The RBCC hardware was designed to have no flow field variations across the width of the duct. Consequently, no modes should be excited across the width, and Equation 5.11 simplifies to:

$$f_{n,0} = \frac{a \cdot n}{2 \cdot h} \qquad [5.12]$$

Figure 5.31 illustrates the instantaneous pressure profile of an acoustic mode in a rectangular duct, which in this case is the first transverse mode (1,0). The points of maximum pressure fluctuation (anti-nodes) are at the walls (y = ± 2.5 in.), and the point where the pressure

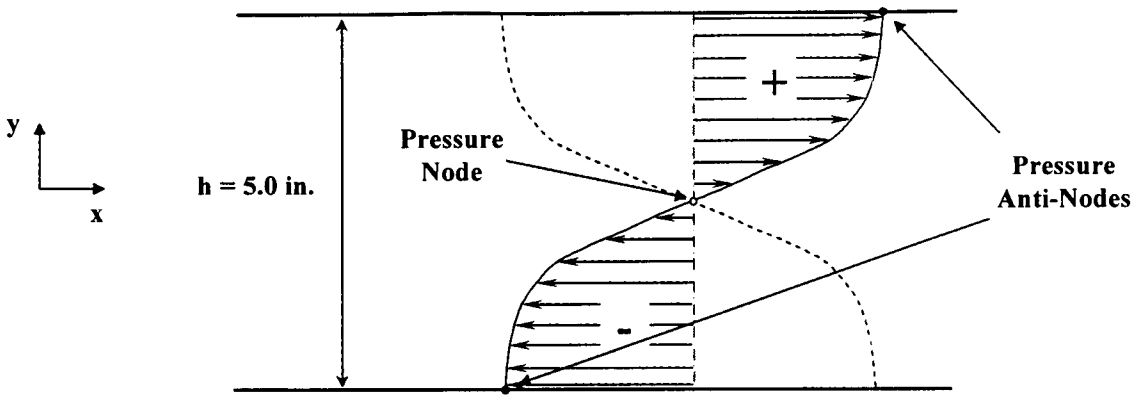

Fig. 5.31. First transverse acoustic mode (1,0) in a rectangular duct.

fluctuation is always zero (node) is at the centerline (y = 0 in.). All points above the pressure node have the same phase, ϕ, designated "+" in the figure, and all points below the node are 180 degrees out of phase with the top section ("-"). As time progresses, the acoustic pressure amplitude decreases across the entire duct height, until at some time, the amplitude is zero everywhere. The pressure amplitude then begins to increase in the opposite direction at every point until the profile becomes a mirror image of the original one. This second profile is shown as a dashed line in Fig. 5.31. The cycle then reverses itself until the pressure returns to the original profile. Using Equation 5.12, the frequency of this pressure oscillation is:

$$f_{1,0} = \frac{a}{2 \cdot h} \qquad [5.13]$$

The pressure profile and the mirror image for the second transverse mode (2,0) are shown in Fig. 5.32. In addition to the pressure anti-nodes at the walls, there is a third anti-node at the centerline. The two pressure nodes are at y = ± 1.25 in. In this case, the regions between the nodes and the walls have the same phase ("+"), and the region between the nodes is 180 degrees out of phase ("-"). For a rectangular duct, the frequency of the (2,0) mode is simply twice the frequency of the (1,0) mode. This pattern continues for any higher mode (n,0) – there are n nodes and n+1 anti-nodes; and the mode frequency is $f_{n,0} = n \cdot f_{1,0}$.

5.4.2. Measurements

For the GH_2/GO_2 rocket ejector (Twin A, Twin B and Single) configurations, high frequency pressure measurements were made in the constant area combustor section of the RBCC duct to assess the unsteady behavior of the flowfield. High frequency pressure

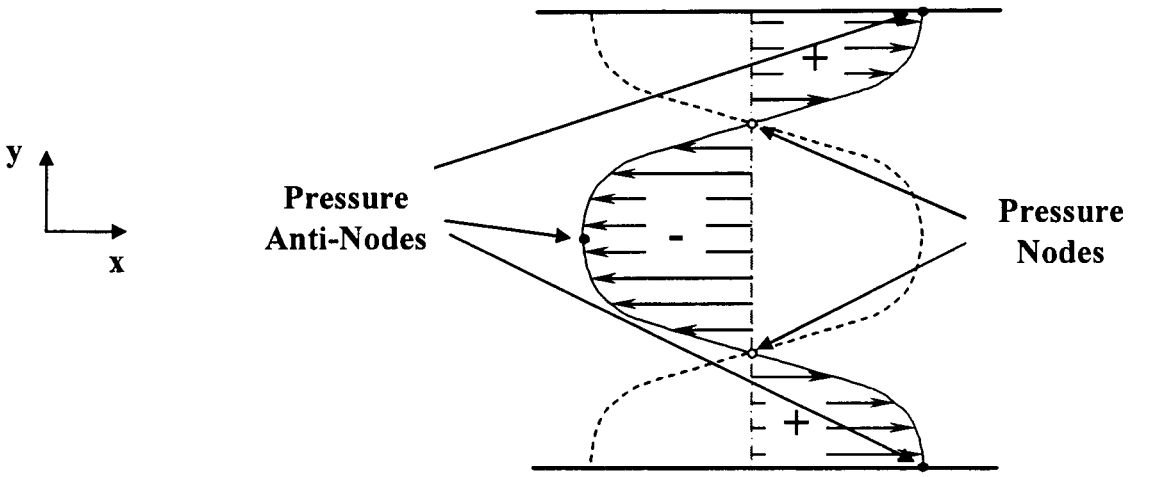

Fig. 5.32. Second transverse acoustic mode (2,0) in duct.

transducers placed at several locations in the duct as discussed in Section 3.7 were used to characterize unsteadiness evident in the flowfield.

The signals from the PCB high frequency pressure transducers were processed using two standard routines in the National Instruments LabVIEW™ software package [28]. In LabVIEW terminology these routines are referred to as "virtual instruments," or VIs. The first VI, the auto power spectrum (APS) function, transforms a fluctuating signal from the time domain to the frequency domain. Given a time-domain function $x(t)$, the auto power spectrum in the frequency domain, $S_{xx}(f)$, is given by:

$$S_{xx}(f) = X^*(f) \cdot X(f) = |X(f)|^2 \qquad [5.14]$$

where $X(f)$ is the Fourier transform of $x(t)$:

$$X(f) = \frac{1}{\sqrt{2\pi}} \cdot \int_{-\infty}^{\infty} x(t) \cdot e^{-if t} dt \qquad [5.15]$$

and $X^*(f)$ is the complex conjugate of $X(f)$. In general, if a complex number is expressed as $z = a + ib$, then its complex conjugate is $z^* = a - ib$, and the product $z \cdot z^* = a^2 + b^2$, is a real number [29].

The output from the APS VI is a table of acoustic power (psi^2/Hz) versus frequency (Hz). Data in this form is commonly referred to as a power spectrum density (PSD). PSD plots can be used to identify the dominant frequencies of a system. In addition, the PSD measurements can be used to determine the intensity of the entire fluctuating signal, or the intensity of an individual frequency peak. The area under the PSD curve across the entire spectrum, referred to as the total

variance (σ_T^2), gives the intensity of the total signal (psi^2). In the time domain, the total variance is a statistical measure of the signal fluctuation about the mean value. Similarly, the area under the PSD curve for an interval bracketing a particular frequency peak (f_i) gives the intensity of that peak (σ_i^2). The square root of variance, sigma, can be interpreted as the fluctuation of the total signal (σ_T) or of a particular frequency peak (σ_i) in terms of pressure (psi).

The cross-power spectrum (CPS) routine was the second LabVIEW VI used to process the signals. The CPS analysis compares two frequency measurements made during the same period of time at different locations. The CPS identifies the frequencies where the two signals are well correlated and the phase difference between the two signals ($\Delta\phi$) at those frequencies. Given two time-domain functions, x(t) and y(t), the cross power spectrum, $S_{xy}(f)$, is given by:

$$S_{xy}(f) = X^*(f) \cdot Y(f) \qquad [5.16]$$

where $X(f)$ and $Y(f)$ are the Fourier transforms of x(t) and y(t), respectively, and $X^*(f)$ is the complex conjugate of $X(f)$. The output of the CPS VI is a table of the cross power magnitude (psi^2/Hz) and phase difference (deg) vs. frequency (Hz). When CPS measurements were made during the RBCC experiments, one transducer was always mounted on the bottom wall (x = 2.4 in., y = -2.5 in., z = 0.0 in.). This transducer served as the reference point for all $\Delta\phi$ calculations.

As mentioned earlier, high frequency pressure measurements were made and analyzed for all three RBCC thruster configurations. Measurements were made during the steady state portion of hot-fire tests. Data points from a ~ 0.3 sec. time interval were processed with the APS VI. The resulting PSD output covers the frequency range from 0 to 25 kHz in increments of 1.526 Hz. Measurements from 3 or more tests were used to calculate an average value of the total variance (σ_T^2) for each transducer location.

Figure 5.33 depicts the PSD profile from a measurement made on the top wall at x = 2.4 in. for the Twin B configuration operating at O/F = 8. The dominance of the peak at 2200 Hz is obvious in the linear scale plot (Fig. 5.33(a)). This peak is the fundamental frequency (f) for this configuration/case. The first 4 harmonics ($2f$, $3f$, ...) are identified in the log scale plot (Fig. 5.33(b)). Although the power levels of these harmonics are roughly two orders of magnitude lower than the fundamental frequency, they are still stronger than the nearby broadband noise levels. In addition to the average total variance (σ_T^2), average values of σ_i^2 for

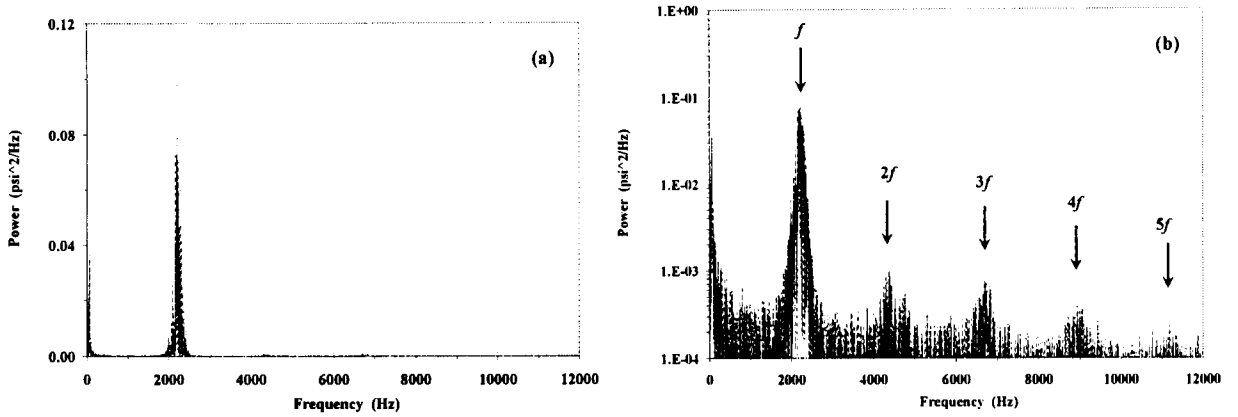

Fig. 5.33. PSD profile for Twin B configuration using (a) linear and (b) log scale.

the fundamental peak and the first two harmonics were also calculated for both Twin thruster configurations. All of these values, except for the intensity of the second harmonic, were also calculated for the single thruster configuration. Table 5.9 identifies the peak frequency and the frequency range used to calculate σ_i^2 for each peak of interest. The total variance for the Twin B test shown in Fig. 5.33 is 7.84 psi^2 and the variance of the fundamental peak (σ_1^2) is 5.38 psi^2. As Fig. 5.33(a) indicates, most of the acoustic power (~ 69%) in this test is associated with the fundamental frequency. Much of the remaining power (~ 18%) is at low frequency (< 500 Hz).

Figure 5.34 is the PSD profile for the Single thruster configuration at the same measurement location as Fig. 5.33. Although the Single thruster PSD has the same general characteristics as the Twin B PSD, there are some notable differences. The first peak in Fig. 5.34 is narrower and at a higher frequency than its counterpart in Fig. 5.33 (2840 vs. 2200 Hz). Only ~ 30% of the total power is present in this first peak, and almost as much power (28%) resides below 500 Hz. Three harmonics are identified in Fig. 5.34(b), but only the 2f and 3f peaks are distinguishable from the broadband noise.

The PSD plot for the Twin A configuration is shown in Fig. 5.35. The characteristics of this PSD are quite different than the previous two cases. The frequency of the dominant peak (4900 Hz) is roughly twice the frequency of the first peak in Figs 5.33 and 5.34. Figure 5.35(b) shows no discernible peak in the range where these other two dominant peaks reside (2000-3000 Hz). The dominant peak in Fig. 5.35 is broader than the corresponding peaks for the other two configurations. In addition, there is a smaller, secondary peak at ~ 4000 Hz. Secondary

Table 5.9. Frequency ranges used to calculate variance and sigma.

	Single	Twin A (Ψ = 1.75 in.)	Twin B (Ψ = 2.50 in.)
	Experimental Data - Frequency Range (Hz)		
Fundamental (i = 1)	**2840**	**4900**	**2200**
Minimum Value	2640	4600	1900
Maximum Value	3040	5200	2500
First Harmonic (i = 2)	**5680**	**9800**	**4400**
Minimum Value	5480	9300	4200
Maximum Value	5880	10,300	4700
Second Harmonic (i = 3)	**8520**		**6600**
Minimum Value	8320		6300
Maximum Value	8720		6900

peaks such as this one are not seen in the other two cases. An even broader 2f peak can be seen in Fig. 5.35(b). Excluding the secondary peak at 4000 Hz, approximately 50% of the total acoustic power is contained in the first peak. The power below 500 Hz is ~ 12% of the total. Another unique feature of the Twin A PSD is a discernible peak at 1000 Hz. Although it is clearly visible in Fig. 5.35, this peak only accounts for ~ 2% of the total acoustic power.

The features in Figs 5.33-5.35 indicate that the acoustic characteristics are different for each thruster configuration. While the Twin B and Single configuration cases have some common features, the Twin A configuration appears to be fundamentally different.

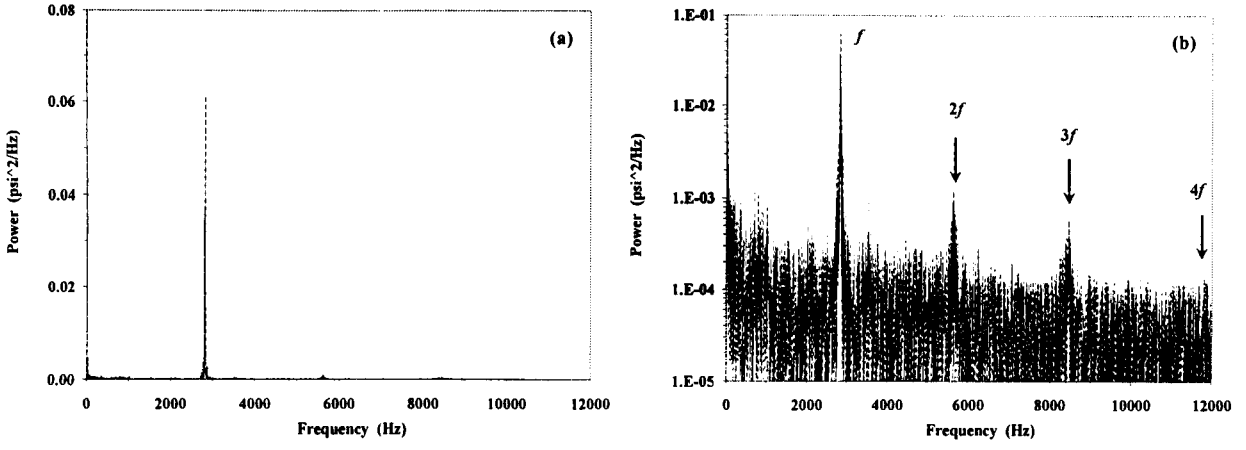

Fig. 5.34. PSD profile for Single configuration using (a) linear and (b) log scale.

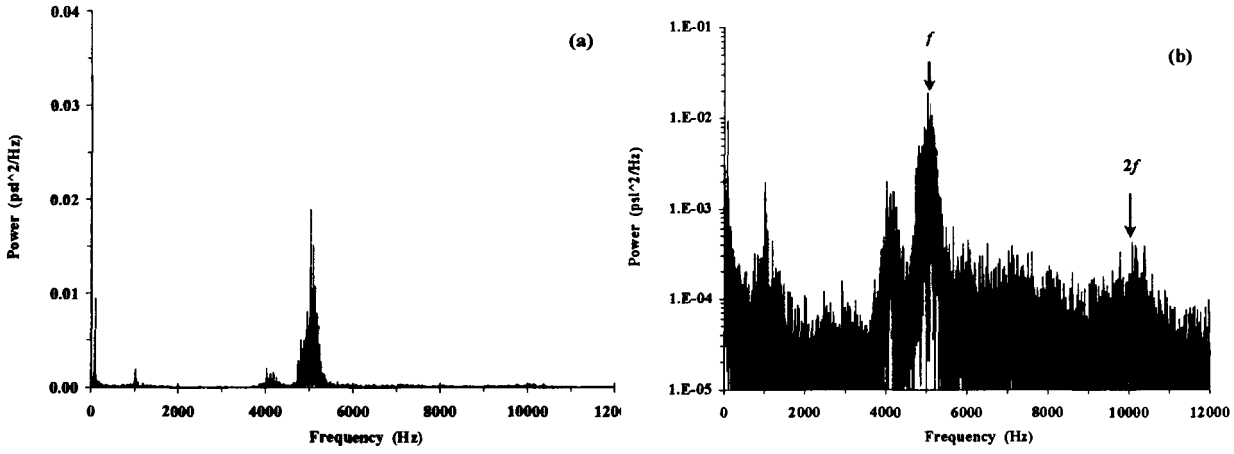

Fig. 5.35. PSD profile for Twin A configuration using (a) linear and (b) log scale.

The differences are more apparent in Fig. 5.36, which includes the PSDs from top wall measurements for all three configurations. In addition to the frequency differences, Fig. 5.36 indicates that the acoustic intensities of the three configurations are also different. Table 5.10 summarizes an analysis of the PSD profiles for all three configurations. Since the maximum pressure fluctuations occur at the anti-nodes, σ_T^2 and σ_1^2 were calculated at the top and bottom walls for each configuration. Because transverse asymmetry was present in all 3 cases, the top and bottom wall values were averaged for this comparison. In all three cases, σ_T^2 and σ_1^2 are

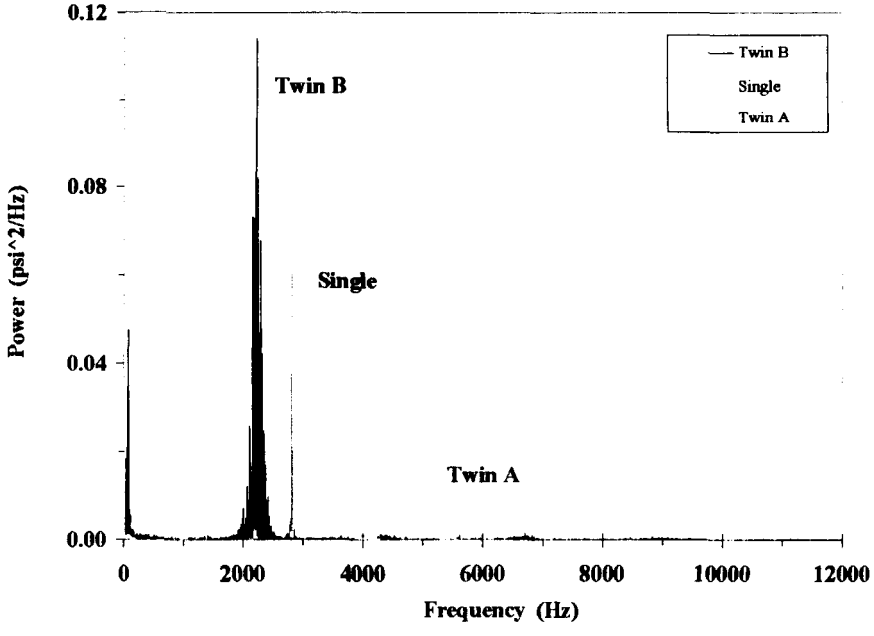

Fig. 5.36. Top wall PSD profiles for all three thruster configurations, O/F = 8.

Table 5.10. Comparison of variance values at the top and bottom walls, O/F = 8.

		Single	Twin A (Ψ = 1.75 in.)	Twin B (Ψ = 2.50 in.)
		Variance [σ^2] (psi^2)		
Top Wall	*Total :*	2.93	2.31	7.84
	Below 500 Hz :	0.83	0.27	1.13
	First Peak (f) :	0.86	1.10	5.40
Bottom Wall	*Total :*	16.47	8.42	11.55
	Below 500 Hz :	0.11	0.38	0.45
	First Peak (f) :	6.85	4.25	6.76
Average of Top & Bottom Walls	***Total :***	**9.70**	**5.37**	**9.69**
	Below 500 Hz :	**0.47**	**0.33**	**0.79**
	% of total :	4.8%	6.1%	8.1%
	Fund. Peak (f) :	**3.86**	**2.67**	**6.08**
	% of total :	39.7%	49.8%	62.7%

significantly higher at the bottom wall, but the intensity below 500 Hz is lower at the bottom wall. While the Single and Twin B configurations have essentially the same total intensity, the Twin B configuration has more of its intensity located at the first frequency peak (63% vs. 40%). The total variance of the Twin A configuration is approximately half the Twin B value (5.37 vs. 9.69 psi^2), and the same is true for the intensity of the first peak of the Twin A configuration (2.67 vs. 6.08 psi^2).

The intensity below 500 Hz was calculated for all three cases (Table 5.10). Significant acoustic power at low frequencies may indicate the presence of longitudinal modes in the duct. A cut-off value of 500 Hz was estimated to be the highest frequency the fundamental longitudinal mode could produce. This value assumes the shortest possible length scale (L) and the highest possible acoustic velocity in the frequency calculation:

$$f_L = \frac{a}{2 \cdot L} \qquad [5.17]$$

The length of the constant-area combustor (35.3 in.) was used for L rather than the overall duct length, and the acoustic velocity was assumed to be the equilibrium value for the primary/secondary mixture (~ 2900 ft/s). In all three cases, the average low frequency intensity

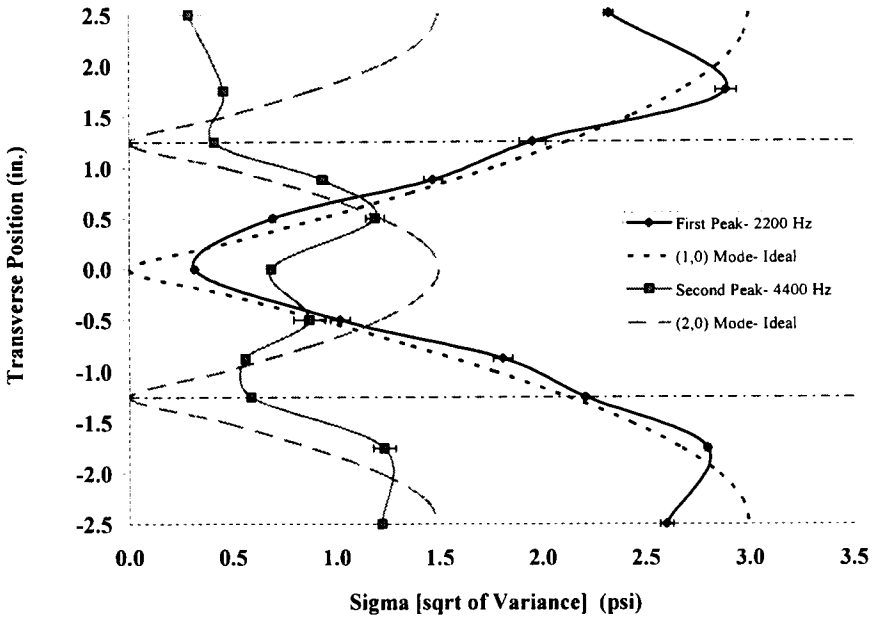

Fig. 5.37. Acoustic pressure amplitude profiles for the Twin B configuration, O/F = 8.

(< 500 Hz) was less than 10% of the total. Therefore, it does not appear that low frequency longitudinal modes play a significant role in the RBCC duct acoustics.

The results from both the APS and the CPS VIs were used to determine whether the peak frequencies identified in Table 5.9 were associated with transverse acoustic modes in the duct. High frequency pressure measurements were made at the 9 side wall positions, as well as on the top and bottom walls, at x = 2.4 in. (see Fig. 3.4). The average sigma values at the peak frequencies were used as a measure of the pressure fluctuation at those points.

Figure 5.37 presents the average sigma values for the first two peaks from the Twin B frequency measurements (2200 and 4400 Hz). In this figure, and others that follow, the thruster centerline positions are identified by horizontal dash/dot lines, and the error bars on the average data points represent ± 1 standard deviation. The dashed curves in Fig. 5.37 represent the absolute value of the pressure amplitudes for ideal (1,0) and (2,0) transverse modes as depicted in Figs. 5.31 and 5.32. These ideal amplitude curves have the form:

$$A(y) = A_1 \cdot \left|\sin\left(n \cdot \pi \frac{y}{h}\right)\right| \qquad \text{for odd mode numbers } (n = 1, 3, \ldots), \qquad [5.18]$$

or

$$A(y) = A_2 \cdot \left|\cos\left(n \cdot \pi \frac{y}{h}\right)\right| \qquad \text{for even mode numbers } (n = 2, 4, \ldots). \qquad [5.19]$$

The amplitude constants (A_1, A_2) in Equations 5.18 and 5.19 were arbitrarily set to match the data points as closely as possible. Since the objective was to determine which modes, if any, were present in the duct, the primary concern was with the shape of the curves, not their amplitudes. The measured amplitude profile for the peak at 2200 Hz is fairly symmetric, and it follows the ideal (1,0) mode curve closely, except at the duct centerline and the top/bottom walls. The deviation at the centerline is understandable because the flow field is unsteady (Fig. 5.30). Any slight variation in the location of the pressure node will result in some fluctuations being detected by the transducer at y = 0 in. The deviations on the top and bottom walls could be due to the fact that these measurements were made at the center of the duct (z = 0 in.), rather than along the side wall (z = -1.5 in.) as with the other nine measurements (see Fig. 3.4). Another possible explanation is that the deviation is due to less than perfect reflections of the acoustic waves at the top/bottom walls.

The average values of sigma for the 4400 Hz peak follow the ideal (2,0) mode curve in Fig. 5.37 fairly well. Again, deviations are seen at the centerline and the top/bottom walls. Sigma values at the higher harmonics were also examined, but the PSD values at these higher frequencies tended to be close to the background noise levels. In addition, the eleven measurement points did not provide adequate spatial resolution for plotting the higher transverse modes. As a result, well-defined mode shapes could not be distinguished beyond the second peak.

Figure 5.38 depicts a typical magnitude plot from a cross power spectrum (CPS) calculation. In this case the analysis is for the Twin B configuration with the transducers mounted on the top and bottom walls. The peak CPS magnitudes occur at the same frequencies as the peaks in the PSD (2200, 4400, ... Hz), indicating that both transducers are sensing the same peak frequencies. Fig. 5.39 presents the corresponding phase difference measurements. As seen in Fig. 5.39(a), there appears to be no coherent phase relationship between the two signals across most of the frequency spectrum. The values tend to jump around randomly between $\Delta\phi = 0°$ and 360°. Closer inspection (Fig. 5.39(b)) reveals that there are regions where $\Delta\phi$ has a fairly well-defined value. These regions correspond to the frequencies of the CPS magnitude peaks. A moving average was used to smooth the results in Fig. 5.39(b). Over a frequency range ($2150 < f < 2250$ Hz) that corresponds to the first peak in the CPS magnitude

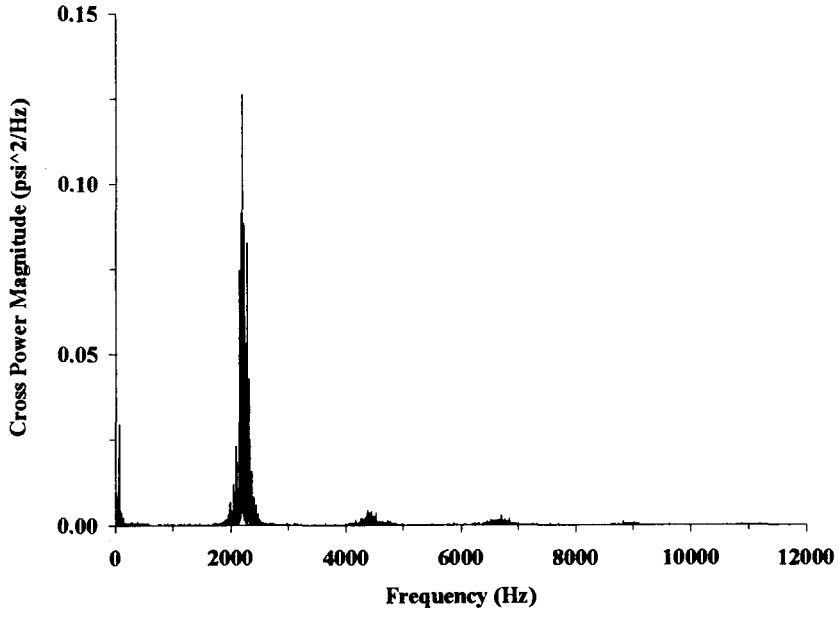

Fig. 5.38. Cross power magnitude for the Twin B configuration, O/F = 8, at y = -2.5 in. and y = +2.5 in.

plot, the average phase difference is approximately 174 degrees. As discussed in Section 5.4.1, the ideal (1,0) phase difference between these two points is 180 degrees.

The phase angle results from the CPS analysis for the Twin B configuration are presented in Fig. 5.40. The phase angle measurements for the first two frequency peaks and the ideal phase relationship for the (1,0) and (2,0) modes are plotted in the same format as the amplitude data in Fig. 5.37. As discussed earlier, all phase angle measurements are referenced to a transducer on

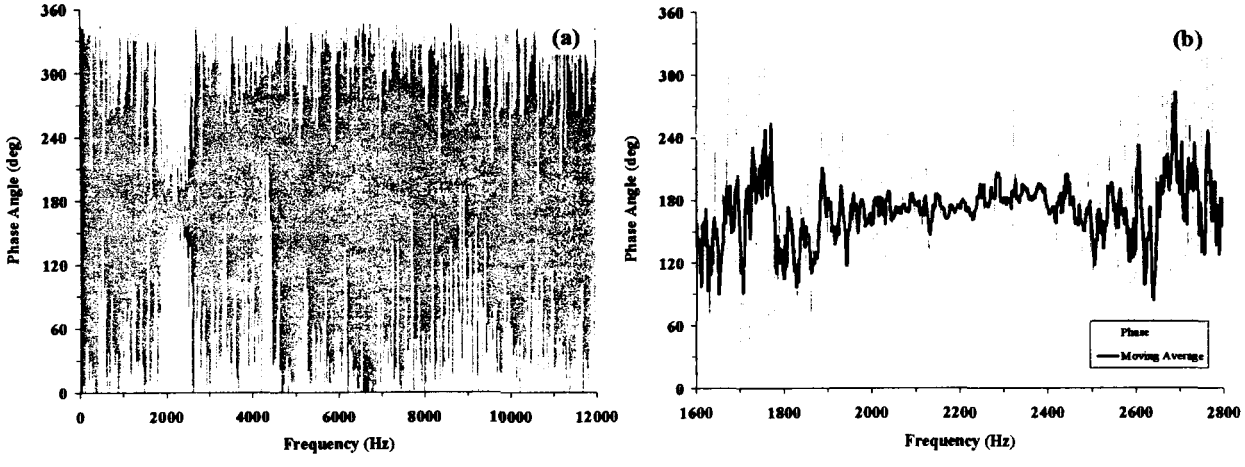

Fig. 5.39. Cross power phase difference for the Twin B configuration, O/F = 8, at y = -2.5 in. and y = +2.5 in.

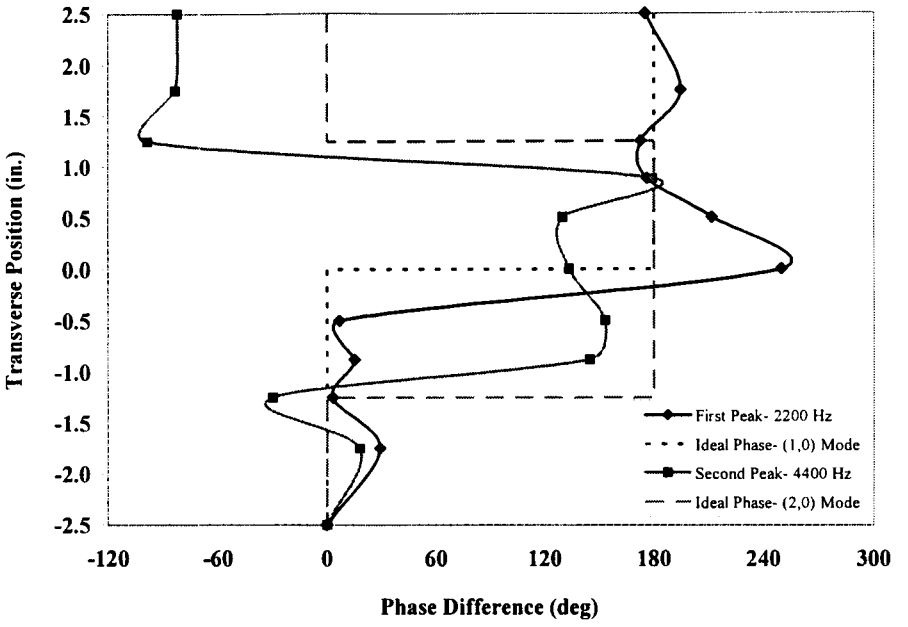

Fig. 5.40. Pressure oscillation phase angle profiles for the Twin B configuration, O/F = 8.

the bottom wall (y = -2.5 in.). The phase angle at that point has been arbitrarily set equal to zero in Fig. 5.40. The phase angle results for the 2200 Hz peak follow the ideal (1,0) curve fairly well. Points below the centerline have roughly the same phase angle as the reference point, and points above the centerline are ~ 180 degrees out of phase. As with the PSD profiles, some deviation is present at the centerline. The profile of the peak at 4400 Hz has the general features of the ideal (2,0) curve, especially below the centerline. The most notable deviations are near the top wall, where the measured phase angles were ~ -90° rather than the ideal value of 0°. Despite the noted deviations, Figs. 5.37 and 5.40 clearly show that transverse modes are present in the duct for the Twin B configuration. The dominant frequency at 2200 Hz corresponds to a (1,0) mode, and the first harmonic at 4400 Hz corresponds to a (2,0) mode.

Figure 5.41 presents the transverse sigma profiles for the Single configuration. In this case, the dominant frequency (2840 Hz) is a (2,0) mode. The first harmonic (5680 Hz) follows the profile of the ideal (4,0) mode reasonably well, although additional measurements would help define the shape of the curve more clearly. As with the static pressure map (Fig. 5.15) and the inlet velocity profile (Fig. 5.25) for the Single configuration, a definite top/bottom asymmetry is present in Fig. 5.41. The sigma values at 2840 Hz and 5680 Hz are 2-3 times larger on the bottom wall than on the top wall. As with the static pressure and velocity measurements, these results indicate that the flow field is more energetic in the lower half of the

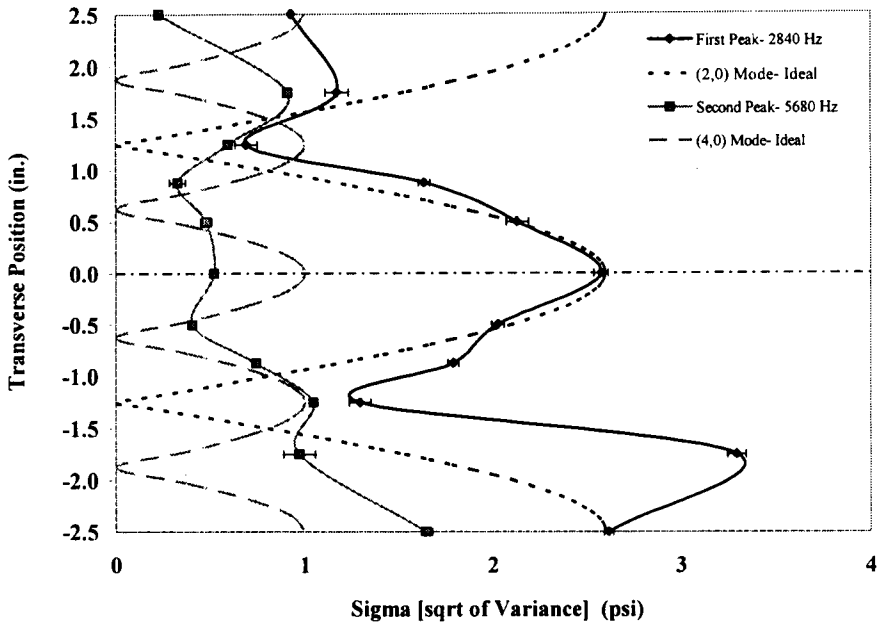

Fig. 5.41. Acoustic pressure amplitude profiles for the Single configuration, O/F = 8.

duct. The phase angle measurements for the single thruster (Fig. 5.42) are generally in agreement with the ideal (2,0) and (4,0) curves. As with the Twin B phase angle measurements, the largest deviations occur at the centerline and the top wall. The results in Figs 5.41 and 5.42 confirm the presence of the (2,0) and (4,0) transverse modes for the Single configuration.

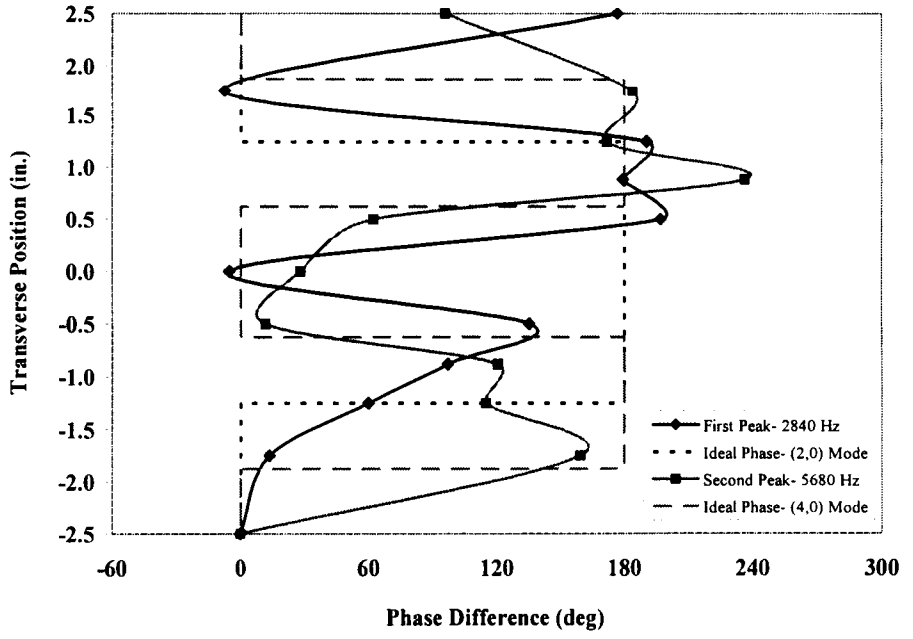

Fig. 5.42. Acoustic pressure phase angle profiles for the Single configuration, O/F = 8.

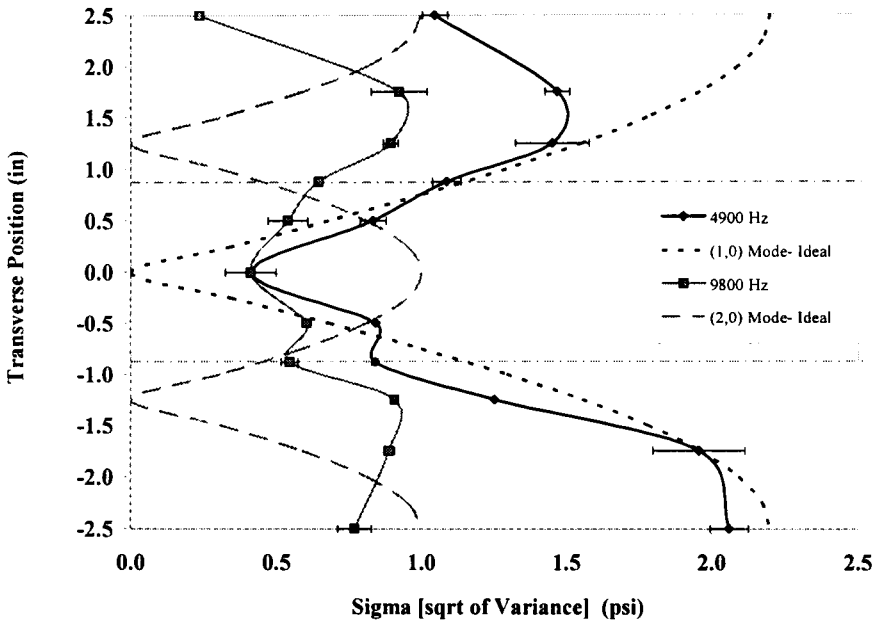

Fig. 5.43. Acoustic pressure amplitude profiles for the Twin A configuration, O/F = 8.

As with the PSD plots, the transverse sigma profile for the Twin A configuration (Fig. 5.43) differs fundamentally from the other two configurations. The measurements for the first major peak (4900 Hz) follow the ideal (1,0) mode profile reasonably well. However, the measurements at 9800 Hz look nothing like the ideal (2,0) profile. In fact, the profile for 9800 Hz has essentially the same shape as the 4900 Hz measurements, only at a lower amplitude. An explanation for this behavior is not obvious from the available measurements. A reference transducer on the bottom wall was not used for the Twin A tests. As a result, no phase angle information is available to help interpret the Twin A behavior.

In summary, there is clear evidence that transverse acoustic modes do occur in the duct for the Single and Twin B configurations, but the Twin A results are inconclusive. The intensity of the Twin B dominant frequency (σ_1^2) is ~1.5 times the corresponding intensity of the single thruster configuration at the top/bottom walls. This acoustic energy is in a (1,0) mode for the Twin B configuration, as opposed to a (2,0) mode for the single thruster configuration. Viets *et al.* [24] suggest that acoustic coupling is more effective at increasing the ejector entrainment ratio when the energy is in lower modes. The combination of the higher intensity (σ_1^2) and the lower mode number for the Twin B configuration helps explain why it is able to entrain ~20% more air than the single thruster configuration. The Twin B intensities (σ_T^2 and

σ_1^2) are approximately twice the corresponding Twin A values. This intensity difference, plus the fact that it is unclear if acoustic coupling is even occurring for the Twin A configuration, explains the higher entrainment for the Twin B configuration.

Finally, the results in this section raise three fundamental questions:

1) Why do the 3 configurations have different dominant frequencies?
2) Why does the Twin B configuration have a dominant (1,0) mode and the Single configuration have a dominant (2,0) mode?
3) Why are the high frequency pressure characteristics of the Twin A configuration fundamentally different than the characteristics of the Single and Twin B configurations?

The next section addresses the first question. As noted earlier, transverse duct modes have been observed in other experimental ejector studies [20-26]. None of these other studies have been able to identify the mechanism that drives the selection of a specific mode in the duct. The results of this study have not been able to identify a mechanism either. Finally, additional testing of Twin A configuration would be required to answer the third question.

5.4.3. Frequency Analysis

In order to understand the peak frequency differences between the three configurations, an effort was made to predict the mode frequencies. The first attempt to calculate the mode frequencies used Equation 5.11 assuming the acoustic velocity is known and constant across the flow field. Table 5.11 compiles the first several mode frequencies for the RBCC duct geometry. Three different acoustic velocities were used to calculate these frequencies. The first column uses the acoustic velocity of air at ambient temperature (1140 ft/s), and the second column uses the value of the thruster exhaust products for O/F = 8 (~ 4100 ft/s). These two values of acoustic velocity represent the lower and upper physical limits for this analysis. Since the gases in the duct are a mixture of air and thruster exhaust products, the measured mode frequencies should fall somewhere between these limits. The third column in Table 5.11 uses the acoustic velocity of the equilibrium composition of the air/thruster exhaust mixture (~ 2900 ft/s).

The (1,0) mode for the Twin B configuration has a measured frequency of 2200 Hz. None of the (1,0) frequencies in Table 5.11 are close to that value. The (0,1) mode frequency is close (2280 Hz), but this mode is not physically consistent with the observed mode characteristics (Fig. 5.37). The first mixed mode, (1,1), is ruled out because its frequency is

Table 5.11. Transverse mode frequencies of the RBCC duct for various speeds of sound.

	a (ft/s) →	Air 1140	Thruster 4100	Mixed 2900
Mode Numbers (n,m)		Mode Frequency (Hz)		
Height n	Width m			
1	0	1,368	4,920	3,480
2	0	2,736	9,840	6,960
3	0	4,104	14,760	10,440
4	0	5,472	19,680	13,920
0	1	2,280	8,200	5,800
0	2	4,560	16,400	11,600
0	3	6,840	24,600	17,400
1	1	2,659	9,563	6,764
2	1	3,561	12,809	9,060
3	1	4,695	16,885	11,943
1	2	4,761	17,122	12,111
2	2	5,318	19,126	13,528
3	2	6,135	22,064	15,606

higher than the measured value, even for the pure air case (2659 vs. 2200 Hz). All other combinations of mode numbers and acoustic velocity produce frequencies higher than 2200 Hz, ruling out these modes as well. Since the measured (1,0) frequency falls mid-way between the values for pure air and the equilibrium mixture in Table 5.11, a more detailed approach is required to predict this frequency.

The dominant frequency (2840 Hz) for the single thruster corresponds to the (2,0) mode. This frequency is slightly higher than the pure air frequency for the (2,0) mode in Table 5.11 (2736 Hz). The calculated frequency for the mixed gas case is significantly higher (6960 Hz) than the measured value for this mode. The high acoustic velocity of the hot thruster exhaust appears to have little effect on the mode frequency in this case. The single thruster acoustics behave as if the duct contained nearly pure air at ambient temperature.

The first frequency peak for the Twin A configuration appears to be a (1,0) mode in Fig. 5.43. The measured frequency (4900 Hz) is close to the (1,0) frequency calculated with the thruster exhaust acoustic velocity (4920 Hz). However, it is not reasonable to assume that this acoustic velocity would be present across the entire duct height. The only other frequency in Table 5.11 close to the measured value is the (1,2) mode for pure air (4761 Hz). At this point, this mode can not be ruled out.

The preceding analysis provides only limited insight into the frequency modes of the three thruster configurations. The assumption of a constant acoustic velocity across the entire duct height is too simplistic for these flow fields. As shown in the Raman figures for Phase I results in the addendum report [3], there are wide variations in the transverse temperature and species mole fraction profiles at the axial location of interest (x = 2.4 in.). As a result, the acoustic velocity also varies across the duct:

$$a(y) = \sqrt{\frac{\gamma(y) \cdot R_u \cdot T(y)}{MW(y)}} \qquad [5.20]$$

where $\gamma(y)$ and $MW(y)$ are the values of the gas mixture at each transverse position. The effects of a variable acoustic velocity should be incorporated into the analysis in order to develop a better understanding of the frequency characteristics.

Kapur *et al.* [30] developed a model for analyzing a similar acoustic mode problem. They were interested in predicting the frequency of longitudinal modes in a long tube with axial temperature and density gradients. Using their approach as a point of departure, the wave equation for transverse modes in a rectangular duct with variable properties was derived. This new model is restricted to acoustic modes in one transverse direction (y), and the mean fluid properties can only vary in that direction. The model assumes that the mean pressure ($\bar{p}$) is uniform across the flow field, and the mean axial velocity ($\bar{u}$) is negligible. Neither of these assumptions is completely valid for the RBCC flow field. There are significant pressure gradients in both the transverse and axial dimensions, and the axial velocities in the primary jets are large. Despite these shortcomings, this model was viewed as a significant improvement over the analysis used to produce Table 5.11. The resulting non-dimensional wave equation has the form:

$$\frac{d^2 p}{dY^2} + [-\eta(Y)]\frac{dp}{dY} + \left[\frac{(k_o \cdot H)^2}{\xi(Y)}\right] p = 0 \qquad [5.21]$$

where,

$p \equiv$ fluctuating (acoustic) pressure, normalized by the pressure at the wall

$Y \equiv$ transverse position, normalized by the duct height, (y/H)

$k_{o,n} \equiv \omega_n / a_o$, wave number of transverse mode "n"

$\omega_n \equiv 2\pi \cdot f_n$, angular frequency of transverse mode "n"

$f_n \equiv$ frequency of transverse mode "n"

$H \equiv$ duct height ($H = 5$ in.)

The variable coefficients in Equation 5.21 account for transverse variation in the mean density ($\bar{\rho}$) and the acoustic velocity (a):

$$\eta(y) = \frac{1}{\bar{\rho}} \cdot \frac{d\bar{\rho}}{dy} \qquad [5.22]$$

$$\xi(y) = \frac{a^2}{a_o^2} = \frac{\gamma T}{\gamma_o T_o} \cdot \frac{MW_o}{MW} \qquad [5.23]$$

The properties of air at 540°R are used for the reference values in Equation 5.23 (γ_o, T_o and MW_o). Equation 5.21 is an ordinary differential equation that can be solved numerically using a fourth order Runge-Kutta technique [31]. The integration proceeds from one wall ($Y = 0$) to the other ($Y = 1$), subject to the boundary conditions at the walls:

$$p(0) = 1\,, \qquad \left.\frac{dp}{dY}\right|_{Y=0} = \left.\frac{dp}{dY}\right|_{Y=1} = 0\,;$$

and at the centerline ($Y = 0.5$):

$p(0.5) = 0$ for odd modes (n = 1, 3, ...),

or

$$\left.\frac{dp}{dY}\right|_{Y=0.5} = 0 \quad \text{for even modes (n = 2, 4, ...).}$$

Two different approaches were used to generate the variable fluid properties used in Equations 5.22 and 5.23. The first approach used the fluid properties at the thruster exit plane (x = 0 in.). A modified "top hat" profile was created for each property needed for the integration. An example of these profiles is shown in Fig. 5.44, which is the temperature profile for the Twin B configuration. (All figures in this section use the normalized transverse position (Y), where $Y = 0$ is the bottom wall and $Y = 1$ is the top wall.) This profile has three distinct regimes, viz., the thruster flow, the air flow, and the mixing layer. The thruster flow area equals the exit area of each nozzle. The temperature in this region is the equilibrium temperature of the thruster exhaust (~ 5000°R). The air flow area includes the secondary flow passages and the base region of the nozzles, excluding the mixing layer. This region is assumed to be filled with ambient temperature air (540°R). The temperature profile in the mixing layers is a straight line between the thruster and air values. The normalized mixing layer thickness ($t^* = t/H$) was a

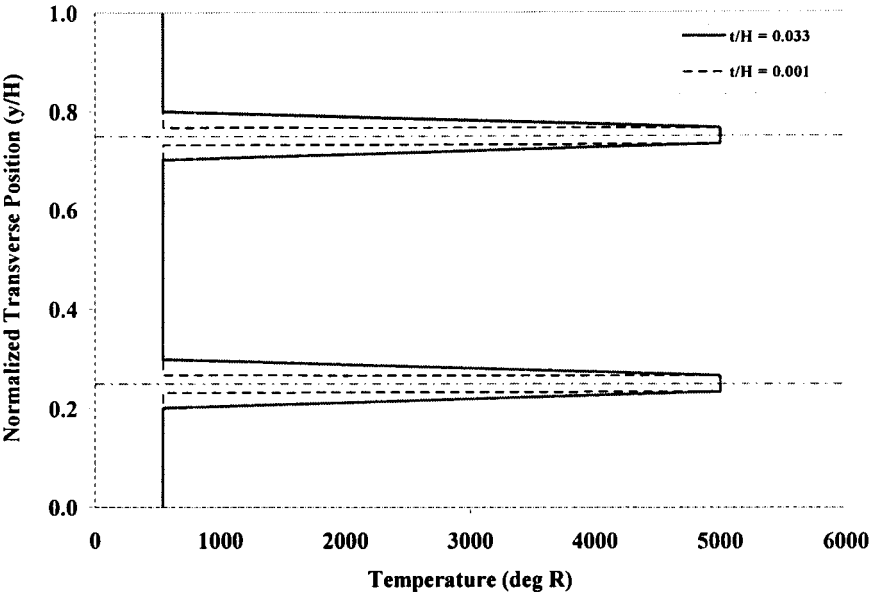

Fig. 5.44. Twin B exit plane temperature profile with two assumed mixing layer thicknesses (t/H = 0.001 or 0.033).

variable in the acoustic pressure calculations. The two profiles in Fig. 5.44 represent the assumed minimum and maximum mixing layer thicknesses. The maximum thickness ($t^* = 0.033$) is equal to the nozzle exit height.

Using the appropriate values for air and the thruster exhaust, profiles such as those shown in Fig. 5.44 were generated for all variable properties needed to integrate Equation 5.21. Parametric results for the (1,0) mode frequency versus t^* were generated for each thruster configuration (Fig. 5.45). In all three cases, the (1,0) mode frequency reaches a limiting minimum value for $t^* < 0.001$. The three asymptotic lines in Fig. 5.45 fall within a narrow frequency band. The Single configuration has the highest value (1955 Hz), and the Twin A configuration has the lowest value (1870 Hz). As t* increases, the (1,0) mode frequency increases non-linearly. The vertical dot-dash line in Fig. 5.45 represents the value of t^* equal to the nozzle exit height for the Twin thrusters (0.033). This thickness is half the single thruster exit height. Since the mixing layer has just begun to form at x = 0 in., this value of t^* should be a conservative upper limit. The difference between the frequencies at $t^* = 0.033$ and the asymptotic values is on the order of 100 Hz, which indicates that the assumed value of t^* is not critical for these calculations.

The mode frequencies from the exit plane calculations are summarized in Table 5.12, along with the corresponding measured frequencies. The model produced a reasonable estimate

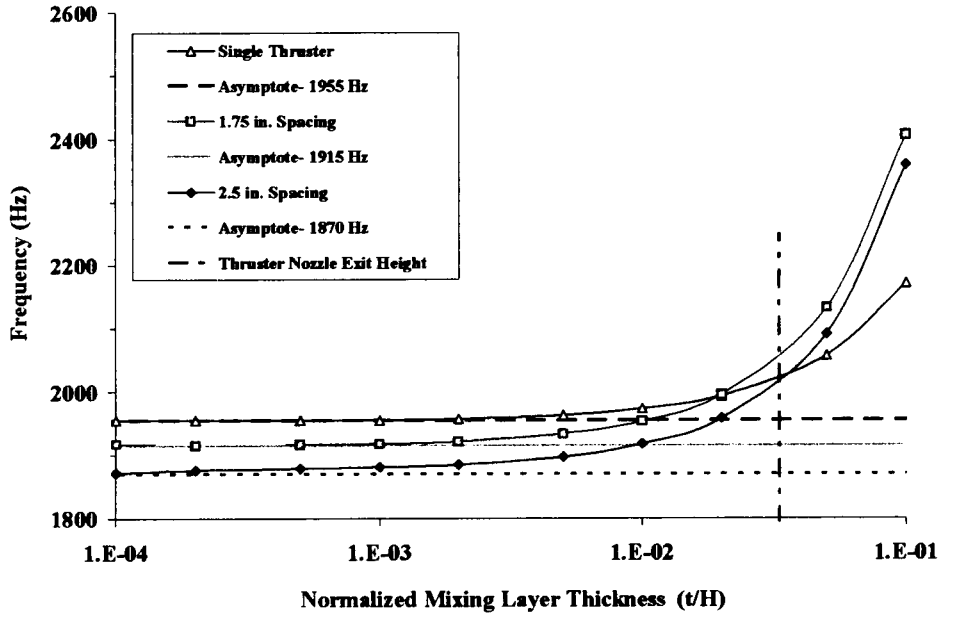

Fig. 5.45. Calculated values of (1,0) mode frequency at the thruster exit plane as a function of assumed mixing layer thickness (t/H).

of the Twin B (1,0) mode frequency (2000 vs. 2200 Hz). The calculated single thruster (2,0) mode frequency was ~ 40% higher than the measured value (4000 vs. 2840 Hz). The calculated (1,0) mode frequency for the Twin A configuration (1950 Hz) does not help explain the anomalous measured value (4900 Hz).

Table 5.12. Calculated acoustic mode frequencies using variable properties.

	Single	**Twin A (Ψ = 1.75 in.)**	**Twin B (Ψ = 2.50 in.)**
	Frequency (Hz)		
(1,0) Mode			
Measured	-- N/A --	4900	2200
Model- Exit Plane	~ 2000	~ 1950	~ 2000
Model- x = 1.4 or 2.4 in.	1833		2570
(2,0) Mode			
Measured	2840	9800	4400
Model- Exit Plane	~ 4000	~ 3900	~ 4000
Model- x = 1.4 or 2.4 in.	3666		5140

The second set of variable properties used to integrate Equation 5.21 was derived from the Phase I Raman measurements for the Twin B and Single configurations [3]. The property profiles were at x = 1.4 in. for the Twin B configuration and x = 2.4 in. for the Single configuration. Powell [27] observed that the acoustic sources of screech tones formed at the end of the third shock cell in a supersonic jet. The Raman measurements at x = 1.4 in. or 2.4 in. are in the vicinity of the third shock cell. The property profiles at these locations may be more representative of the conditions where the duct tones are generated than the exit plane values. The profiles for the Raman-derived properties were approximated by a series of straight line segments. Figures 5.46 (Twin B configuration) and 5.47 (Single configuration) show the Raman-derived temperature measurements and the curve fits used in the integration of Equation 5.21.

Results from the Twin B calculations are shown in Fig. 5.48. The (1,0) mode pressure profile has the same general shape as the ideal profile in Fig. 5.31. Comparing the pressure derivative curve (*dp/dY*) to the temperature profile in Fig. 5.46 shows that the pressure gradients are largest in the relatively cool region between the thruster centerlines ($0.25 < Y < 0.75$). The hot regions near the walls, which have a higher acoustic velocity than the center region, have very little impact on the shape of the mode curve. A similar trend is seen in the single thruster

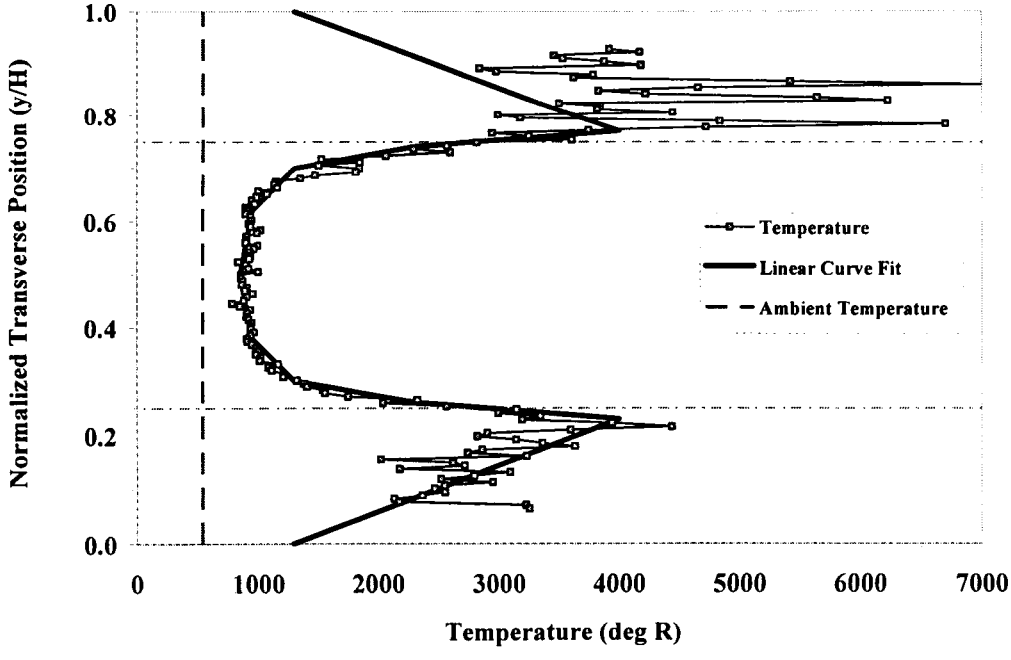

Fig. 5.46. Temperature profile at x = 1.4 in. for Twin B acoustic pressure calculations.

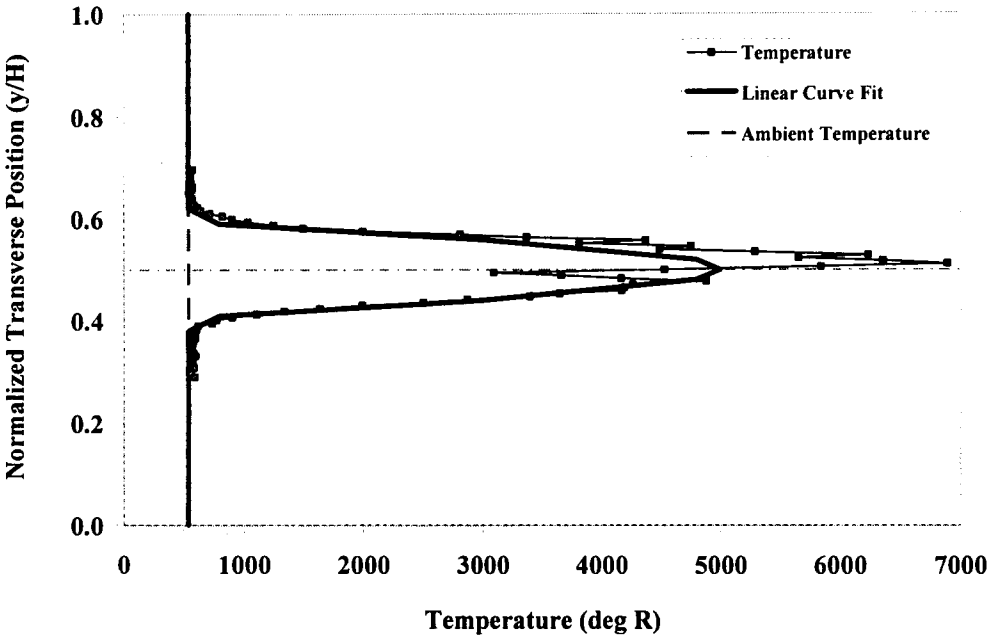

Fig. 5.47. Temperature profile at x = 2.4 in. for Single thruster acoustic pressure calculations.

results in Fig. 5.49. The (2,0) pressure profile is relatively flat in the hot primary flow near the centerline.

The results from this second set of calculations are also included in Table 5.12. In this case, the calculated (1,0) frequency for the Twin B configuration is greater than the measured

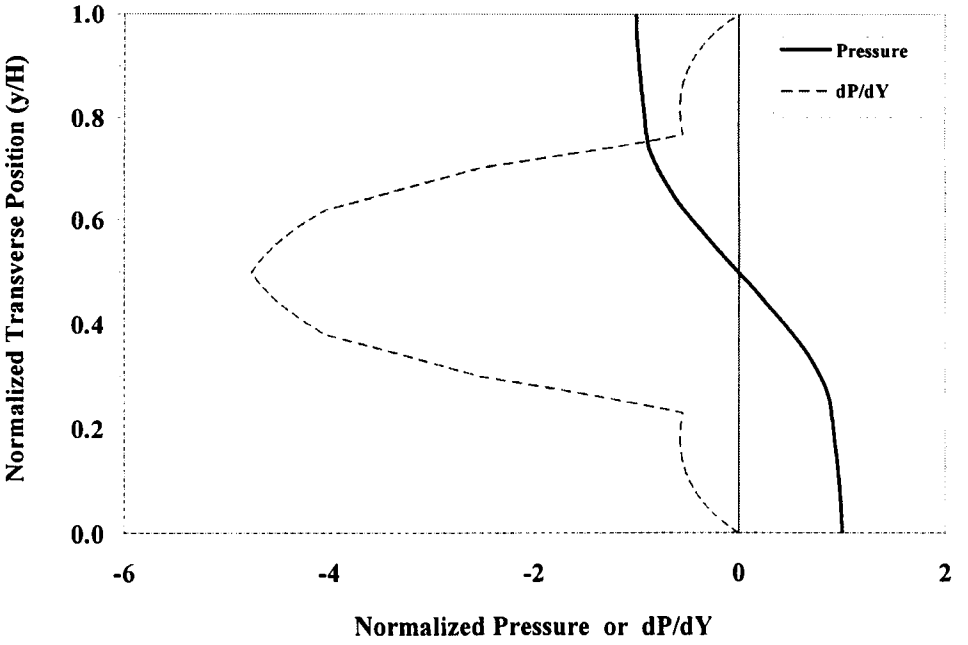

Fig. 5.48. Calculated acoustic pressure profile for the (1,0) mode with the Twin B configuration at x = 1.4 in.

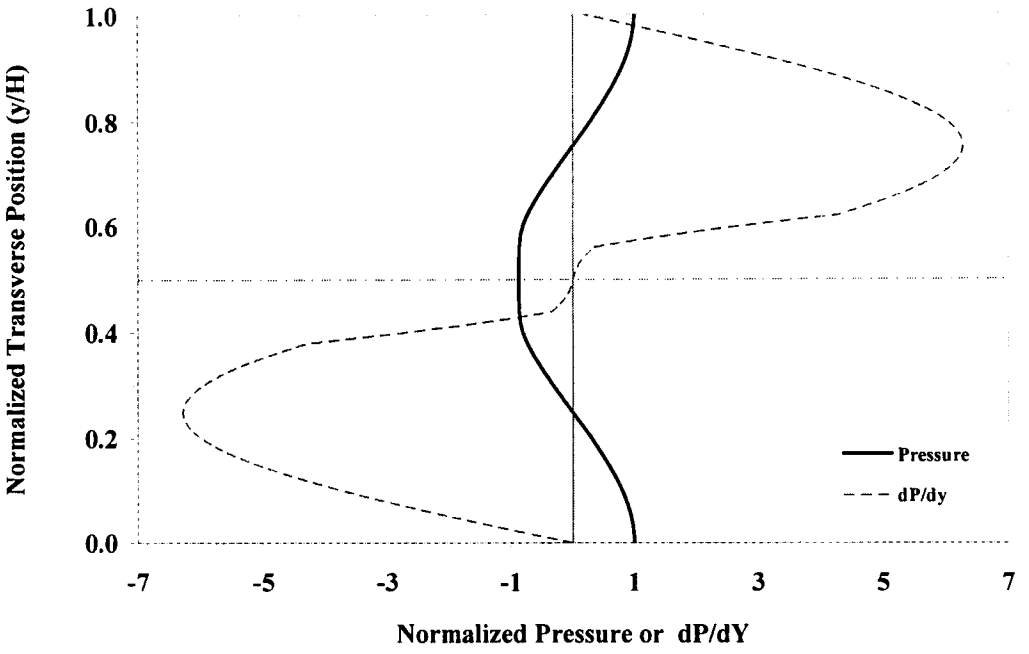

Fig. 5.49. Calculated acoustic pressure profile for the (2,0) mode with the single thruster configuration at x = 2.4 in.

value (2570 vs. 2200 Hz). The Twin B calculations at x = 0 in. and x = 1.4 in. bracket the measured value by approximately ± 10%. The calculated (2,0) mode frequency for the single thruster at x = 2.4 in. is 3666 Hz. This value is closer to the measured frequency (2840 Hz) than the first calculation (4000 Hz), but it still overpredicts the measured value by ~ 30%.

In summary, these calculations have shown that the Twin B mode frequencies can be reasonably predicted by accounting for the transverse variation in the properties. The mode frequencies for the Single configuration do not appear to be influenced by the properties of the hot primary flow. The measured (2,0) mode frequency is close to the value calculated for ambient temperature air in the duct (2840 vs. 2736 Hz). Finally, none of the mode frequency calculations in this section approach the high frequencies measured for the Twin A configuration.

6. SUMMARY

Experimental studies of rocket ejectors for application to RBCC engines have been completed that examine a set of key operational parameters which include propellant type (JP-7 or GH_2 with GO_2), O/F ratio (8 or 4), number of rockets (single or twin configurations) and geometric parameters such as rocket spacing. The extensive data base assembled as part of these studies is intended to provide both phenomenological insight as well as benchmark data for CFD model validation. Results obtained include both sea level static (SLS) and direct connect conditions for which flow rate, static pressure, heat flux and thrust measurements have been obtained. Additionally, the GH_2/GO_2 single and twin rocket studies have extensive static and high frequency pressure measurements to characterize the air entrainment processes at SLS conditions as a function of the number of rockets (1 or 2) and the spacing between the rockets. These studies have provided important insights into the potential of using unsteady ejector processes to enhance ejector performance in terms of pumping efficiency as well as in aiding the rapid mixing downstream of the rockets.

Specifically, the work that is reported here provides an important comparative data set for rocket ejectors utilizing JP-7/GO_2 as the propellants. Previous extensive work conducted in this laboratory on GH_2/GO_2 provides a baseline set of results from which to assess the performance of JP-7 as compared to GH_2. Given the recent increased interest in hydrocarbon fuels for both RBCC and rocket applications, these results are extremely timely for assessment of rocket engine and vehicle concepts utilizing hydrocarbon fuels for RBCC applications.

Similarly, the extension of the twin rocket studies that were initiated as part of a previous NASA funded effort have provided new and significant results related to the performance of unsteady ejector concepts. Measurements conducted as a function of the rocket spacing showed enhancement of both the air entrainment and thrust for the rocket ejector. Extensive static and dynamic pressure measurements indicated that there were significant differences in the pressure fields for the two rocket separation distances studied. In fact, for the case showing the highest mass entrainment and thrust enhancement, the dynamic pressure fields show evidence indicating that the excitation of the first and second transverse modes of the ejector chamber by the rocket plumes was significant. Simple analysis of the variable density flow present in the ejector duct downstream of the rocket plumes showed general agreement between the measured and predicted pressure oscillation frequencies. More analysis is clearly needed if a more detailed

understanding of the unsteady phenomena observed is to be achieved. Additionally, for the cases where significant unsteady pressure oscillations were present, mixing lengths between the flows from the rocket plumes and the entrained air flow were significantly shorter as compared to the rocket spacing where little unsteadiness was observed. Thus, these results demonstrate that unsteady ejector operation can result in significant performance and are worthy of more study since they can result in increased thrust and more compact engines, both of which improve engine thrust to weight.

In addition to this detailed report, a DVD summary of the data has been assembled for researchers wishing access to the data for model development and validation.

7. REFERENCES

[1] Escher, W. J. D., ed., *The Synerjet Engine: Airbreathing/Rocket Combined-Cycle Propulsion for Tomorrow's Space Transports*, PT-54, Progress in Technology Series, Society of Automotive Engineers, Warrendale, PA, 1997.

[2] Santoro, R. J. and Pal, S., Experimental and Analytical Modeling of the Rocket Ejector Mode of a Combined Cycle Rocket-Based Engine, Final Report Submitted to NASA MSFC for NASA Contract Grant NAS8-40890, June 2001.

[3] Santoro, R. J. and Pal, S., Focused RBCC Experiments: Two-Rocket Configuration Experiments and Hydrocarbon/Oxygen Rocket Ejector Experiments, Addendum Report for NASA Contract Grant NAG8-1844, September 2003.

[4] Odegaard, E. A. and Stroup, K. E., "1966 Advanced Ramjet Concepts Program, Volume VIII- Ejector Ramjet Engine Tests- Phase I," The Marquardt Corporation, Technical Report AFAPL-TR-67-118 Volume VIII, January 1968.

[5] Billig, F. S., Advanced Propulsion Technology Program, SSTO Low Speed System Assessment Final Report, The Johns Hopkins University Applied Physics Laboratory, JHU/APL AL-95-A050, 1995.

[6] Lehman, M. K., "Mixing and Reaction Processes in Rocket Based Combined Cycle and Conventional Rocket Engines," Ph.D. Thesis, The Pennsylvania State University, August 2000.

[7] Lehman, M., Pal, S., Schwer, D., Chen, J. D. and Santoro, R. J., "Focused Experimental and Analytical Studies of the RBCC Rocket-Ejector Mode," 36th JANNAF Combustion Subcommittee Meeting, Cocoa Beach, FL, October 18-21, 1999.

[8] Lehman, M., Pal, S. and Santoro R. J., "Experimental Investigation of the RBCC Rocket-Ejector Mode," AIAA Paper 2000-3725, 36th Joint Propulsion Conference, Huntsville, AL, July 2000.

[9] Greene, M. U., "Experimental Study of Rocket Based Combined Cycle Rocket-Ejector Mode for JP-7/GO2 Propellants," M.S. Thesis, The Pennsylvania State University, May 2000.

[10] Burkardt, L. A and Franciscus, L. C., RAMSCRAM--A Flexible Ramjet/Scramjet Engine Simulation Program, NASA Technical Memorandum 102451, 1990.

[11] McBride, B. J. and Gordon, S., Computer Program for Calculation of Complex Chemical Equilibrium Compositions and Applications, NASA Reference Publication 1311, June 1996.

[12] Ruf, J. H., "Benchmark of FDNS CFD Code for Direct Connect RBCC Test Data," AIAA Paper 2000-3726, July 2000.

[13] West, J., Ruf, J. H., Cramer, J., Pal, S., and Santoro, R., "Computational Insight to an Experimentally Observed Change in the Mixing Characteristics of an RBCC Engine in Ejector Mode," AIAA Paper 2001-3459, July 2001.

[14] Scheaffer, R. L. and McClave, J. T., "Hypothesis Testing," Chap. 8, *Probability and Statistics for Engineers*, 3rd ed., PWS-Kent, Boston, 1990, pp. 310-363.

[15] Seiner, J. M. and Norum, T. D., "Experiments of Shock Associated Noise on Supersonic Jets," AIAA Paper 79-1526, July 1979.

[16] Van Dyke, M., *An Album of Fluid Motion*, 1st ed., The Parabolic Press, Stanford, CA, 1998, p. 98.

[17] Zucrow, M. J., and Hoffman, J. D., *Gas Dynamics, Vol. 1*, 1st Ed., John Wiley & Sons, New York, 1976, pp. 172-174.

[18] Revington, P. R., *Data Reduction and Error Analysis for the Physical Sciences*, McGraw-Hill, New York, 1969.

[19] Thies, A. T. and Tam, C. K. W., "Computation of Turbulent Axisymmetric and Nonaxisymmetric Jet Flows Using the κ-ε Model," *AIAA Journal*, Vol. 34, No. 2, Feb. 1996, pp. 309-316.

[20] Quinn, B., "Effect of Aeroacoustic Interactions on Ejector Performance," *Journal of Aircraft*, Vol. 12, No. 11, Nov. 1975, pp. 914-916.

[21] Quinn, B., "Interactions between Screech Tones and Ejector Performance," *Journal of Aircraft*, Vol. 14, No. 5, May 1977, pp. 467-473.

[22] Abdel-Fattah, A. M. and Favaloro, S. C., "Duct Resonance and Its Effect on the Performance of High-Pressure Ratio Axisymmetric Ejectors," *AIAA Journal*, Vol. 26, No. 7, July 1988, pp. 791-798.

[23] Tam, C. K. W., Ahuja, K. K. and Jones III, R. R., "Screech Tones from Free and Ducted Supersonic Jets," *AIAA Journal*, Vol. 32, No. 5, May 1994, pp. 917-922.

[24] Viets, H., Campbell, J. R. and Korkan, K. D., "Acoustic Interactions in Ejectors," AIAA Paper 81-2045, Oct. 1981.

[25] Hsia, Y. C., Krothapalli, A. and Baganoff, D., "Mixing of an Underexpanded Rectangular Jet Ejector," *Journal of Propulsion and Power*, Vol. 4, No. 3, June 1988, pp. 256-262.

[26] Krothapalli, A. and Hsia, Y. C., "Discrete Tones Generated by a Supersonic Jet Ejector," Journal of the Acoustical Society of America, Vol. 99, No. 2, Feb. 1996, pp. 777-784.

[27] Powell, A., "On the Noise Emanating from a Two-Dimensional Jet Above the Critical Pressure," The Aeronautical Quarterly, Vol. 4, Feb. 1953, pp. 103-122.

[28] "Digital Signal Processing VIs," LabVIEW Function and VI Reference Manual, National Instruments Corporation, Austin, TX, January 1998, pp. 39-1 to 39-20.

[29] Kreyszig, E., Advanced Engineering Mathematics, 7th ed., John Wiley & Sons, New York, 1993, p. 710.

[30] Kapur, A., Cummings, A. and Mungur, P., "Sound Propagation in a Combustion Can with Axial Temperature and Density Gradients," *Journal of Sound and Vibration*, Vol. 25, No. 1, pp. 129-138, 1972.

[31] Forsythe, G. E., Malcolm, M. A. and Moler, C. B., Computer Methods for Mathematical Computations, 1st ed., Prentice-Hall, Englewood Cliffs, NJ, 1977, pp. 129-147.

8. PUBLISHED PAPERS

[1] Cramer, J. M., Marshall, W. M., Pal, S. and Santoro, R. J., "Acoustic Coupling in a Rocket-Based Combined Cycle Duct," to be presented at the 12th AIAA Space Planes and Hypersonic Systems and Technologies Conference, Norfolk, VA, December 15-19, 2003.

9. MEETINGS

[1] Cramer, J. M., Pal, S., Marshall, W. M. and Santoro, R. J., "Recent Experimental Results Related to Ejector Mode Studies of Rocket-Based Combined Cycle (RBCC) Engines," NASA Spring Workshop on Fluids-2003, Birmingham, AL, April 22-24, 2003.

[2] Cramer, J. M., Marshall, W. M., Pal, S. and Santoro, R. J., "Sea-Level Static Testing of the Penn State Two-Dimensional Rocket-Based Combined Cycle (RBCC) Testbed," Propulsion Engineering Research Center, Penn State, Fourteenth Annual Symposium, The Pennsylvania State University, State College, PA, December 10-11, 2002.

[3] Cramer, J. M., Pal, S., Marshall, W. M. and Santoro, R. J., "Sea-Level Static Testing of the Penn State Two-Dimensional Rocket-Based Combined Cycle (RBCC) Testbed," MSFC Fall Fluids Workshop-2002, Huntsville, AL, November 19-21, 2002.

10. PERSONNEL

Robert J. Santoro, George L. Guillet Professor of Mechanical and Nuclear Engineering, co-Principal Investigator

Sibtosh Pal, Senior Research Associate, Department of Mechanical and Nuclear Engineering co-Principal Investigator

John Cramer, Ph.D Student, Department of Mechanical and Nuclear Engineering

Mayumi U. Greene, MS 2002, Department of Mechanical and Nuclear Engineering

Larry Schaaf, Senior Research Technician, Department of Mechanical and Nuclear Engineering